Fluorescent Analogues of Potential Cancer Theranostic Agents

Jayden Bradley Wells

A thesis submitted in fulfilment of the requirements
for the degree of Master of Philosophy

Faculty of Science,
The University of Sydney
2023

Statement of Contribution

I declare that this thesis, presented for the degree of Master of Philosophy, is solely my own work, except where otherwise stated. It has not been submitted, in whole or in part, for any other previous degree.

ICP-MS experiments were conducted by Dr. Nicholas Proschogo.

Jayden Wells
September, 2023

Table of Contents

Table of Figures

Acknowledgements

First off, to my supervisor, Prof. Louis Rendina. Your friendly guidance, expertise and reassurance has made this project an absolute pleasure from start to finish. I am extremely grateful for your endless support in managing the degree, and always look forward to our catch-ups and group meetings. Annon allen!

To my group, including Dr. Leila Hill, Dr. Anita Marfavi, Dr. Poya Kavianpour, Eliash Hemzal, Tom Carraro, Nick Smith, Alex Sadler, Xinyi (Sophia) Zhang and Nina Qiu, for your friendship and support. I'm so grateful to have met you all and for the experiences that we have shared – even if Wednesday afternoon HSPs have likely given me cardiovascular disease. Our chats around the office and lab have made my time spent in the group always fun, interesting and enjoyable.

Thank you Dr. Aviva Levina, for your patience and endless guidance with cell work, Dr. Nicholas Proschogo, for your friendly advice and support with mass spectrometry, Dr Pamela Young, for your help with fluorescence microscopy, Dr. Cody Szczepina, for sharing your expertise with HPLC and Dr. Ian Luck for your expertise with NMR.

Finally, to my family. Your never-ending love and support is my foundation.

Abstract

Lanthanoid-based metal complexes containing delocalised lipophilic cations (DLCs) hold significant clinical potential as theranostic agents against various types of cancer, including glioblastoma. These complexes, which contain a phosphonium targeting vector as the DLC, have been shown to selectively localise to the mitochondria of cancer cells and are promising candidates for neutron capture therapy (NCT), as well as photon activation therapy (PAT), thereby potentiating the selective destruction of cancerous tissue. While they hold significant potential, additional work is required to further characterise various properties of these complexes, such as their intracellular biodistribution.

In this project, a number of novel fluorescent lanthanoid complexes were synthesised and fully characterised. These complexes utilised both europium(III) and terbium(III) centres, coordinated by a DO3A-based ligand structure. A linker domain, typically consisting of a fluorescent sensitising antenna group (i.e. a xylyl, 2º-amide-xylyl, or naphthyl group), was used to connect the central ligand structure to a targeting moiety, which consisted of a DLC known as triphenylphosphonium (TPP).

Fluorescence excitation and emission spectroscopic properties as well *q* values were determined, which are relevant in maximising fluorescent yield. A selection of these metal complexes (i.e. **13**, **14**, **16**, **17**) were visualised inside intact human cancer and normal cells using fluorescent microscopy. Enhanced co-localisation was observed for both the metal complexes and the MitoTracker Deep Red (MTDR) probe within human cancer (glioblastoma T98G) cells relative to normal (foetal glial SVG-p12) cells. Such studies were complemented by ICP-MS cell uptake studies.

These fluorescent studies serve as a strong precedent for a relatively time-efficient, cheap and effective means of analysing cellular localisation of this class of metal complexes, which can hopefully be incorporated into future studies involving analogues of such complexes, and can potentially replace other more time-intensive and costly methods such as synchrotron XRF studies.

List of Abbreviations

4CCA	*Cyano-4-hydroxycinnamic acid*
ADP	*Adenosine diphosphate*
ATP	*Adenosine triphosphate*
BNCT	*Boron neutron capture therapy*
BPA	*Boronophenylalanine*
BSH	*Sodium borocaptate*
CNS	*Central Nervous System*
CoA	*Co-enzyme A*
DCM	*Dichloromethane*
DLC	*Delocalised Lipophilic Cation*
DMF	*Dimethylformamide*
DNA	*Deoxyribonucleic acid*
DO3A	*1,4,7,10-tetraazacyclododecane-1,3,7-triacetic acid*
DOTA	*1,4,7,10-tetraazacyclododecane-1,3,7,10-tetraacetic acid*
ESI	*Electrospray Ionisation*
FADH2	*Flavin adenine dinucleotide*
GBCA	*Gadolinium based contrast agent*
GBM	*Glioblastoma Multiforme*
HPLC	*High Performance Liquid Chromatography*
ICP	*Inductively coupled plasma*
LET	*Linear Energy Transfer*
LMCT	*Ligand to metal charge transfer*
Ln	*Lanthanoid*
MALDI	*Matrix assisted laser desorption ionisation*
MRI	*Magnetic Resonance Imaging*
MTDR	*MitoTracker Deep Red*
NADH	*Nicotinamide adenine dinucleotide*
NCT	*Neutron Capture Therapy*
NMR	*Nuclear Magnetic Resonance*
NOTA	*1,4,7-triazacyclononane-1,4,7-triacetic acid*
NSF	*Nephrogenic systemic fibrosis*

OBD	*Optimum bed density*
PAT	*Photon activation therapy*
PDA	*Photodiode array*
ROS	*Reactive Oxygen Species*
SPECT	*Single photon emission computed tomography*
SSR	*Synchrotron stereotactic radiotherapy*
SVG-p12	*Human foetal glial cell line*
T98G	*Glioblastoma cell line*
TA30	*30:70 MeCN:0.1% aqueous TFA*
TFA	*Trifluoroacetic acid*
TGA	*Therapeutic Goods Administration*
THF	*Tetrahydrofuran*
TPMP	*Triphenylmethylphosphonium*
TPP	*Triphenylphosphonium*
UCP	*Uncoupling protein*
WHO	*World Health Organisation*

Chapter 1:

Introduction

1.1 – An Overview of Cancer

As a disease, cancer is characterised by the uncontrolled division of cells possessing abnormal proliferative genetic mutations.[1] Affecting most multicellular organisms, cancer is often caused by exposure to carcinogens, such as asbestos or X-rays, however can also be caused by endogenous processes, such as aberrant autoimmune processes that lead to deoxyribonucleic acid (DNA) replication errors.[1] This uninhibited proliferation of abnormal cells can lead to tumour development and metastasis, ultimately resulting in organ dysfunction, organ failure and death.[1]

Even the earliest human records (e.g. those documented by ancient Egyptian civilisations) demonstrate an awareness of cancer, however being a disease that predominantly occurs later in life, it wasn't until the major increase in life-expectancy during the 20th century that cancer began to affect a large proportion of the human population.[1] Disease burden is a modern epidemiological measure of both lifestyle impact and premature death due to disease within a population. Defined as the number of years of healthy life lost due to death and illness, total disease burden is credited as the single best measure of a population's health.[2] Currently, cancer (all forms) accounts for 17% of the total disease burden in Australia, making it the largest contributor to total disease burden.[3] This is reflected in statistics from the Australian Institute of Health and Welfare, which in 2020 reported approximately 150 000 newly diagnosed cancer cases as well as 50 000 cancer related deaths. These numbers are expected to rise in the coming years due to Australia's aging population.[3] Cancer also impacts the Australian economy due to removal of workers from the labour force. In 2015, cancer related non-participation in the Australian labour force was estimated to have reduced Australia's GDP by $1.7 billion.[4] It is thus obvious that cancer takes a huge toll on the Australian society, in terms of both total wellbeing and economic impact.

1.1.1 – Glioblastoma

Glioblastoma (GBM) is a highly proliferative type of central nervous system neoplasm, consisting of a group of genetically and phenotypically heterogenous tumours.[5] Being of Grade IV histological malignancy (the highest malignancy grade

according to the World Health Organisation (WHO) classification scheme), GBM is both the most common and most lethal primary brain tumour that affects humans.[5] The vast majority (90%) of GBM cases develop from normal glial cells *via* multistep tumorigenesis over a period of approximately 3 months.[5] Currently, the most common forms of GBM treatment include a combination of chemotherapy and radiotherapy, as well as tumour resection.[6] However, even with aggressive treatment, the long-term prognosis is often poor, with the post-diagnosis survival time in young people being under 4 years.[7]

1.2 – Traditional Cancer Treatment

In many cancer types, local growth continues for an appreciable amount of time, prior to metastasis. This gives the opportunity for the complete local resection of a malignant tumour, which can often be curative. Indeed, resective surgery continues to result in the most cancer cures.[1] Surgical resection is frequently considered the most effective treatment option for GBM, as this approach has been associated with higher survival times.[5] Unfortunately, however, radical resection is rarely possible without further compromising patient health, as GBM tumours often exhibit extensive spreading patterns within the brain, as well as poorly defined margins.[8] As such, the anatomical location of a GBM tumour (including the spreading pattern and margin definition) is a key determinant in the success of resective surgery.

The radiotherapy landscape has seen some major advancements in recent decades, such that modern clinical oncologists able to use cross-sectional imaging to accurately target tumorous tissue, while protecting healthy tissue from the majority of the radiation exposure.[1] Nowadays, radiotherapy is used to treat approximately 50% of all cancer patients.[9] Radiotherapy involves the utilisation of ionising radiation (such as X-rays, gamma-rays, high-energy electron beams or protons) to trigger various intracellular apoptotic signalling pathways, which often involve reactive oxygen species (ROS) generation, DNA damage and subcellular organelle stress (particularly within the endoplasmic reticulum and mitochondria).[10] While radiotherapy can be targeted to a certain extent, collateral damage to healthy tissue is unavoidable, often causing tissue necrosis or mutations, which can result in the formation of secondary cancers.[11] The efficacy of radiotherapy is limited in GBM

tumours, both because of the considerable off target damage to healthy brain tissue, as well as the fact that GBM tumours are usually hypoxic, resulting in a lesser ROS generation.[12]

Chemotherapy is another popular form of cancer treatment, involving the utilisation of drugs that target (with varying selectivity) and initiate the destruction of cancer cells.[1] The earliest chemotherapy agents were based on nitrogen mustards – chemical warfare agents used in the First World War.[13] Nitrogen mustard based drugs function by cross-linking DNA (by either inter- or intra- strand linkages), thereby preventing processes fundamental to cell survival (such as transcription or DNA replication), which ultimately results in apoptosis.[13] While nitrogen mustards (and other DNA alkylating agents) also damage healthy cells, cancer cells, being generally more proliferative and metabolically active, are normally affected by these chemotherapeutic agents to a greater extent. Unfortunately, poorly selective chemotherapeutic agents usually damage rapidly dividing healthy cells, such as those composing hair follicles and bone marrow, resulting in side-effects such as hair loss and pancytopenia, respectively.[1] Owing to major developments in the understanding of cancer biochemistry and biology, medicinal chemists are now able to develop drugs that target cancer cells with much higher selectivity. Nevertheless, drug delivery and off target toxicity remain key challenges in modern chemotherapeutic drug discovery.[13] An added complication for central nervous system (CNS) based tumours, such as GBM, is that the blood-brain-barrier prevents the entry of many types of drugs, although in many GBM patients the BBB is somewhat compromised.[5]

It should be noted that cancer treatments are most often and effectively used in a complementary fashion. Chemotherapy and radiotherapy are frequently utilised as adjuvant treatment options following resective surgery, in order to eradicate any residual microscopic disease.[1] This is an attractive approach, as smaller quantities of micro-metastatic disease are often better able to be eradicated by drug and radiation therapy than larger established tumour masses, which are less penetrable.[1] Currently, the mainstay of GBM treatment involves surgical resection, followed by X-ray radiation therapy and chemotherapy with temozolomide.[14] As previously mentioned, this approach has been found to extend life expectancy significantly.[7]

More recently, immunotherapy directed treatments such as chimeric antigen receptor T-cell therapy and immune checkpoint inhibitors have been also found to hold considerable promise in GBM treatment.[15]

1.3 – Targeting Cancer Cells

Traditional cancer therapies usually rely on the premise that cytotoxic agents, such as alkylating agents, are more likely to affect rapidly dividing cancer cells than healthy cells. While this premise holds to a certain extent, traditional cancer therapies notoriously cause off-target damage to healthy cells, as a result of their limited selectivity.[1,16] This leads to systemic toxicity and often harsh side effects. A more rational approach to the design of therapeutic anti-cancer agents is to exploit biochemical differences between healthy cells and cancerous cells, in order to optimise cancer cell selectivity.[16] Modern drugs that are developed for the purpose of cancer treatment generally possess two critical components that are connected by a suitable linker. These are: (i) a targeting moiety that is able to selectively deliver the drug to cancer cells and (ii) a cytotoxic 'warhead' moiety, that is able to initiate the destruction of targeted cancer cells.[16]

1.3.1 – Mitochondria

Mitochondria are double-membrane enveloped organelles that are responsible for maintaining a range of cellular processes, including; cellular metabolism, redox signalling, calcium homeostasis and apoptosis signalling.[17] A hallmark of many types of cancer is abnormal mitochondrial function, whereby energy metabolism pathways primarily involve glycolysis instead of oxidative phosphorylation, even under normal conditions.[18] This is associated with an increase in ROS generation.[17]

Adenosine triphosphate (ATP) is the energy currency of the cell. The cleavage of its terminal phosphate group is a high-energy process that is utilised in almost all energy-demanding enzymatic reactions.[19] The principal function of the mitochondria is to generate ATP, which occurs in four major steps. The first step involves the formation of acetyl co-enzyme A (acetyl-CoA), most of which is generated by either the beta-oxidation of fatty acids or the glycolytic pathway, which uses D-glucose as a

substrate.[19] In the second step, within the mitochondrial matrix, acetyl-CoA is processed by the citric acid (TCA) cycle, which generates biological reducing agents nicotinamide adenine dinucleotide (NADH) and flavin adenine dinucleotide ($FADH_2$).[19] The third step involves the transfer of electrons from these biological reductants to a series of redox-capable protein complexes that are embedded within the inner mitochondrial membrane.[19] The exergonic transfer of electrons between these protein complexes (eventually terminating in the reduction of molecular oxygen to water) is coupled to the translocation of protons across the inner mitochondrial membrane, from the mitochondrial matrix to the intermembrane space, resulting in the generation of a proton gradient across the inner mitochondrial membrane.[19] In the fourth and final step of ATP synthesis, the protons in the intermembrane space are allowed to pass down their concentration and charge gradient, through ATP synthase (also embedded within the inner mitochondrial membrane), back into the mitochondrial matrix.[19] This process is coupled with the synthesis of ATP within the mitochondria, using adenosine diphosphate (ADP) as a substrate (Figure 1).[19] ATP is then pumped out of the matrix by adenine nucleotide translocase, a transmembrane carrier protein within the inner mitochondrial membrane that exchanges ATP for free ADP and a phosphate ion.[19]

Given the vital role that the mitochondria play in cellular energy metabolism, they provide an excellent target for therapeutic drugs.

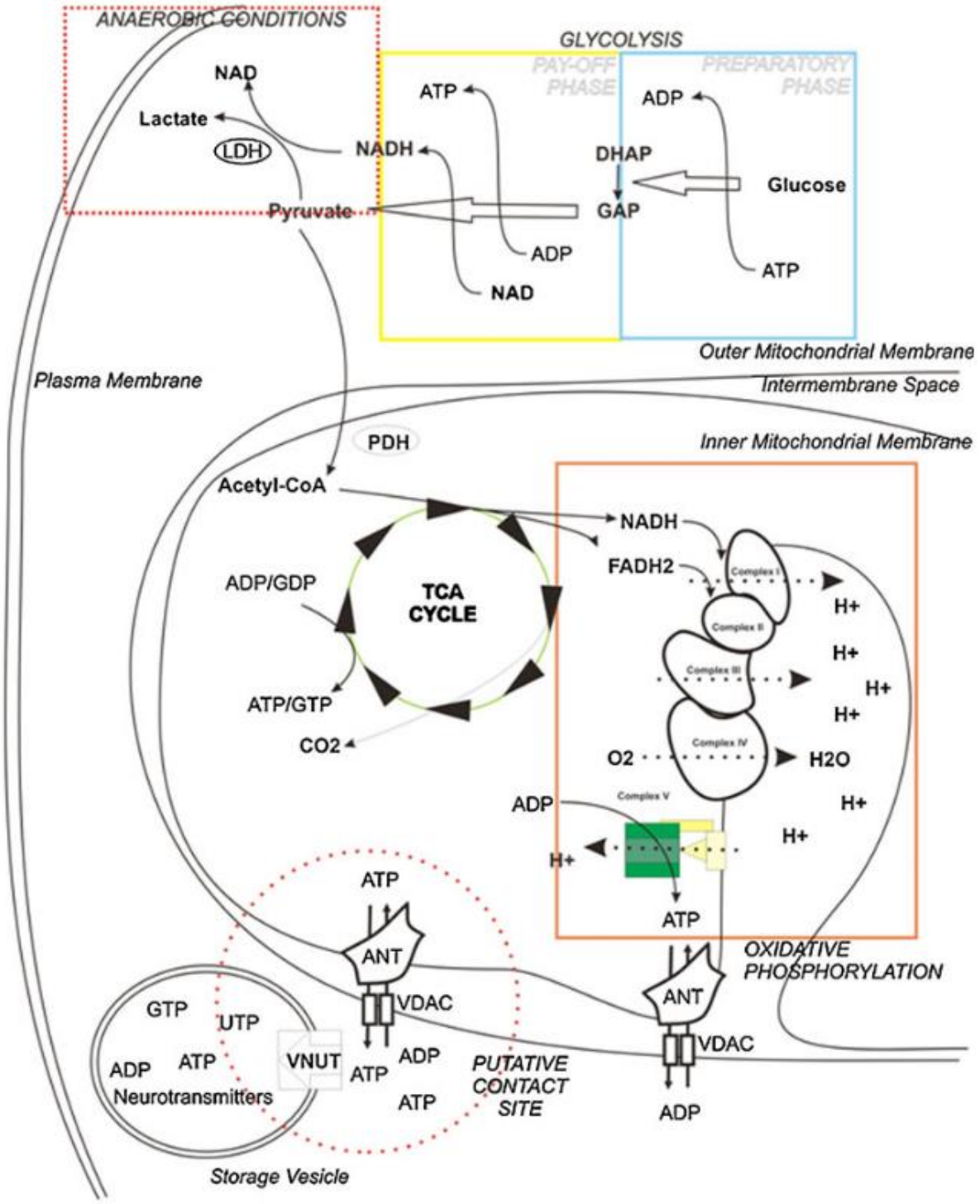

Figure 1: The mitochondrial ATP production process, depicting the citric acid cycle, electron transport chain, proton gradient generation and finally, ATP synthesis, by ATP synthase. Image taken from Bonora, *et al.*[19]

1.3.1.1 – The Warburg Principle

In most differentiated, non-proliferative cells, D-glucose is metabolised to pyruvate (*via* glycolysis), which pyruvate dehydrogenase converts to acetyl-CoA – the precursor for the citric acid cycle. Whilst glycolysis does generate some ATP itself, most differentiated cells produce 95% of their total ATP by mitochondrial oxidative phosphorylation.[20] This is generally thought of as favourable, as oxidative phosphorylation is much more efficient in terms of ATP production than glycolysis. Indeed, 1 mole of glucose generates approximately 36 moles of ATP through the oxidative phosphorylation pathway, but it only generates 2 moles of ATP *via* glycolysis.[21]

In cancer cells, it is estimated that aerobic glycolysis is responsible for 50-70% of the total ATP production.[22,23] This key metabolic difference between cancer cells and their healthy counterparts is termed the 'Warburg effect'.[18] In order to sustain such high levels of glycolysis, it is necessary for cancer cells to up-regulate the production of glycolytic proteins. These include the plasmalemmal glucose transporters, hexokinase-II, pyruvate kinase M2, and lactate dehydrogenase.[24–27]

Cell proliferation involves the mass biosynthesis of proteins, nucleic acids and membranes. As such, there is a high demand for amino acids, nucleotides and lipids in proliferating cells.[20] One possible explanation for the Warburg effect is that various glycolytic intermediates are able to be converted to substrates used by the pentose phosphate pathway, which generates ribulose-5-phosphate and NADPH – two key metabolites for cell proliferation.[28] It has also been suggested that mutations within mitochondrial DNA genes that encode key citric acid cycle enzymes is a contributor to the Warburg effect.[29]

1.3.1.2 – Mitochondrial Membrane Potential

The proton gradient generated across the inner mitochondrial membrane has both a chemical component (i.e. ΔpH), as well as an electrical component, termed the mitochondrial membrane potential ($\Delta\Psi_M$). It has been found that in many cancerous

cell lines, $\Delta\Psi_M$ is approximately 60 mV higher than that found in healthy cells, within which $\Delta\Psi_M$ tends to range between 108-159 mV, with a mean value of 139 mV.[30–34]

One possible explanation for the higher $\Delta\Psi_M$ observed in cancer cells is the relative activity of mitochondrial uncoupling proteins (UCPs), compared to healthy cells. It has been observed that $UCP2^{-/-}$ mice develop more colon tumours than $UCP2^{+/+}$ litter-mates.[35] Furthermore, $UCP2^{-/-}$ cells have been found to exhibit more cancer-like characteristics, including enhanced colony formation, hypoxia, increased oxygen consumption, and a low ATP content.[36] As such, diminished UPC2 expression in cancer cells is one candidate explanation for the hyperpolarised $\Delta\Psi_M$ observed in cancer cells.

1.3.2 – Delocalised Lipophilic Cations

In the early 1980s, it was observed that the lipophilic cation, Rh123 (Figure 2), could serve as a highly-specific mitochondrial fluorescent stain.[33,37] Furthermore, it was realised that relative to healthy epithelial cells, the mitochondria of carcinoma cells exhibited much higher uptake and prolonged retention times of Rh123.[38–40] Interestingly, increased mitochondrial Rh123 uptake was correlated with increased Rh123 cytotoxicity.[38–40] For instance, Rh123 was shown to markedly inhibit the proliferation of carcinoma cell lines that displayed high uptake, however it had minimal effect on the clonal growth of cell types that exhibited minimal uptake and shorter retention times.[41] The anti-cancer potential of Rh123 was also demonstrated *in vivo*, where it was found that following Rh123 treatment, the survival times of mice implanted with cancerous cells (either Ehrlich ascites tumour or MB49 mouse bladder carcinoma cells) were prolonged by up to 260%. As expected, Rh123 failed to prolong the survival times of mice that had been implanted with tumours that displayed minimal Rh123 uptake and retention.[41]

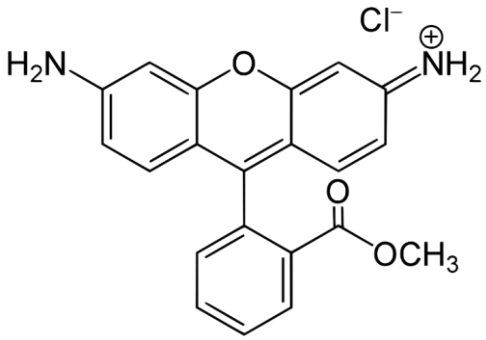

Figure 2: Molecular structure of Rh123, a delocalised lipophilic cation.

Subsequent studies elucidated two key properties of Rh123 that enable it to function as an effective mitochondrial stain. One of these key properties is hydrophobicity, which is necessary in order for Rh123 to bypass the relatively hydrophobic phospholipid bilayers of both the outer cell and mitochondrial membranes.[41] The second key property is a delocalised positive charge, which promotes the accumulation of Rh123 within the relatively negative mitochondrial matrix.[41] It has been demonstrated that the extent to which Rh123 accumulates in mitochondria is dependent on their $\Delta\Psi_M$.[34] Furthermore, uncharged Rh123 derivatives fail to exhibit any mitochondrial accumulation.[34] The mitochondrial uptake dependent cytotoxic effect of Rh123 is a result of the ability of Rh123 to act as an ATP synthase inhibitor.[42,43] This explains why increased Rh123 uptake (as a result of a higher $\Delta\Psi_M$) results in increased cytotoxicity.

Rh123 provided a working prototype for a novel class of mitochondrial targeted anti-cancer compounds, collectively known as delocalised lipophilic cations (DLCs). In recent years, this field has expanded dramatically to include a range of DLCs of varying structure, cytotoxicity and cancer cell specificity.[44–49] While passive diffusion is the primary mitochondrial uptake mechanism for most DLCs, it should be noted that the mechanisms by which these compounds exhibit cytotoxicity are quite varied.[41] For example, while Rh123 is an ATP synthase inhibitor, dequalinium chloride (DECA) interferes with the activity of NADH-ubiquinone reductase, a key protein in the mitochondrial electron transport chain.[41]

1.3.2.1 – DLC Mitochondria Targeting

The relationship between $\Delta\Psi_M$ and mitochondrial affinity for a particular DLC is given by the Nernst equation:[50]

$$\Delta\Psi_M = \frac{RT}{zF}\ln\left(\frac{[DLC]_{in}}{[DLC]_{out}}\right)$$

where $\Delta\Psi_M$ = mitochondrial membrane potential (V); R = gas constant (8.314 J K^{-1} mol^{-1}); T = temperature (K); *z* = ion valency; *F* = Faraday constant (96 500 C mol^{-1}); $[DLC]_{in}$ = concentration of DLC inside mitochondria (mM); $[DLC]_{out}$ = concentration of DLC outside of mitochondria (mM).[50]

As dictated by the Nernst equation, the ~60 mV difference in $\Delta\Psi_M$ between cancer and healthy cells (at physiological temperatures) results in an approximately 10-fold higher DLC uptake by cancer cell mitochondria, relative to the mitochondria of healthy cells.[51] In some cancer cell lines, the plasma membrane potential is also sufficiently polarised (between -30 and -60 mV), such that DLCs are 'pre-concentrated' in the cytosol. This effectively results in a greater amount of DLC available for mitochondrial uptake, thereby increasing mitochondrial DLC content by tremendous amounts.[52]

It is important to note that an increased mitochondrial membrane potential is not the only necessary requirement for the selective uptake and cytotoxicity of DLCs. While cardiac muscle cells have been found to exhibit hyperpolarised mitochondrial membrane potentials (similar to carcinoma cells),[53] *in vivo* studies involving the intravenous administration of DLCs such as MKR-077 or DECA have indicated that these DLCs do not cause significant cardiac toxicity.[41] This is possibly due to differences in cellular DLC uptake and retention characteristics, or differences in the sensitivity of specific target biomolecules to the cytotoxic effects of the DLC.

As briefly mentioned above, as in the case of Rh123, DLCs must be sufficiently hydrophobic in order to cross both the plasma and mitochondrial membranes. The activation energy barrier associated the passive diffusion of an ion across a lipid membrane is due to the ion's passage from the aqueous extracellular environment into the hydrophobic lipid bilayer interior. This activation energy has contributions

from both electrostatic and hydrophobic forces.[54,55] By far, the main component of the electrostatic contribution is the Born energy (W_B), which is due to the enthalpically unfavourable removal of the water molecules solvating the ion.[51,56] The Born energy is given by the following equation:[51]

$$W_B = \frac{q^2}{8\pi\varepsilon_0 r}\left(\frac{1}{\varepsilon_1} - \frac{1}{\varepsilon_2}\right)$$

where W_B = Born energy (V); q = the electric charge per mole of the cation (C mol^{-1}); ε_0 = the vacuum permittivity (F m^{-1}); r = the ionic radius (m); ε_1 = the dielectric constant within the membrane core (~2 F m^{-1}) and ε_2 = the dielectric constant of water (~80 F m^{-1}).[51]

It follows that the enthalpy required to move a ion into a lipid membrane is inversely proportional to radius of the ion. Put simply, this is because a more diffuse distribution of charge density gives rise to a smaller surface electric field magnitude, resulting in a diminished ability to polarise surrounding water molecules and weaker intermolecular bonding.[51] As such, DLCs partially owe their increased membrane permeability to their large area of positive charge delocalisation.

There are two other electrostatic components that contribute to ionic passive diffusion, however both are significantly weaker than the Born energy component.[57] One is the image energy, which is due to electrostatic interaction at the membrane interface.[55,57] The other is the intramembrane dipole potential, which exists predominantly because of the orientation of the polar carbonyl groups of the phospholipids that comprise the membrane.[55,57] Interestingly, the contribution of the intramembrane dipole potential lowers the activation energy of membrane permeability for anions, while elevating the activation energy for cations.[57]

In addition to the electrostatic contributions to the activation energy of DLC passive diffusion, there also exists the hydrophobic interaction contribution. This component is due to the intermolecular attraction between lipids and the hydrophobic cations, as well as the increase in systemic entropy associated with the movement of a largely lipophilic entity from a hydrophilic medium, into the lipophilic core of the plasma membrane.[51] It should be noted that the overall gain in systemic enthalpy is due to

both the release of the kinetically-restricted water molecules solvating the DLC, as well as the dissolution of the DLC within the membrane core.[51]

1.3.2.2 – Phosphonium Containing DLCs

Alkylphenylphosphonium DLCs have shown great promise as mitochondrial targeting agents, exhibiting higher mitochondrial accumulation than other common mitochondria targeting DLCs.[51] Furthermore, the synthetic chemistry associated with alkylphenylphosphonium DLC synthesis is generally straightforward, primarily involving reliable organic reactions, which enables the synthesis of a variety of derivatives.[58,59]

To this end, research involving the use of phosphonium containing DLCs for mitochondrial targeting has boomed over recent years, witnessing the development of a number of promising phosphonium-based anti-cancer drugs.[41,48,52,60,61] Triphenylmethylphosphonium (TPMP, Figure 3) is one agent that has demonstrated remarkable cancer cell selectivity in both canine and mouse *in vivo* models, with uptake into mouse Lewis lung carcinoma nodules being 549% greater than in control healthy lung tissue.[62] Additionally, TPMP exhibits many pharmacologically desirable features, including rapid clearance from the blood, relatively fast tumour uptake kinetics, and prolonged tumour retention (over a 20-95 minute interval).[62]

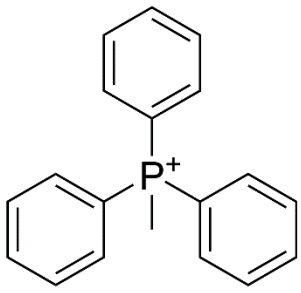

Figure 3: Molecular structure of triphenylmethylphosphonium.

Over the past decade, there has been considerable interest in the development of cancer drugs and imaging probes that utilise phosphonium containing DLC moieties as mitochondrial targeting vectors. Cationic cancer radiotracers, such as ^{99m}Tc-Tetrofosmin and ^{99m}Tc-Sestamibi (Figure 4) have traditionally been used in the clinic

for cancer diagnosis by single photon emission computed tomography (SPECT).[63] Unfortunately, however, the diagnostic ability of these imaging agents is severely limited by insufficient tumour uptake and poor tumour selectivity.[63]

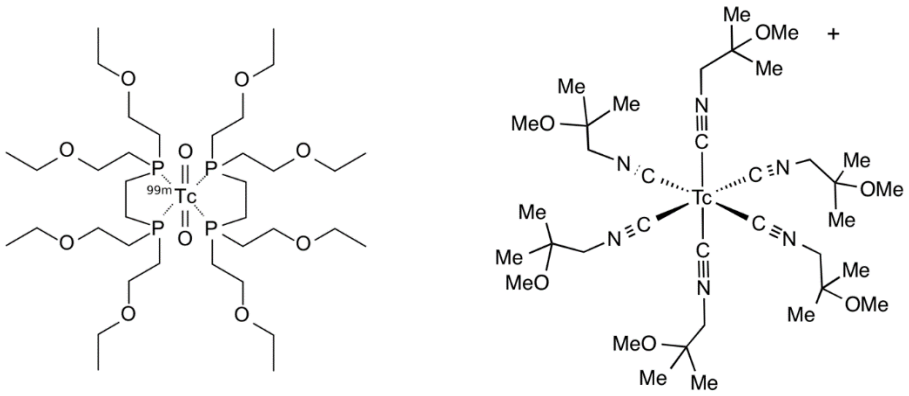

Figure 4: Molecular structures of ^{99m}Tc-Tetrofosmin (left) and ^{99m}Tc-Sestamibi (right).

Promising alternatives to these traditional radiotracers are ^{64}Cu-labeled phosphonium cations (Figure 5), which have demonstrated high tumour uptake and selectivity *in vivo*.[64] These new-generation radiotracers are composed of a phosphonium cation that is joined by a 'linker', to a ^{64}Cu chelating moiety, such as 1,4,7,10-tetraazacyclododecane-1,3,7,10-tetraacetic acid (DOTA), 1,4,7,10-tetraazacyclododecane-1,3,7-triacetic acid (DO3A) or 1,4,7-triazacyclononane-1,4,7-triacetic acid (NOTA).[63]

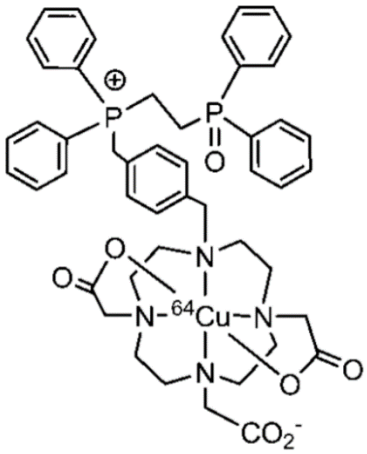

Figure 5: Molecular structure of ^{64}Cu-DO3A-xy-TPEP, a prototype radiotracer that features a phosphonium DLC.[64]

Phosphonium DLC moieties have also found use in targeting a range of other mitochondrial payloads, including mitochondrial dyes,[65] antioxidants,[66] anti-cancer drugs,[67] and small peptides.[68] Evidently, phosphonium containing DLCs hold much promise as tumour mitochondria targeting vectors.

1.4 – Binary Therapies

A binary therapy involves the utilisation of two components that are individually non-therapeutic, however upon combination, are able to deliver a therapeutic effect. This requires that the two singularly innocuous components have a high propensity for an interaction that results in the localised production of cytotoxin.[69] Such an approach to cancer therapy affords greater efficacy, selectivity and safety than traditional drug or radiation based therapies, especially in the treatment of intractable tumours.[70] Two common modes of binary therapy include neutron capture therapy and photon activation therapy.[69]

1.4.1 – Neutron Capture Therapy

Neutron capture therapy (NCT) employs nuclides of high neutron capture propensity to capture thermal neutrons, resulting in a prompt nuclear reaction, whereby cytotoxic radiation is released. An essential requirement for a suitable NCT nuclide is a high neutron-capture cross section (σ_{th}), which is measured in barns (Table 1).[71] Currently, boron neutron capture therapy (BNCT) is the best recognised and most investigated means of NCT.[72]

Table 1: Potential NCT candidate nuclides, with neutron capture cross section, σ_{th}, (b).[71]

Nuclide	Nuclear Reaction Type	Neutron Capture Cross Section σ_{th} (b)
^{3}He	(n, p)	5 333
^{10}B	(n, α)	3 835
^{113}Cd	(n, γ)	20 600
^{149}Sm	(n, γ)	42 080
^{151}Eu	(n, γ)	9 200
^{155}Gd	(n, γ)	61 100
^{157}Gd	(n, γ)	259 000

BNCT makes use of the naturally occurring (19.8% natural abundance) boron-10, which undergoes the nuclear fission reaction $^{10}B(n,\alpha)^{7}Li$. The products of this reaction possess high linear energy transfer (LET) properties, of approximately 150 keVμm^{-1} for the *α*-particle and 175 keVμm^{-1} for the lithium-7 nucleus.[71] As such, the radioactive decay products are highly cytotoxic, yet poorly penetrative, with path lengths in the range of 4.5-10 *μ*m, meaning that the energy deposition is generally limited to a single cell (typical cell diameter = 10 *μ*m). Accordingly, BNCT in principle presents the opportunity to selectively destroy boron-10 containing tumour cells, whilst sparing nearby healthy cells.[71]

Clinical BNCT research has focussed mainly on the treatment of high grade, intractable gliomas.[72] Currently, only two boron delivery agents, namely sodium borocaptate (BSH, Figure 6 - left) and *L*-boronophenylalanine (BPA, Figure 6 - right), have been explored in clinical trials to date, however many candidate third generation BNCT delivery agents are currently under development.[72,73] Both BSH and BPA have shown promising clinical results to date.

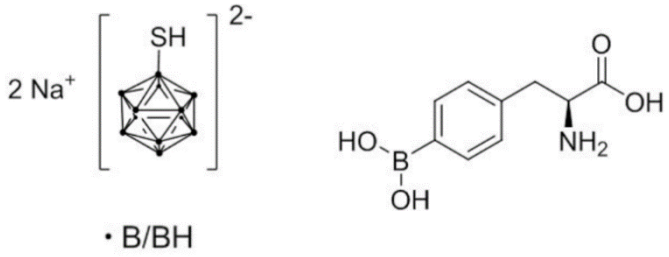

Figure 6: Molecular structures of BSH (left) and BPA (right).

The ^{157}Gd nuclide is another attractive candidate for use in NCT, as it possesses the largest neutron capture cross section of all stable isotopes. Furthermore, owing to the highly paramagnetic nature of Gd(III), compounds containing this lanthanoid metal ion function as excellent contrast agents in magnetic resonance imaging (MRI), opening up potential theranostic applications with such complexes.[74] Indeed, there are a range of Therapeutic Goods Administration (TGA) approved contrast agents, such as gadobutrol (Gadovist®), that utilise Gd(III) complexes. ^{157}Gd also exists in reasonable (15.7%) natural abundance, aiding in the sourcing of this isotope.[75]

In gadolinium neutron capture therapy (GdNCT), a thermal neutron capture event within a ^{157}Gd nucleus results in nuclear rearrangement to form an excited ^{158}Gd* nucleus, which relaxes through parallel internal transition and internal conversion processes, leading to the emission of a prompt *γ*-photon, internal-conversion electrons and an average of 5 high-energy Auger electrons per neutron capture event.[71,76] The Auger electrons produced possess high LET characteristics and are therefore able to exert a cytotoxic effect, either by generating free radicals or reacting directly with key biological molecules, such as DNA or mitochondrial respiratory proteins. It should be noted that Auger electrons deposit their energy over very short path lengths (approximately 12.5 nm), meaning that in order for ^{157}Gd-containing therapeutics to exert a tumoricidal effect, they should be targeted in very close proximity to their biological targets.[71,77]

1.4.2 – Photon Activation Therapy

Similar to NCT, photon activation therapy (PAT) involves the incorporation of an appropriate target nucleus into a critical site within tumour cells, which is followed by activation of the nucleus and the release of tumoricidal Auger electrons. This activation is not a nuclear process as it relies on the photoelectric effect, whereby photo-excitation of a high atomic-number element results in photoelectron emission, ultimately leading to an Auger electron cascade.[78–80]

Synchrotron stereotactic radiotherapy (SSR) is a type of PAT that utilises collimated monochromatic synchrotron X-rays, of an energy tuned to slightly above the *K*-edge of the photosensitive heavy element.[81] Interaction between these photons and *K*-shell electrons of the target atom results in *K*-shell electron ejection, leaving a *K*-shell vacancy, which is subsequently filled by an outer shell electron.[81] The energy lost by the outer shell electron in this process is released as a photon, which is of sufficient energy to, in turn, liberate an outer shell Auger electron.[82,83]

Gadolinium synchrotron stereotactic radiotherapy (GdSSR) is an extremely promising treatment option. While its full potential has not yet been realised, theoretical calculations predict that GdSSR would produce a greater Auger electron yield than gadolinium based NCT.[84] Additionally, it has been previously demonstrated that the Auger electrons released from DNA-bound Gd^{3+} are capable of inducing double-strand DNA cleavage.[75] Evidently, further research into GdSSR can be expected to yield interesting and potentially useful results in the future.

1.5– Gadolinium in Medicine

1.5.1 – MRI Contrast agents

Within the current Australian therapeutic landscape, gadolinium use is exclusively limited to gadolinium based contrast agents (GBCAs), which improve clarity and diagnostic capacity in magnetic resonance imaging (MRI). At the time of writing, the Australian Therapeutic Goods Administration (TGA) has approved eight distinct GBCAs, which differ in terms of their ligand structure.[85] Contrast enhanced MRI has

proved an invaluable technique for the imaging of soft tissue (such as the brain or abdomen) and is frequently used by physicians, to assess tumours, tissue vascularity and myocardial perfusion.[86] Unlike other common imaging modalities, MRI does not require patients to be exposed to ionising and potentially harmful radiation. GBCAs owe their ability to produce contrast enhanced MRI images to the highly paramagnetic nature of Gd^{3+}, which contains 7 unpaired, parallel spin *f*-electrons. This enables Gd^{3+} ions to shorten the T_1 and T_2 relaxation times of protons in adjacent water molecules, thereby improving tissue contrast enhancement, as a greater number of scans can be run over a given time period.[86,87]

1.5.2 – Gadolinium Toxicity and Chelators

While the use of gadolinium in medicine holds clear therapeutic value, over recent years, reports of gadolinium toxicity have been documented. The development of nephrogenic systemic fibrosis (NSF) has been linked with GBCA administration, in those patients exhibiting poor renal function.[88] NSF is a potentially fatal pathology, characterised by the fibrosis of various internal structures, including the skin, heart and lungs. Fortunately, the number of reported cases of NSF due to GBCA administration has virtually declined to zero as of mid-2009, due screening for renal deficiency prior to GBCA administration, as well as the use of safer (macrocyclic, higher stability) GBCAs and/or decreased doses.[89] Gadolinium deposition disease (GDD) is another disease associated with gadolinium based contrast agent treatment, that unlike NSF, has been observed in patients with normal renal function.[89] While extremely rare, GDD results in the deposition of gadolinium in vital organs such as the brain and kidneys, causing symptoms similar to those associated with NSF, with the addition of mental disorientation.[89]

A suggested mechanism for gadolinium toxicity is that Gd^{3+} ions are able to preferentially coordinate endogenous protein ion binding sites (for example, displacing calcium in calcium binding protein), leading to protein dysfunction and regional toxicity.[88,90] In addition to suboptimal ligand specificity, factors contributing to the release of Gd^{3+} from its ligand include the presence of competing cations (such as Zn^{2+}, Cu^{2+} and Fe^{3+}) that interact strongly with the ligand binding site, as well as the presence of high Gd^{3+} affinity biological ligands, which include phosphate

and carbonate groups.[88] Another factor that may be partially responsible for the release of Gd^{3+} from contrast agents that are taken up intracellularly, is lysosomal degradation, which can result in ligand breakdown.[88]

Given the apparent toxicity of free Gd^{3+} ions, it is vital that the gadolinium ion is coordinated with high affinity. It has been found that macrocyclic polydentate ligand systems such as 1,4,7,10-tetraazacyclododecane-1,4,7-triacetic acid (DO3A, Figure 7, left) and 1,4,7,10-tetraazacyclododecane-1,4,7,10-tetraacetic acid (DOTA, Figure 7, right) are able to coordinate Gd^{3+} ions to form kinetically inert, non-toxic, water soluble, thermodynamically stable and rapidly excretable complexes.[91]

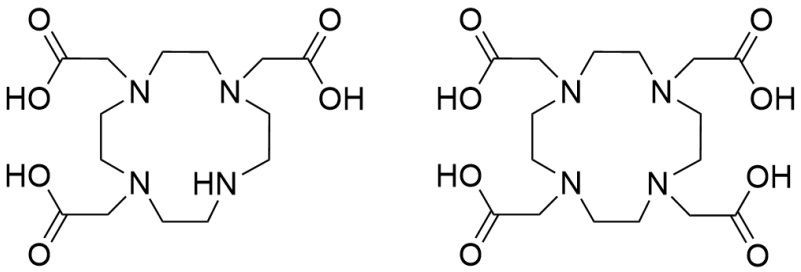

Figure 7: Molecular structures of DO3A (left) and DOTA (right).

These complexes owe their relative chemical inertness both to the chelate effect (DO3A and DOTA contain 7 and 8 coordinating atoms, respectively), as well as the macrocyclic effect, which results from the preorganisation of the macrocyclic ring.[89,91,92] Indeed, the three TGA approved macrocyclic GBCAs, Dotarem®, Prohance®, and Gadovist® (Figure 8) are based on derivatives of these ligand systems.[91] Studies have demonstrated that these contrast agents exhibit higher kinetic stability and less toxicity than the acyclic TGA approved GBCAs.[91] An additional benefit of DOTA and DO3A based GBCAs is that chemical modification of the ligand system, in order to introduce new functionalities, is relatively straightforward.[81]

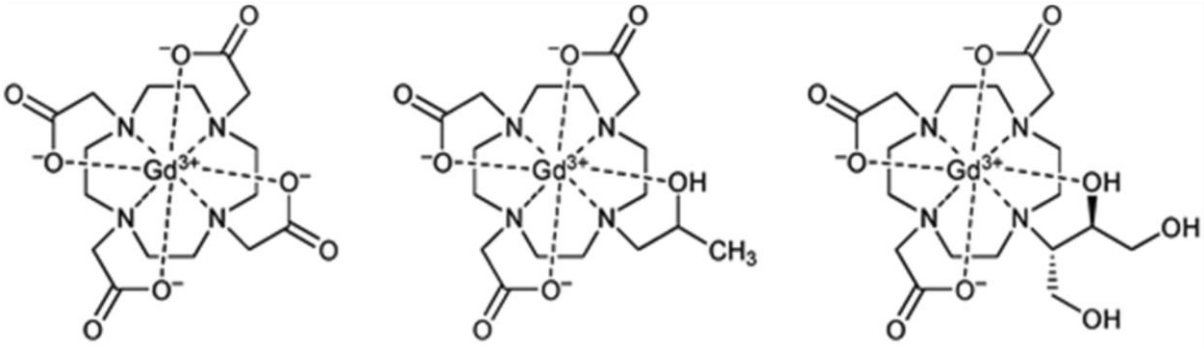

Figure 8: Molecular structures of Dotarem®, Prohance®, and Gadovist®.

1.6 – Additional Medically Relevant Isotopes

The ground electron configuration of Ln(III) ions is [Xe]4f^n, where *n* ranges between 0-14. The valence 4*f* electrons exist in inner orbitals and are often described as 'embedded', due to being shielded by the 54 electron Xenon core (particularly by the relatively radially diffuse 5$s^2$5p^6 subshells).[93] As a result, lanthanoids tend to exhibit fairly similar and predictable chemical reactivity. In the case of ligand binding, lanthanoids act as hard Lewis acids, meaning that they interact preferentially with hard Lewis base donors, such as high charge density oxygen or nitrogen. Given the high degree of chemical similarity between lanthanoids, it follows that high Gd^{3+} affinity ligands (such as DOTA and DO3A) have been found to coordinate other Ln(III) ions with similarly high affinity.[94]

The ability of the DOTA and DO3A ligand systems to form kinetically-inert complexes with a range of lanthanoids (as well as other metal isotopes) is of therapeutic and diagnostic interest, due to the varying emergent properties of such complexes. The medical applications of a selection of metal isotopes that are able to be coordinated by DOTA and DO3A ligand systems is summarised below (Table 2).[95–98]

Table 2: Medical applications of a range of metal isotopes that have demonstrated ability to be coordinated by DOTA and DO3A ligand systems.[95–98]

Metal Isotope	Medical Application
^{44}Sc	Long physical half-life ($t_{½}$ = 4.04 h) β^+ emitter for PET imaging.
^{47}Sc	Low energy β^- emitter for treatment of small tumours and cancer metastasis. Also emits low energy γ-radiation, which can be used for SPECT imaging.
^{64}Cu	β^+ emitter, useful for PET imaging, as well as a β^- emitter, which can be used for tumour treatment. Also emits γ-radiation, suitable for use in SPECT imaging.
^{66}Ga	Long physical half-life ($t_{½}$ = 9.49 h) β^+ emitter for PET imaging.
^{67}Ga	Low energy γ-radiation emitter that decays exclusively through electron capture and is suitable for SPECT imaging.
^{68}Ga	Leading β^+ emitter ($t_{½}$ = 1.13 h) for PET imaging, due to its high branching ratio and relative abundance.
^{86}Y	β^+ emitter ($t_{½}$ = 14.7 h) for PET imaging. Able to be coupled with yttrium-90 to form a chemically identical theranostic pair.
^{90}Y	Well established β^- emitter, exhibiting high-energy emission, yet relatively long soft-tissue range (11 mm). Suitable for treating tumours such as non-Hodgkin's lymphoma.
^{110m}In	β^+ emitter ($t_{½}$ = 1.15 h) for potential use in PET imaging.
^{111}In	Widespread γ-radiation emitter, used routinely in SPECT imaging. Decays by electron capture, releasing two γ-rays in the process.
^{114m}In	Medium energy γ-radiation emitter, potentially useful for SPECT imaging. Also an Auger electron emitter with potential to treat small tumours. The decay product, ^{114g}In contributes to the therapeutic effect as a high energy β^- emitter.

^{153}Sm	β^- emitter that has potential for tumour treatment. Also emits low energy γ-radiation, which can be used for SPECT imaging.
^{157}Gd	Highly paramagnetic species, suitable for use as an MRI contrast agent. Also holds potential therapeutic value in NCT and PAT.
^{177}Lu	Decays exclusively through low energy β^- emission, which is useful for tumour treatment. Low energy γ-radiation is produced in the process, which is useful for SPECT imaging and dose determination.
^{212}Bi	High energy β^- emitter as well as an α-emitter. Useful for targeted alpha therapy, however the high energy γ-radiation produced by the immediate daughter isotope (208-thallium) is viewed as a major drawback to clinical applicability.
^{213}Bi	Medium energy β^- emitter as well as an α-emitter, useful for targeted alpha therapy. Also a medium energy γ-radiation emitter, which is useful for SPECT imaging and dose determination.
^{225}Ac	Promising high LET α-emitter, which limits soft-tissue penetration to ~85 μm, meaning that the cytotoxic effect can be confined to a single cell. Decay products release medium to high energy γ-radiation, which is useful for SPECT imaging and dose determination.

Evidently, the development of cancer cell targeted DOTA and DO3A ligand systems could potentially serve a range of therapeutic and diagnostic purposes, depending on the metal isotope that is chelated.

Europium(III) and terbium(III) are able to be chelated by DOTA and DO3A ligands with a high degree of kinetic inertness.[94] Both of these Ln(III) ions possess well established fluorescence properties and are ideal candidates for tracking the cellular distribution of a particular ligand complex by means of fluorescence microscopy.[99,100] Due to the high degree of chemical similarity between the lanthanoid ions, it is reasonable to assume that a given ligand system will exhibit comparable cellular

distribution patterns, regardless of the nature of the lanthanoid metal centre.[94] Fluorescence microscopy using europium(III) and terbium(III) complexes is therefore a powerful experimental method for determining the intracellular localisation of DOTA and DO3A derivative complexes, as has previously been demonstrated (Figure 9).[101]

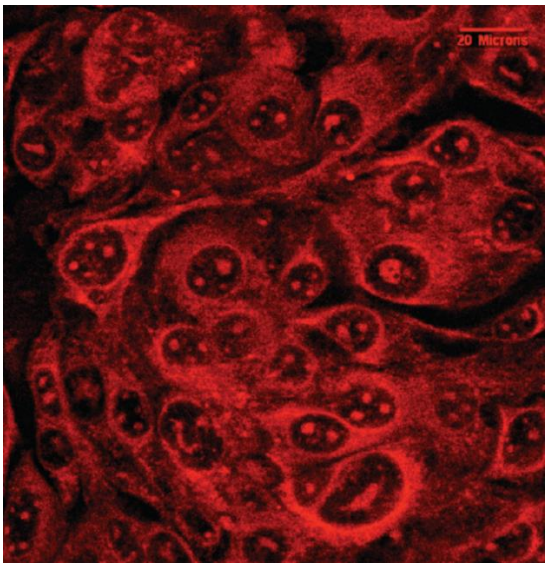

Figure 9: Confocal fluorescence microscopy image (λ_{exc} 405 nm) showing the intracellular ribosomal localisation profile of a typical europium-azathiaxanthone complex. Image taken from Montgomery, *et al.*[101]

1.7 – Lanthanoid Luminescence

1.7.1 – Physical Chemistry of Lanthanoids

The lanthanoids have a principal quantum number, n, of 4, and an angular momentum quantum number, ℓ, of 3. This corresponds to the 4*f* sub-shell, which comprises part of the *f*-block of the periodic table. The distinct electron wavefunctions of the 4*f* sub-shell are further defined by the magnetic quantum number (angular momentum projection), m_ℓ, such that m_ℓ is an integer between -3 and +3, meaning that there are $(2\ell + 1) = 7$ possible m_ℓ values that may be associated with a particular electron wavefunction in the 4f sub-shell. The m_ℓ value of each electron wavefunction is linked to orbital spatial orientation (Figure 10). The spin projection quantum number, m_s, of an electron wavefunction can take on the

values +½ or -½. In accordance with the Pauli exclusion principle, no two electron wavefunctions may possess the same four (n, ℓ, m_ℓ, and m_s) quantum numbers, meaning that the number of electron wavefunctions, n, regrouped by the 4*f* sub-shell is $(4\ell + 2) = 14$. As such, the ground electron configuration of all Ln(III) ions is $[Xe]4f^n$.[93]

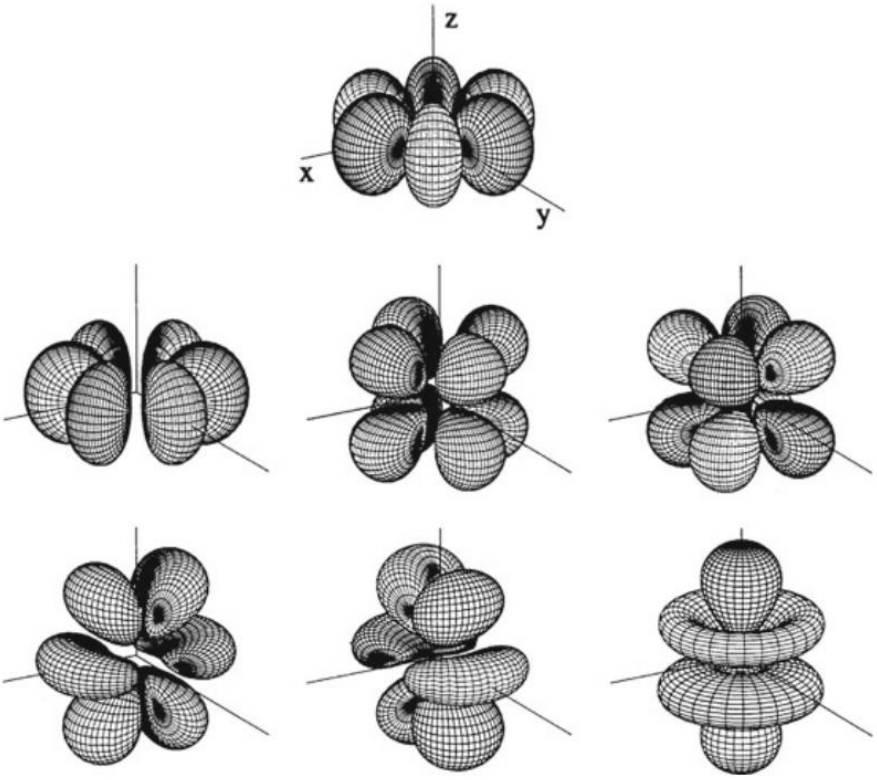

Figure 10: Shapes of 'hydrogenoid' 4*f* orbitals in Cartesian space. From top to bottom and left to right: $4f_{x(x^2 - 3y^2)}$, 4f $y_{(3y^2 - x^2)}$, $4f_{xyz}$, $4f_{z(x^2 - y^2)}$, $4f_{xz^2}$, $4f_{yz^2}$, and $4f_{z^2}$. Image adapted from *Lanthanide Luminescence.*[93]

Essential to an understanding of lanthanoid luminescence is the fact that n electrons can fill the 4*f* sub-shell in a number of configurations, or 'micro states', where differences between micro states correspond to variations in the allowed m_ℓ, and m_s quantum numbers of each electron. A particular micro state can be broadly characterised by two quantum numbers, M_L and M_S, where:

$$M_L = \sum_{\mathrm{i}=0}^{\mathrm{i}=n} (m_\ell)_\mathrm{i} \quad \text{and} \quad M_S = \sum_{\mathrm{i}=0}^{\mathrm{i}=n} (m_S)_\mathrm{i}$$

A group of microstates with the same M_L and M_S values (given by L and S, respectively, when in relation to a group of microstates), is called a spectroscopic

term, denoted by the term symbol, $^{(2S+1)}L$, where L is represented by a capital letter (S, P, D, F, G, etc for L values of 0, 1, 2, 3, 4, etc). The number of microstates that a particular spectroscopic term regroups is given by $(2S + 1)(2L + 1)$. It should be noted that for a lanthanoid with a particular number of electrons, n, there are several possible spectroscopic terms. The ground state spectroscopic term is given by the term that maximises both spin and orbital multiplicity (i.e. produces the highest possible values of L and S), in accordance with Hund's rules.[93]

Electron orbital angular momentum, ℓ, is intrinsically coupled to spin, s. The widely used Russell-Saunders coupling scheme considers this coupling at the level of the total angular momentum (i.e. using L and S values), as opposed to at the single electron level. The ability of this spin-orbital coupling to occur both constructively and destructively necessitates a new quantum number, J, which has values ranging between $(L + S)$ and $(L - S)$. As a result, the spectroscopic term is further energetically split into J levels (i.e. $^{(2S+1)}L_J$), each with $(2J + 1)$ degeneracy.[93] This $(2J + 1)$ degeneracy is partially lifted when a Ln(III) ion is inserted into an asymmetrical ligand field. Due to shielding, interaction between the 4*f* orbitals and the ligand field is weak, resulting in relatively minute energy level splitting that is referred to as Stark splitting.[93]

Three distinct types of electron transitions may occur in lanthanoids upon interaction with a photon, namely 4*f*-4*f* transitions, 4*f*-5*d* transitions, ligand to metal charge transfer (LMCT) and metal to ligand charge transfer (MLCT). This thesis will focus primarily on the 4*f*-4*f* transitions, as these are the most common and of particular relevance to the work at hand. 4*f*-4*f* transitions are formally forbidden by the Laporte parity selection rule, which states that electron transitions cannot occur between states of the same parity.[93] This selection rule is somewhat relaxed by the non-centrosymmetric ligand field, wherein opposite parity ligand field orbitals are mixed with the 4*f* orbitals, resulting in partially allowed (however weak) 4*f*-4*f* transitions.[93] The observed energy levels for a selection of Ln(III) ions is presented in Figure 11.

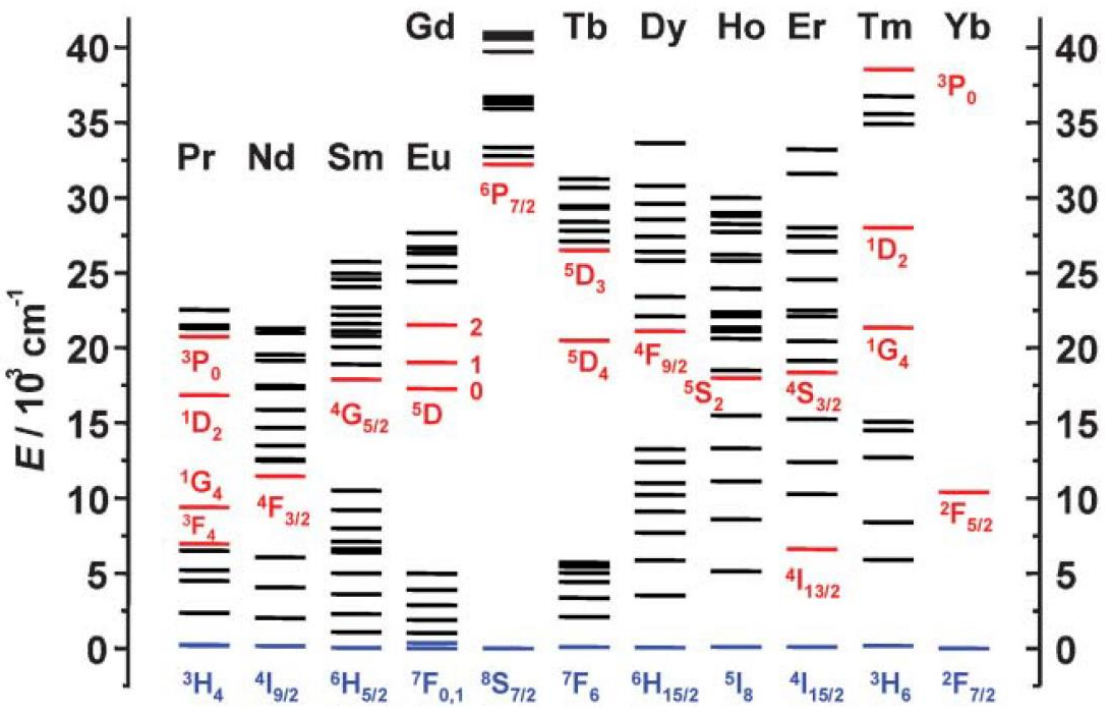

Figure 11: Energy level diagram with red levels representing the main emissive term and blue levels representing the ground electronic term of selected Ln(III) ions. Image taken from Bünzli, *et al.*[102]

Following light absorption, almost all Ln(III) ions exhibit luminescence, either by means of fluorescence, phosphorescence, or both. Due to the poor interaction between the 4*f* orbitals and the ligand field (the covalency of the Ln(III)-ligand bond is ~7% at most),[93] energetic promotion of a 4*f* electron does little to perturb the interatomic bonding within the complex, meaning that there is only minimal intramolecular bond distance lengthening upon excitation. This results in both sharp luminescence spectroscopic bands, as well as relatively small Stokes' shift values (Figure 12).[103]

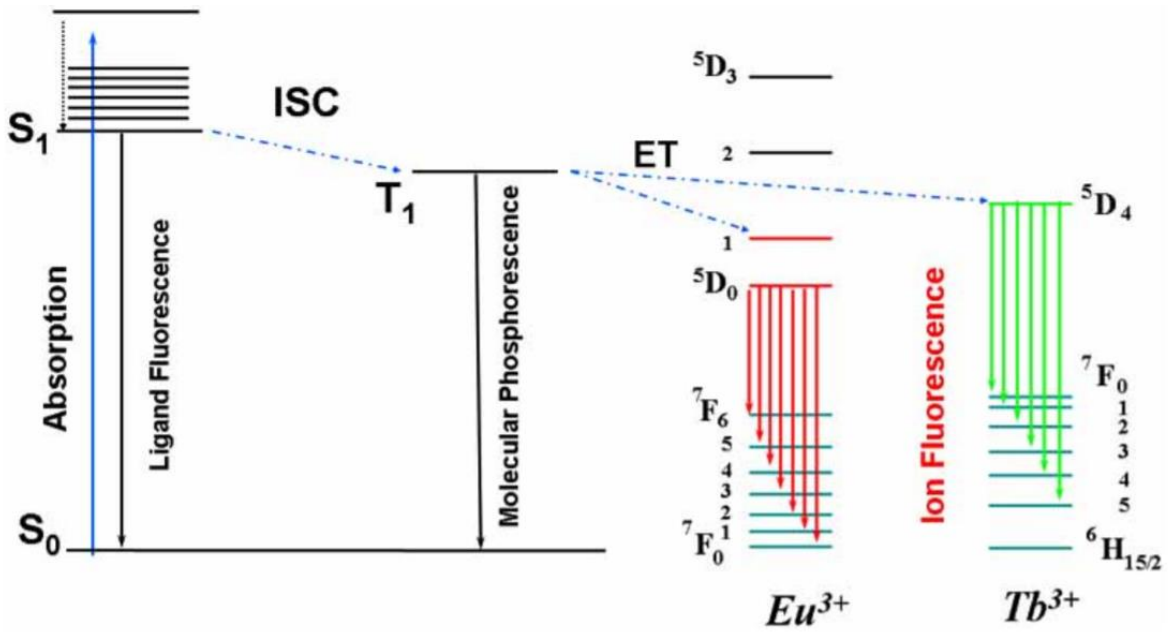

Figure 12: Jablonski diagram depicting the energy transfer to the Eu(III) and Tb(III) emissive levels. Image taken from Juanes, *et al.*[103]

1.7.2 – Lanthanoid Sensitisation

As *f-f* transitions are weak due to their Laporte-forbidden nature, unless considerable excitation power is used (i.e. laser excitation), lanthanoids often fail to exhibit appreciable light absorption and luminescence, which presents a problem if one desires to produce detectable lanthanoid luminescence at low levels. An experimentally proven and widely employed solution to this problem is to use sensitiser or 'antenna' organic molecules that are able to effectively absorb a given wavelength of light and transfer the associated excitation energy to a Ln(III) ion, which is then able to luminesce.[99] Such antenna systems commonly harvest light via aromatic $\pi \rightarrow \pi^*$ and/or $n \rightarrow \pi^*$ transitions.[104] Given the relatively weak covalency between the *f*-electrons and the ligand system in a Ln(III) complex, it is reasonable to consider antenna / ligand-centred excitation separately from Ln(III)-centred excitation. It has been hypothesised that there may be as many as 20-30 distinct rate constants, involving both singlet and triplet antenna excited states, that govern the sensitisation of lanthanoid complexes.[105] Nevertheless, the Dexter and Förster mechanisms (Figure 13) are thought to be two of the key means of energy transfer.[106,107] Briefly, both involve Laporte and spin allowed excitation of the

antenna, which is followed by intersystem crossing from the $^1S_1$* to the relatively long lived ^3T* state. In the Dexter 'double-electron exchange' mechanism, ^3T*→*4f** electron energy transfer is accompanied by *4f*→$^1S_0$ transfer, which is followed by light emission associated with the *4f**→*4f* relaxation.[93] In the Förster 'electrostatic multipolar' mechanism, antenna based ^3T*→$^1S_0$ intersystem crossing is accompanied by *4f*→*4f** promotion on the Ln(III) centre, which is again followed by light emission associated with the *4f**→*4f* relaxation.[93]

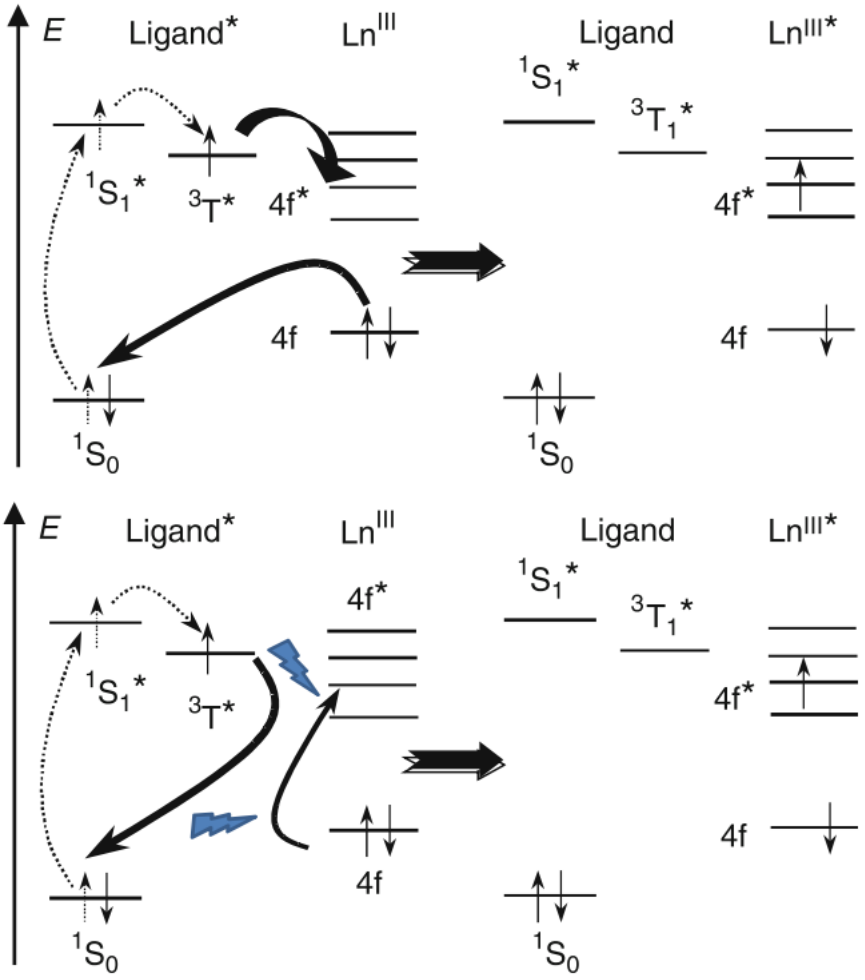

Figure 13: Dexter (top) and Förster (bottom) energy transfer mechanisms. Image adapted from *Lanthanide Luminescence*.[93]

Due to its dependence on orbital overlap (i.e. conjugation), the probability of the Dexter mechanism occurring is related to the distance, *d*, of the antenna to the Ln(III) centre by $e^{-\beta d}$, meaning that the Dexter mechanism is often only able to act over small distances (i.e. 30 – 50 pm).[93] On the other hand, the probability of Förster mechanism occurring is related to the distance of the antenna to the Ln(III) centre by

d^{-6}, meaning that this mechanism is able to act over longer distances (up to 1000 pm).[93]

For the sensitisation of Ln(III) ions, the antenna moiety is often conjugated to, or indeed a part of, the ligand system that coordinates the metal centre. There are several important considerations in the design of both the ligand and antenna systems that the chemist must be aware of. Luminescence quantum yield is usually maximised when the excited triplet state of the antenna is close in energy to one of the higher 4*f* excited states of the Ln(III) ion.[93] It is important, however, that the feeding triplet state of the antenna is sufficiently higher in energy than the emissive state of the Ln(III) ion, such that back-energy transfer is prevented.[93] As such, the antenna moiety should generally possess a triplet state energy of approximately 2500-3500 cm^{-1} above the emissive state of the Ln(III) metal centre.[93] Furthermore, it is thought that intersystem crossing between the excited singlet and triplet states of the antenna is more efficient when the energy gap between both states is approximately 5000 cm^{-1}.[93] These aspects form key considerations for the design of sensitised Ln(III) complexes.

1.7.3 – Quenching

While radiative relaxation of the excited Ln(III) complex has formed the majority of the discussion thus far, it is important to realise that non-radiative processes, such as vibrational quenching and photon-induced electron transfer, also contribute to depopulation of the excited state. Vibrational quenching, often seen as the most significant contributor to deactivation, is predominantly caused by O-H, N-H or C-H oscillators within close proximity of the excited Ln(III) centre.[108] This tends to be a competitive deactivation pathway when the energy gap between the excited and receiving states of the Ln(III) ion is less than 6 quanta of the quenching vibration.[93] A useful strategy to minimise vibrational quenching is to ensure that the ligand system employed coordinates the Ln(III) centre at as many sites as possible, in order to block the binding of potentially deactivating ligands (i.e. solvent water molecules). Care can also be taken to choose luminescent Ln(III) metal centres that possess a sufficient energy gap between the emissive and receiving state, such that vibrational quenching is minimised. It should also be noted that Ln(III)-antenna sensitisation

systems are susceptible to triplet state quenching (of the antenna) by molecular oxygen as well as back-energy transfer from the excited Ln(III) metal centre to the antenna.[93]

1.8 – The Current Study

The current project aimed to synthesise luminescent derivatives of phosphonium-based DLCs containing Ln(III), where Ln(III) = Eu^{3+} or Tb^{3+}. These particular Ln(III) ions were chosen based on their relatively strong and well established fluorescence properties. Candidate derivatives that displayed suitable fluorescence were then used to treat human glioblastoma (T98G) and human glial (SVG p12) cell lines. The treated cell lines were subsequently analysed using fluorescence microscopy, in order to compare the sub-cellular localisation of the Ln(III) complexes in both of these cell lines. Further characterisation revealed fluorescence excitation and emission spectral properties, as well *q* values.

The primary purpose of this study is to serve as a precedent for a relatively time-efficient, cheap and effective means of analysing cellular localisation of this new class of cancer theranostic agents.

Chapter 2:

Chemical Syntheses

2.1 – Overview and Design

The lanthanoid complexes generated within this project consisted of four principal components, namely; *(i)* the lanthanoid metal centre, *(ii)* the ligand surrounding the metal centre, *(iii)* the linker group between the ligand and the triphenylphosphonium moiety, and *(iv)* the triphenylphosphonium group.

An example of a typical lanthanoid complex generated in this research project, that contains each of these key components, is shown below (Figure 14).

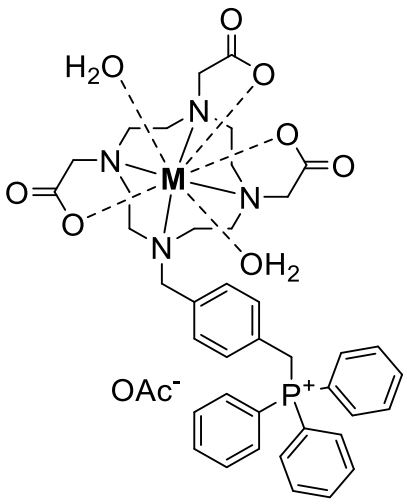

Figure 14: Example of a typical lanthanoid complex generated (**M** = Eu, Tb, Gd), containing the key groups common to all of the lanthanoid complexes generated.

A number of recent studies have demonstrated the theranostic potential of analogues of these complexes, as both anti-cancer therapy agents and as imaging probes.[12,74–76,81] Given the recent drive to utilise phosphonium containing DLC moieties as cancer mitochondrial targeting vectors,[52] these complexes utilise a TPP targeting group. As previous research has extensively characterised the biological consequences of variations in the nature of the aryl and/or alkyl groups attached to the phosphonium targeting group moiety,[77] the TPP targeting group was used consistently throughout this study as it typically shows the greatest cancer cell selectivity compared to derivatives containing a lesser number of aryl rings. Previous studies have also documented the ability of DO3A ligand systems to form highly thermodynamically stable complexes with lanthanoid(III) metal ions, and have

extensively explored the chemical and biological consequences of such ligand variations.[109] As such, a DO3A ligand system was employed exclusively throughout the course of this study.

Whereas previous studies have resulted in thorough chemical and biological profiles of properties such as tumour and normal cell uptake, cellular toxicity and stability of these compounds,[77,81] it has thus far proved difficult to observe directly and compare lanthanoid(III) complex localisation within different cell lines, with previous studies typically requiring the use of synchrotron X-ray beamlines for determining cellular uptake and biodistribution of very low levels of lanthanoid metal ions by means of X-ray fluorescence (XRF).[110] As one principal aims of this project was to mitigate this problem by directly visualising cellular biodistribution of these complexes using confocal fluorescence microscopy, the complexes synthesised here employed Eu and Tb centres. These two lanthanoid metal ions have firmly established and strong fluorescence emission profiles within detectable regions.[111,112] Given the Laporte forbidden nature of direct lanthanoid excitation, linkers containing an antenna sensitising moiety, such as a xylyl or naphthyl group were utilised in this work. Compounds **15**-**17** additionally contained a secondary amide group between the ligand and the xylyl group, so that the carbonyl oxygen of the amide group may provide another donor atom to the lanthanoid(III) centre. The intended effect here was to displace one of the water molecules from the first coordination sphere, in order to minimise vibrational quenching. For the purpose of clarity, herein, the complexes containing only a xylyl group within the linker moiety will be referred to as ‘first-generation’ complexes, whereas those containing both the xylyl group as well as the secondary amide within the linker moiety will be referred to as ‘second-generation’ complexes (Figure 15).

It should be noted that additional complexes were generated, which utilised both naphthyl and butyl linker groups. Aside from the different linker groups, these complexes were identical to the first-generation complexes, being synthesised in a similar fashion. This involved utilising dibromo species as starting compounds for the linker, which were subsequently joined to the ligand and phosphonium moieties utilising standard S_N2 reactions.

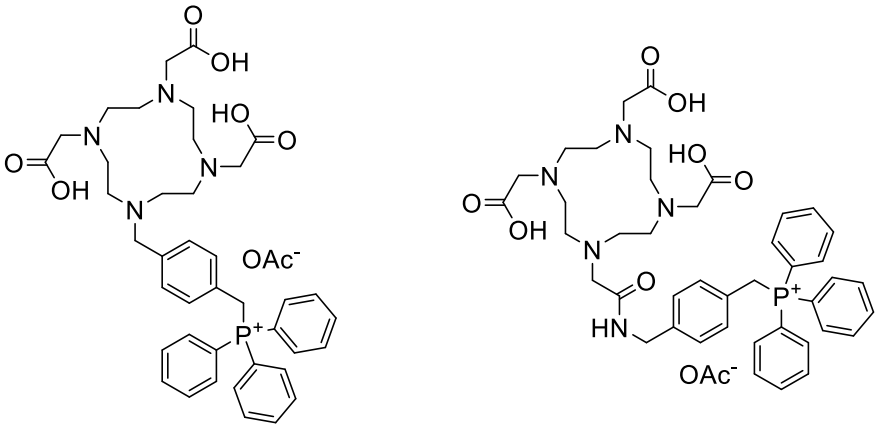

Figure 15: Molecular structure of the 'first-generation' (left) and 'second-generation' (right) ligand systems. Note that these structures differ by the presence of an amide bond between the xylyl group and the DO3A ligand system.

2.1.1 – Retrosynthetic Analyses

Retrosynthetic schemes of the general reaction pathways employed in the synthesis of both the first and second generation complexes are presented in Schemes 1 and 2, respectively. While these two syntheses share a number of common synthetic steps, the second-generation complexes required a more complex and laborious pathway, involving the formation of a phosphonium-amine intermediate as well as the stepwise addition of a carboxylic acid group to the protected triester. Many of the compounds generated have previously been routinely synthesised within the Rendina group.[77,81,113]

The method employed for the synthesis of the second-generation complexes was adopted after several failed attempts to synthesise these complexes using an alternative pathway that would have negated the use of coupling reagents, which pose various health risks. Unfortunately, this alternative method ultimately proved unsuccessful. Nevertheless, the attempt is documented and discussed below.

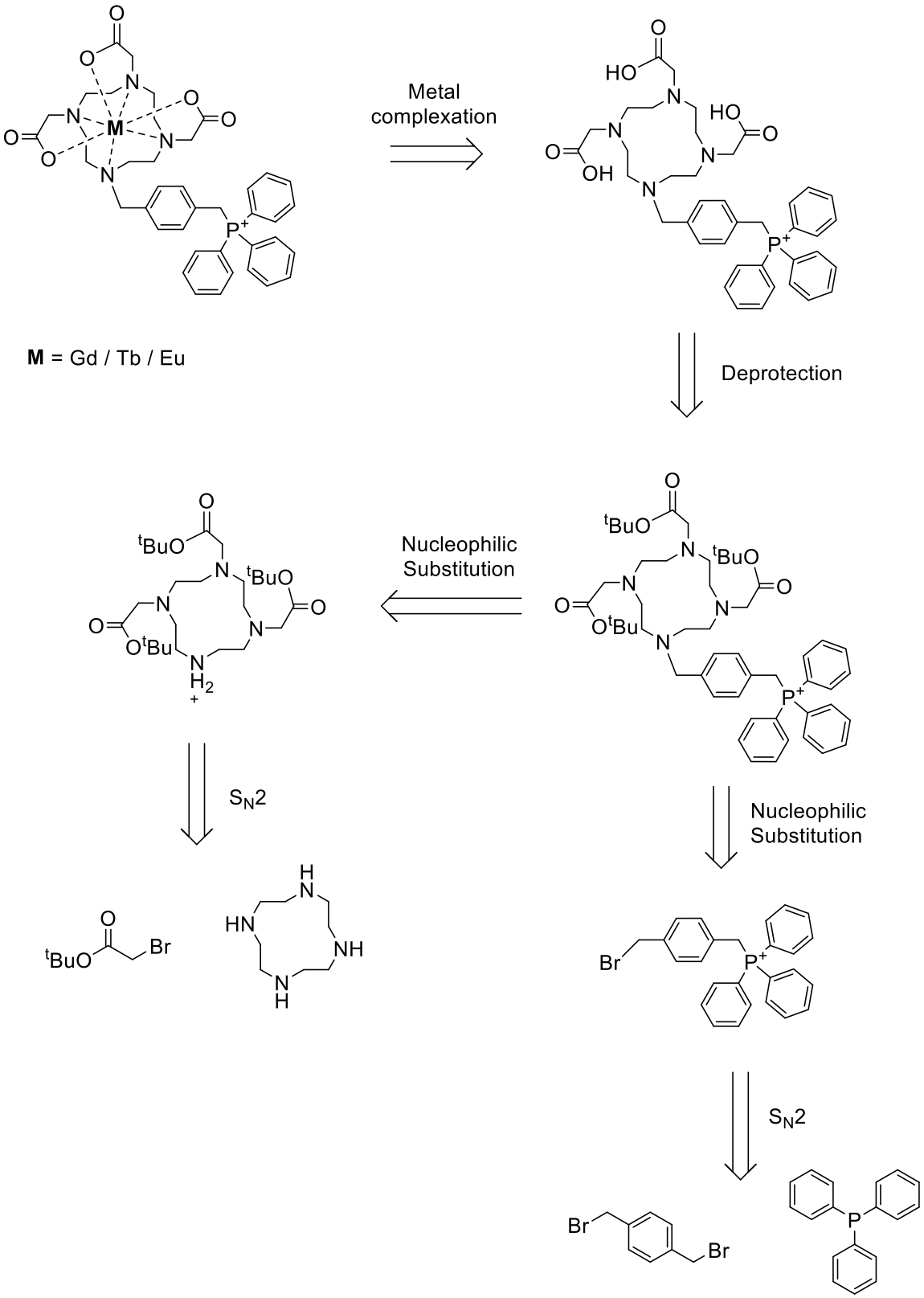

Scheme 1: Retrosynthetic analysis of first-generation lanthanoid(III) complexes (**M** = Gd, Eu, and Tb), detailing the disconnection of the final lanthanoid metal complex into its precursors.

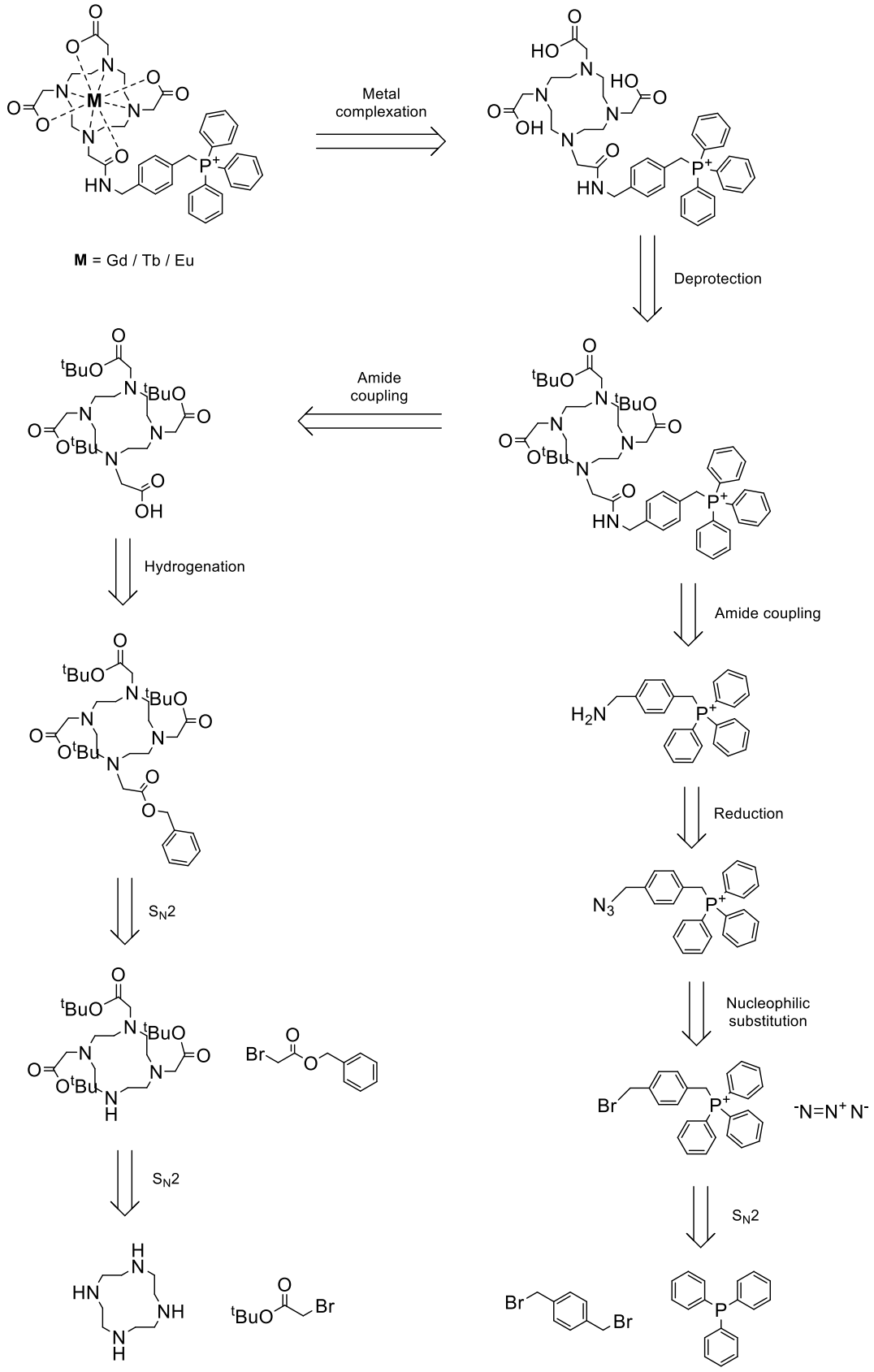

Scheme 2: Retrosynthetic analysis of second-generation lanthanoid(III) complexes (**M** = Gd, Eu, and Tb), detailing the disconnection of the final lanthanoid metal complex into its precursors.

2.2 – Synthesis of Macrocycles

2.2.1 – Formation of the protected triester

The first step undertaken, common to all final products, was the formation of the *tert*-butyl protected DO3A species (Scheme 3). This protection was necessary as the carboxylic acid pendant arms are able to participate in a number of reactions that would have yielded unwanted by-products. Conveniently, the *tert*-butyl groups were able to be readily removed later in the reaction pathway by means of an efficient and high-yielding TFA deprotection reaction.

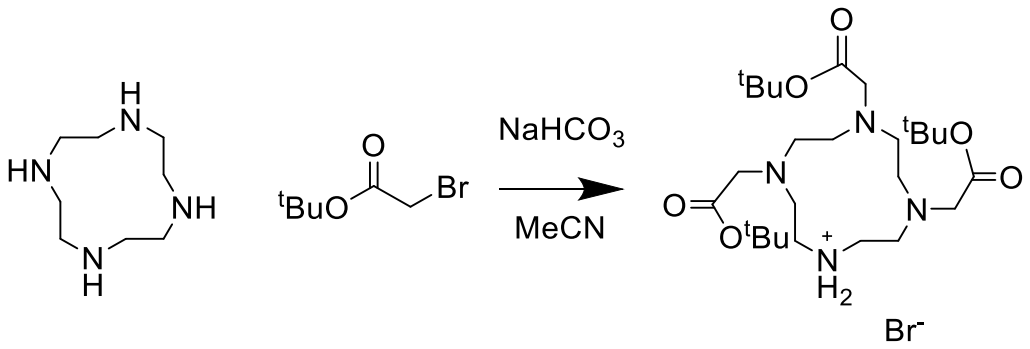

Scheme 3: Formation of protected DO3A triester from cyclen and *tert*-butyl bromoacetate.

This reaction followed a standard S_N2 substitution mechanism, however some considerations were necessary to ensure the generation the triester product while preventing over-alkylation to the tetraester. This was essentially controlled through the precise stoichiometry of the starting materials, which used 3 equivalents of the *tert*-butyl bromoacetate. Furthermore, the reaction was temperature controlled (20°C), in an effort to prevent the over-alkylation of the triester. Sodium bicarbonate was used as a base in order to deprotonate the cyclen, which subsequently enabled the progression of the S_N2 reaction, whereby a nucleophilic nitrogen lone electron pair of the macrocycle was able to attack the electrophilic alpha carbon of the benzyl bromoacetate. To further facilitate the nucleophilic substitution reaction, acetonitrile was utilised, being a polar aprotic solvent system. Inevitably, some impurities were formed, however the crude product was able to be recrystallised from toluene as a pure compound.

The formation of the final product was monitored and confirmed by means of ESI mass spectrometry, with the $[M]^+$ molecular ion peak appearing at *m/z* 515.41 (calculated *m/z* 515.38). Additionally, the ^{1}H NMR spectrum exhibited the ^{t}Bu hydrogen peaks in a 2:1 ratio, as was expected for the triester. This integration was not expected to be observed in either of the mono, di or tetra substituted products, thus confirming the generation of the desired tri-substituted species.

This was the only step required in the synthesis of the macrocycles for the first-generation complexes as well as the related naphthyl derivatives. The second-generation complexes required further modification of the macrocyclic moiety, which is outlined below.

2.2.2 – Further substitution of protected triester

For the second generation compounds, further functionalisation of the cyclen triester was needed in order to generate a suitable species for the coupling reaction to the TPP moiety. This involved the addition of a benzyl acetate group to the triester as a fourth pendant arm, which was subsequently hydrogenated to form a carboxylic acid group (Scheme 4).

In the first reaction, potassium carbonate was used as a base, again to deprotonate the cyclen triester species, facilitating the S_N2 reaction. This reaction mixture was heated under reflux in order to increase the reaction rate and overcome any steric restrictions. In order to facilitate purification, the cyclen triester was used in slight excess, as the cyclen triester was easier to remove from the final product by a washing protocol. Whilst silica gel chromatography would have potentially increased its purity, this compound has previously been found to degrade on silica gel and thus this purification method was not employed here. The reaction progress was able to be effectively monitored using ESI-MS, with the $[M]^+$ molecular ion of the benzyl acetate substituted product peak appearing at *m/z* 685.43 (calculated *m/z* 685.42).

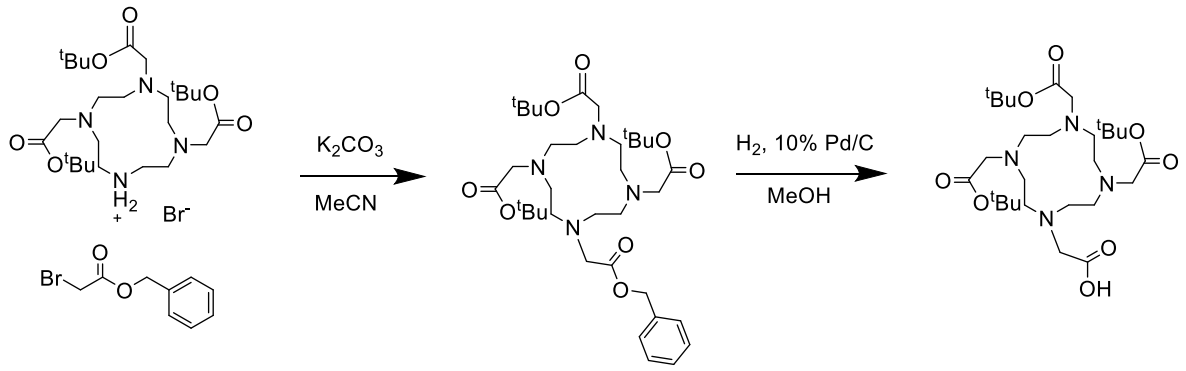

Scheme 4: Further functionalisation of DO3A triester, including the addition of a benzyl acetate arm and subsequent hydrogenation of this group to the corresponding free carboxylic acid.

Conveniently, the benzyl acetate protecting group is orthogonal to the *tert*-butyl protecting groups on the other pendant arms, meaning that the benzyl acetate group could be selectively deprotected without affecting the other pendant arms. The second reaction involved the hydrogenation of the benzyl acetate substituent using gaseous H_2 over a 10% Pd/C catalyst. The reaction was monitored with both TLC and ESI-MS, with [M^+] appearing at *m/z* 595.37 (calculated *m/z* 595.37), and filtered off through a bed of Celite upon completion in order to remove the insoluble Pd/C catalyst.

In the ^{1}H NMR spectrum of the carboxylic acid product, the absence of peaks in the aromatic region indicated the successful removal of the benzyl ester protecting group. The ^{13}C NMR spectrum further confirmed the generation of the carboxylic acid substituted product, with the disappearance of the aromatic C signals and presence of a new downfield carboxyl C signal at 174.6 ppm.

2.3 – Synthesis of Phosphonium Salts

2.3.1 – Formation of phosphonium bromide

The initial phosphonium bromide compound generated was once again a common reaction step to all of the final compounds generated in this work. The reaction is depicted below (Scheme 5). As the final product formed was a salt, it quickly precipitated out of the non-polar toluene solvent as it was formed, facilitating

collection of the product. Furthermore, this precipitation prevented over reaction to the di-substituted product, providing a degree of control over the reaction. The phosphonium bromide was collected by filtration.

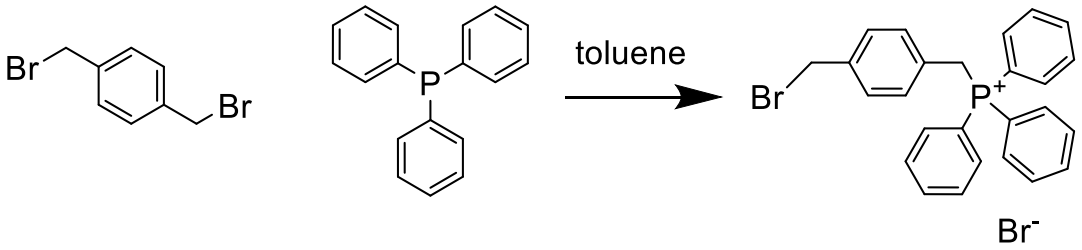

Scheme 5: Formation of phosphonium bromide from triphenylphosphonium and *α,α*'-dibromo-p-xylene starting materials.

The product exhibited the expected molecular-ion peak in the ESI-MS at *m/z* 445.07 (calculated *m/z* 445.07) which was used to monitor the progress of the reaction. Both ^{1}H NMR and ^{13}C NMR spectra indicated the successful generation of the phosphonium bromide product with no sign of contamination by the disubstituted species. Comparing the ^{31}P NMR spectrum of the cationic product to that of triphenylphosphine, it was noted that the peak was shifted downfield from -5.41 to 23.4 ppm.

2.3.2 – Conversion of the phosphonium bromide to a primary amine

In order to perform the amide coupling reactions for the second-generation products, the phosphonium bromide needed to be converted to a phosphonium amine (Scheme 6). First, the phosphonium bromide was reacted with sodium azide. Dimethylformamide (DMF) was used as a solvent, being of sufficiently high polarity to solubilise both the phosphonium bromide salt as well as the sodium azide. This reaction was relatively slow, requiring 72 hours to generate the phosphonium azide product, during which it was monitored with both TLC as well as ESI-MS with the molecular-ion peak appearing at *m/z* 408.15 (calculated *m/z* 408.16).

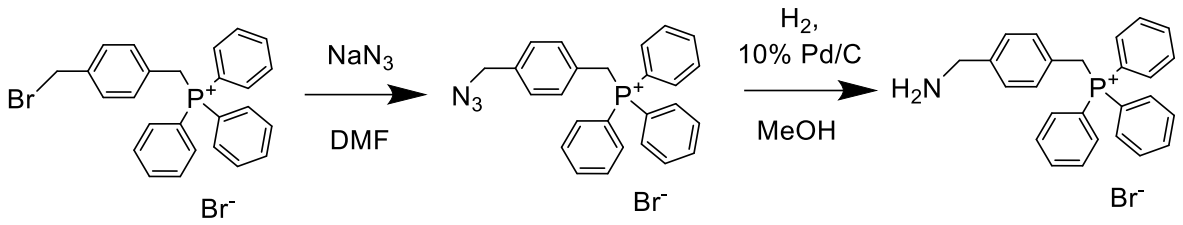

Scheme 6: Further functionalisation of phosphonium bromide to phosphonium azide, followed by its reduction to the phosphonium amine.

After DMF was removed, it was important to quench the potentially unreacted sodium azide which is both a highly toxic and potentially explosive compound. Quenching was achieved by dilution in water, followed by sodium nitrite and 20% (*v/v*) H_2SO_4 addition. This quenching reaction liberated both N_2 and NO gas, generating an acidic solution, which was neutralised with sodium bicarbonate.

Subsequently, the phosphonium azide was reduced to a phosphonium amine through a catalytic hydrogenation reaction using 10% Pd/C. This reaction took approximately 6 hours and formation of the phosphonium amine was monitored by means of TLC using a ninhydrin stain, which revealed the compound as a purple spot on the silica TLC plate. ESI-MS confirmed the formation of product, with the appearance of the molecular-ion peak at *m/z* 382.19 (calculated *m/z* 382.17) and the disappearance of the *m/z* 408.15 peak pertaining to the phosphonium azide. As expected, ^{1}H NMR spectrum displayed a new signal at 2.64 ppm, with an integration of 2:1, corresponding to presence of two amine hydrogen atoms.

2.3.3 – Formation of 2,6-bis(bromomethyl)naphthalene

In order to mitigate the high cost associated with the purchase of 2,6-bis(bromomethyl)naphthalene, a synthetic method was found that utilised in house reagents such as 2,6-dimethylnaphthalene as well as catalytic amounts of NBS and AIBN. The experimental protocol utilised has previously been reported to generate 2,6-bis(bromomethyl)naphthalene with good yields.[114] This reaction is typically performed in carbon tetrachloride solvent, however dichloromethane (DCM) was chosen as a less toxic and more environmentally-friendly alternative. However, due to the relatively low boiling point of DCM (40 ^{o}C), the lower reflux temperature

resulted in a slow reaction, taking approximately 5 days to occur, during which it was monitored using TLC. In future syntheses, an alternative solvent such as acetonitrile may prove to be a more efficient alternative. As expected, in the ^{1}H NMR spectrum, the signals from the methylene H-atoms and the aromatic hydrogens were present in a 2:3 ratio. Additionally, the ^{13}C NMR spectrum demonstrated a number of aromatic peaks in the 126-135 ppm region, as well as the peak of the methylene carbon atom at approximately 34.5 ppm, supporting the successful generation of the 2,6-bis(bromomethyl)naphthalene product.

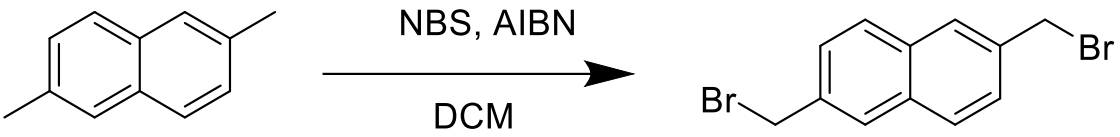

Scheme 7: Formation of 2,6-bis(bromomethyl)naphthalene from 2,6-dimethylnaphthalene

The reaction proceeds by means of the Wohl-Ziegler mechanism, whereby AIBN acts as a radical initiator, enabling Br_2 to be cleaved into two $Br^{\bullet}$ radicals.[115] One $Br^{\bullet}$ radical is then able to abstract a hydrogen from one of the methyl groups of the 2,6-dimethylnaphthalene, generating a methyl radical which subsequently reacts with the other $Br^{\bullet}$ to form the bromo adduct.

2.4 – Coupling Reactions

The generation of the free target phosphonium-DO3A ligand was achieved through the simple S_N2 addition of the DO3A macrocycle to the phosphonium bromide moiety in the case of both the first-generation ligand and its related naphthyl compound. The formation of the second-generation free ligands necessitated the use of the peptide coupling reagents HATU and NMM. In all cases, following the coupling reactions, the free ligand that was generated was deprotected using a 1:1 mixture of DCM / TFA just prior to purification using reverse-phase HPLC.

2.4.1 – First-generation Coupling Reactions

The first-generation coupling reaction is outlined below (Scheme 8). The cyclen triester and phosphonium compounds were reacted together in a 1:1 ratio, using sodium carbonate as a base to deprotonate the triester and facilitate the S_N2 reaction mechanism. The reaction was monitored by means of TLC (with an eluent consisting of a 1:1 mixture of hexane / methanol), as well as using ESI-MS, which clearly indicated the disappearance of the *m/z* 445.07 phosphonium peak. Following the completion of the reaction, the solvent was removed *in vacuo*, and the crude product was re-dissolved in DCM / TFA in order to remove the *tert*-butyl protecting groups.

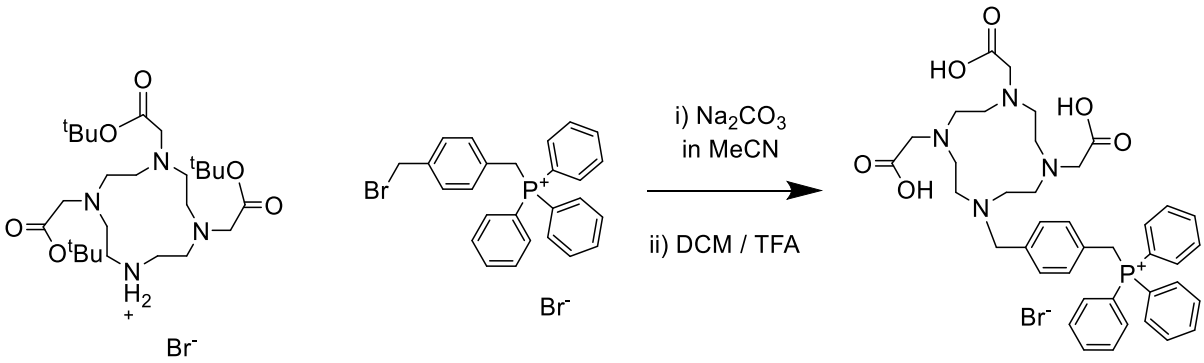

Scheme 8: Coupling of DO3A triester and phosphonium bromide, followed by *tert*-butyl deprotection to form the first-generation free ligand.

The free ligand was unable to be observed using ESI-MS, however, MALDI-TOF MS did reveal the free ligand peak at *m/z* 711.33 (calculated *m/z* 711.33). In the ^{1}H NMR spectrum, many of the signals were overlapping, but a comparison of the integrations was also consistent with the generation of the free ligand.

2.4.2 – Second-generation Coupling Reactions

The second-generation coupling reaction is outlined below (Scheme 9). This reaction utilised both NMM and HATU amide coupling reagents in order to deprotonate the carboxylic acid of the DO3A triester and to prime it for the formation of an amide bond, respectively. The reaction was monitored my means of ESI-MS, noting the disappearance of the phosphonium amine peak at *m/z* 382.17. Following reaction

completion, the solvent was removed *in vacuo*, and the crude product re-dissolved in a 1:1 mixture of DCM / TFA in order to remove the *tert*-butyl protecting groups. Again, the free ligand product was not detectable by means of ESI-MS, necessitating the use of MALDI-TOF MS for the confirmation of the free ligand molecular-ion peak at *m/z* 761.56 (calculated *m/z* 761.35). The formation of the free ligand product was further confirmed by means of ^{13}C NMR as well as ^{1}H NMR spectroscopy, which both showed characteristic peaks and, in the latter case, integrals and splitting patterns characteristic of the second-generation ligand.

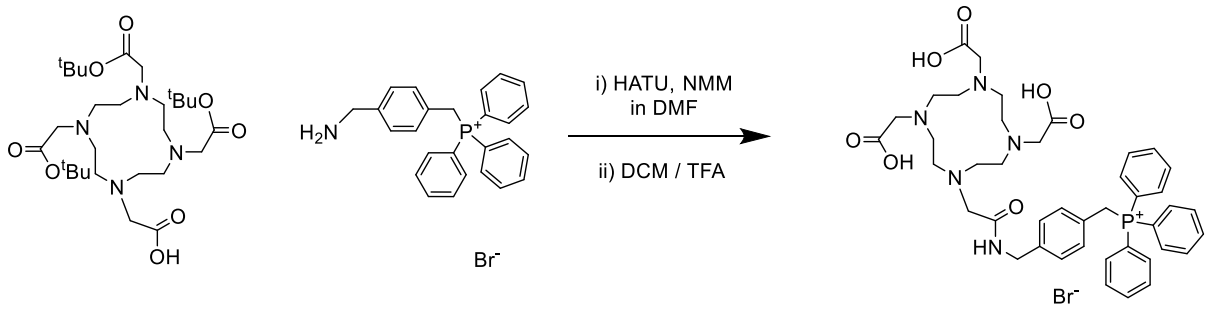

Scheme 9: Coupling of carboxylic acid substituted DO3A triester and phosphonium amine, followed by *tert*-butyl deprotection to form the second-generation free ligand.

While this procedure served as an effective method for generating the desired free ligand, there are a number of unfavourable toxicities associated with the coupling reagents, including respiratory and skin sensitisation in the case of NMM and acute eye / oral toxicity in the case of HATU. As a result, a safer experimental method was attempted, which endeavoured to utilise a S_N2 reaction between the phosphonium amine and chloroacetyl chloride. While this step was successful, the intention was then to perform a carbonyl neutrophilic addition reaction between the cyclen triester and the phosphonium compound. Unfortunately, this step proved unsuccessful, likely due to steric effects of the triester impeding the addition reaction.

2.4.3 – HPLC Purification

The deprotected, free ligands generated in this work were purified by means of reversed-phase HPLC. In both analytical and preparative HPLC methods, the mobile phase was run in a gradient from 100% ammonium acetate to 100% acetonitrile (over 30 minutes for first-generation and 60 minutes for second-generation ligands)

using multi-channel detection. The first-generation complexes were found to elute at approximately the 19 minute mark, whereas the second-generation complexes were eluted at approximately the 15 minute mark. An example of a typical HPLC chromatogram for the first-generation complexes is provided below (Figure 16).

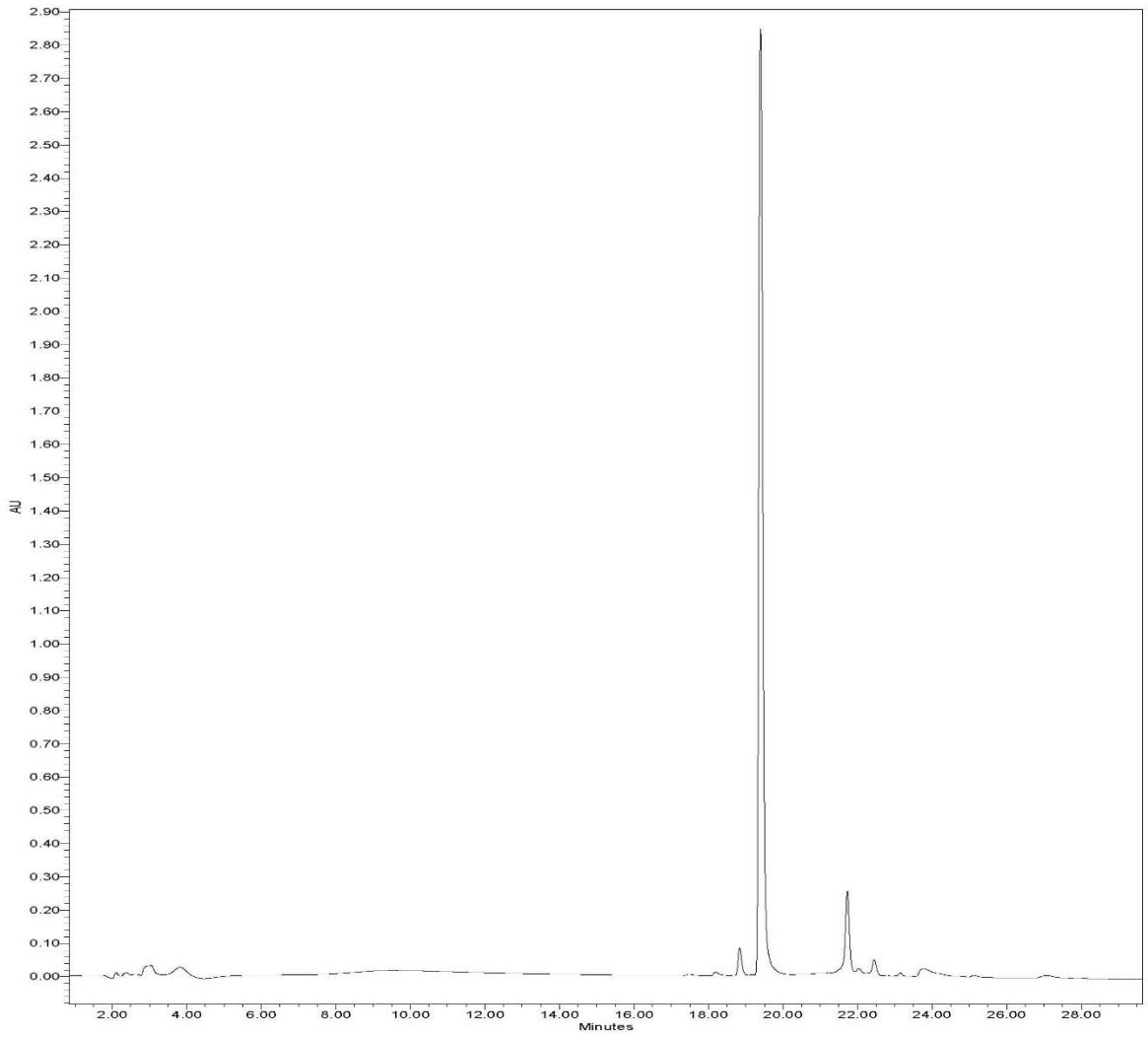

Figure 16: HPLC trace of the first-generation free ligand using multi-channel detection, showing ligand elution at approximately 19 minutes.

2.5 – Formation of Lanthanoid Complexes

The formation of the lanthanoid complexes from the free ligands was generally a straightforward process. Each ligand was separately metalated using lanthanoid oxides, including Gd_2O_3, Tb_4O_7 and Eu_2O_3 for the generation of gadolinium(III), terbium(III) and europium(III) complexes, respectively. The reactions were conducted

in MilliQ water, and whilst the lanthanoid oxides used were fairly insoluble (necessitating use of an excess amount of lanthanoid oxide), they were able to deprotonate the carboxylic acid arms of the free ligands due to their basic nature, thereby facilitating complexation. These reactions were performed at 80 ^{o}C, and reaction progress was monitored by means of MALDI-TOF MS. Following the formation of the complexes, the reaction mixture was passed through a 0.2 µm PTFE syringe filter and lyophilised under high vacuum. Generalised metalation reactions for both the first- and second-generation complexes are presented below (Schemes 10 and 11, respectively).

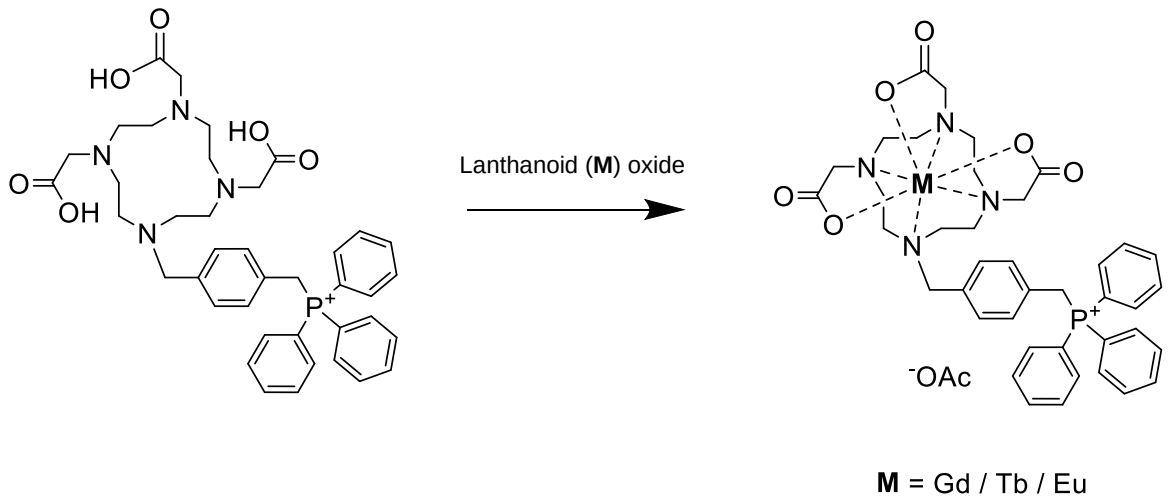

Scheme 10: Metalation reaction of first-generation ligand, with **M** = Gd (using Gd_2O_3), Tb (using Tb_4O_7) or Eu (using Eu_2O_3).

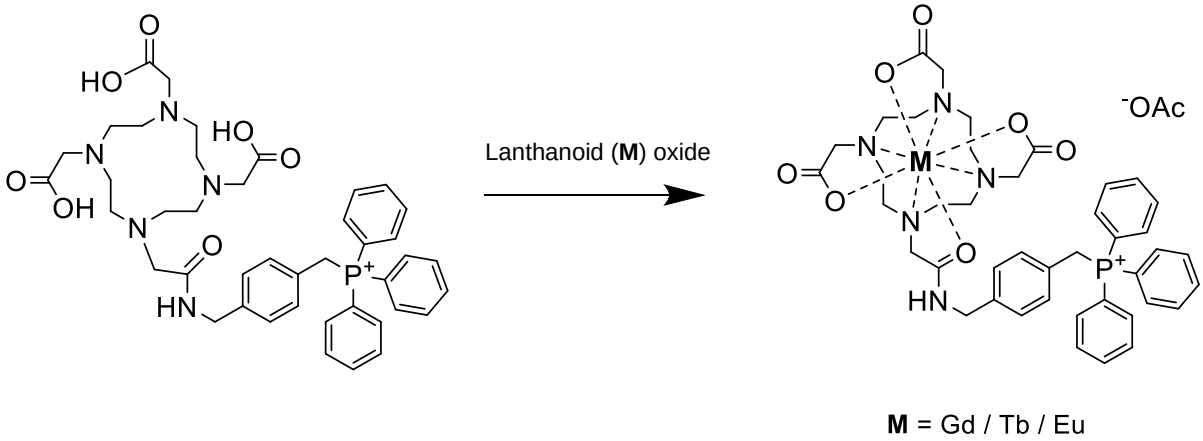

Scheme 11: Metalation reaction of second-generation ligand, with **M** = Gd (using Gd_2O_3), Tb (using Tb_4O_7) or Eu (using Eu_2O_3).

Due to the high number of unpaired electrons within each of these lanthanoid centres, NMR peaks were broadened to the point that useful structural information and coherent NMR spectra were unable to be obtained. As such, these compounds were characterised based on MALDI-TOF MS, with their purities confirmed using analytical HPLC. Example MALDI-TOF MS spectra of the first-generation Gd(III) complex as well as the second-generation Tb(III) complex are provided (Figures 17 and 18, respectively). These traces compare the trace obtained to that calculated for each complex. The high degree of similarity between experimental and calculated MS supports the successful generation of these complexes.

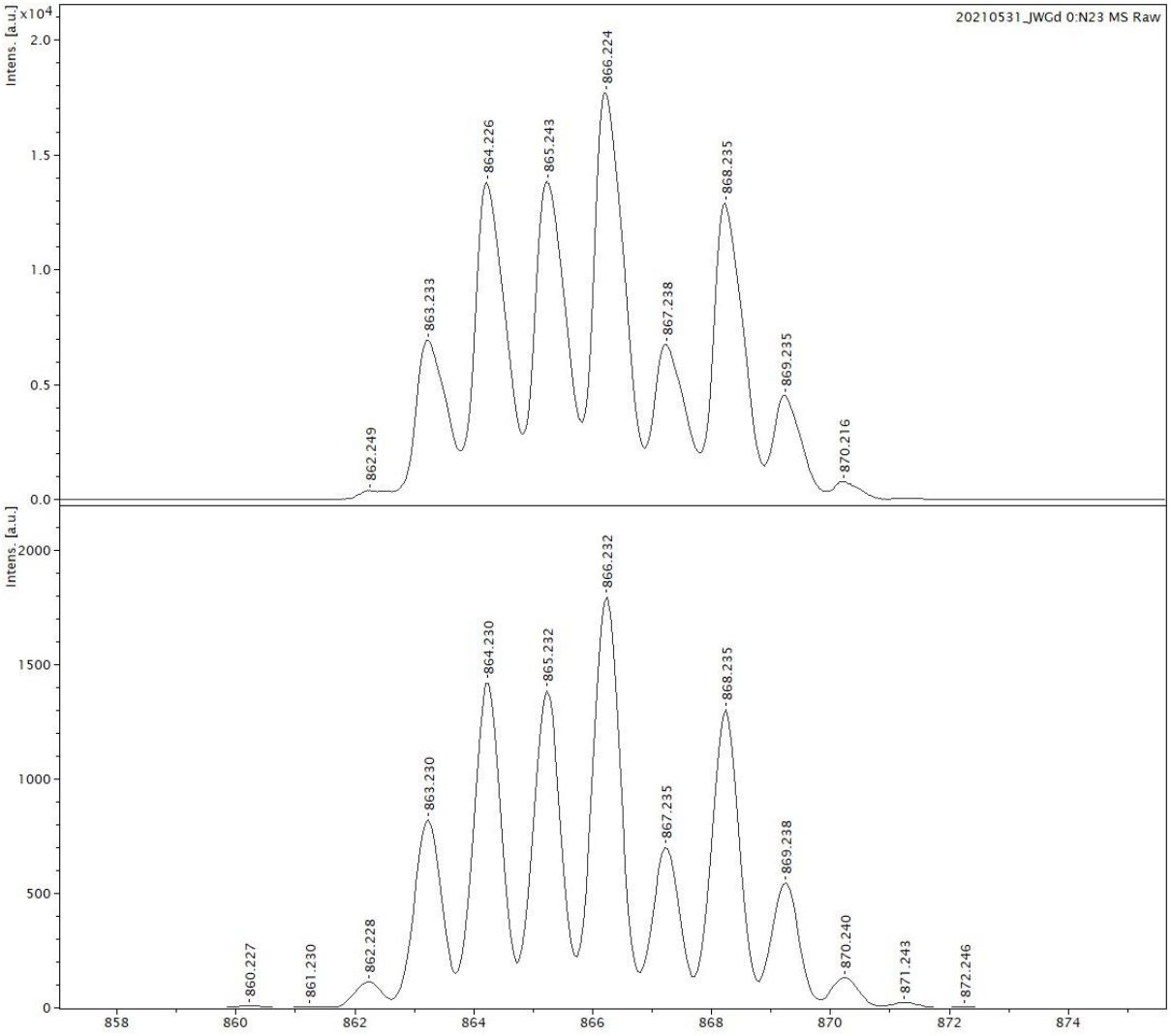

Figure 17: MALDI mass spectrometry trace obtained for the first-generation Gd(III) complex (top) compared to the calculated MS for this complex (bottom).

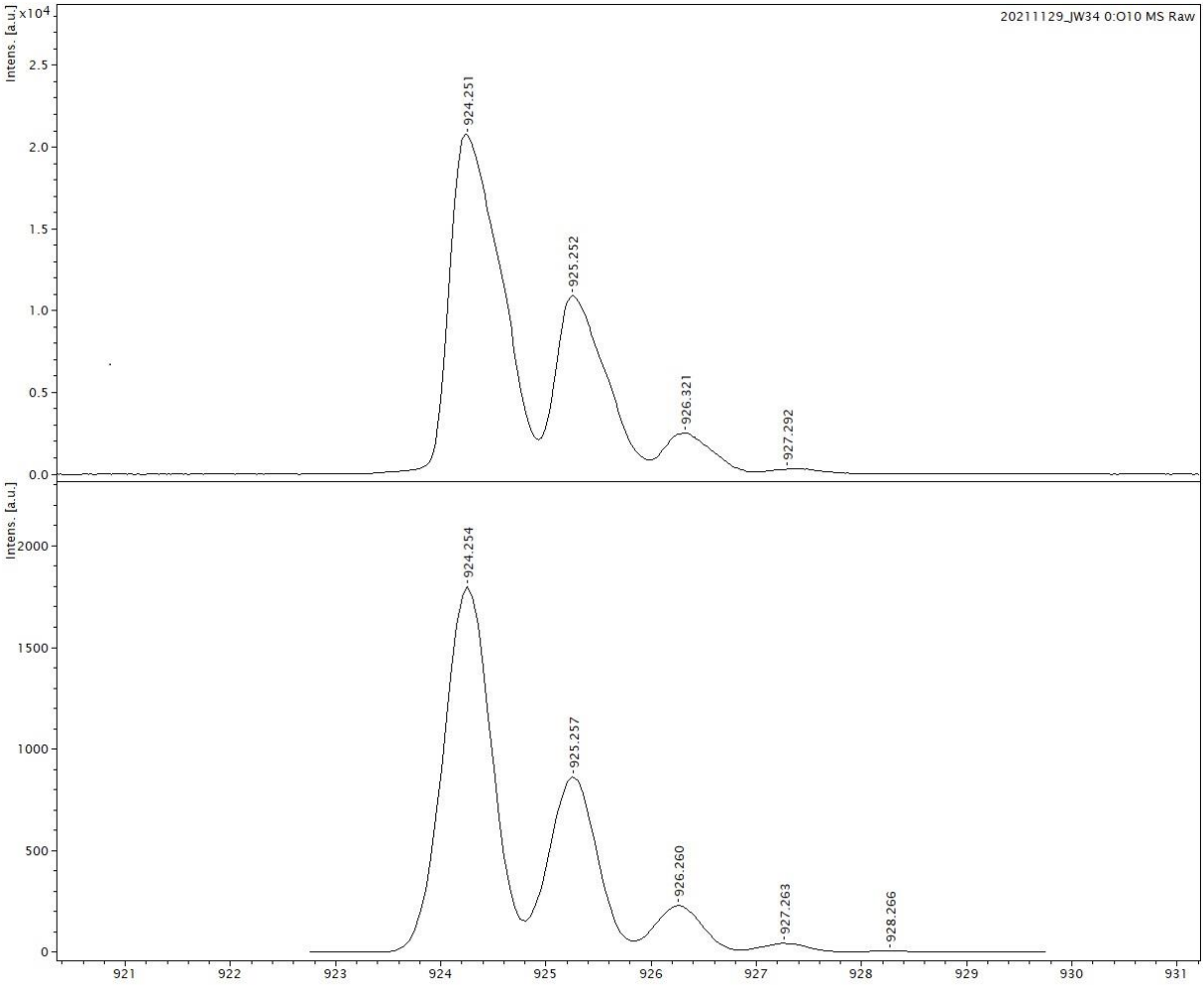

Figure 18: MALDI-TOF MS spectrum obtained for the second-generation Tb(III) complex (top) compared to the calculated MS for this complex (bottom).

Interestingly, the free ligand peak was present within both of these mass spectra, at *m/z* 711.33 for the first-generation complexes and *m/z* 761.35 for the second-generation complexes. These peaks remained constant, regardless of any increased reaction times and/or temperatures, indicating that they were most likely artifacts of the MS analyses, i.e. partial demetallation of the complexes during the laser assisted desorption process within the mass spectrometer, rather than incomplete reactions. Indeed, HPLC traces confirmed the purity of the metal complexes.

With the lanthanoid(III) complexes in hand, comprehensive fluorescence and cell uptake experiments could be conducted, the results of which are presented in the next chapter.

Chapter 3

Fluorescence and Biological Studies

3.1 – Fluorescence Spectra

Given the importance of characterising the fluorescence properties of the new lanthanoid(III) complexes **13**, **14** and **16**-**20** prior to conducting confocal microscopy studies involving cells, the excitation and emission spectra of these complexes were investigated (Figures 19-25).

The fluorescence spectra typically had an excitation peak at approximately 230 nm (Figures 19-25), which is attributed to sensitisation of the xylyl / naphthyl linker group. It is interesting, however, that a 230 nm excitation peak and characteristic fluorescent emission was still observed even when *n*-butyl linker group was used (Figures 23 and 24; ligands prepared previously by Dr Andrew Hall). It is proposed that this is possibly the result of some degree of sensitisation by the TPP moiety. Furthermore, the excitation peaks around 450 nm were somewhat unexpected and, as these were absent in the free ligand, are thought to be due to two-photon excitation processes.

The emission spectra observed are typical for Eu and Tb complexes, with the strongest emission peaks observed at 616 and 545 nm, respectively (Figures 19-25). For the Eu spectra (Figures 19, 21, 23), the emission peaks correspond to the $^5D_0 \rightarrow {}^4F_J$ (J = 0-6) transitions, with the peak emission at 616 nm corresponding to the $^5D_0 \rightarrow {}^4F_2$ transition.[93] For the Tb spectra (Figures 20, 22, 24, 25), the emission peaks correspond to the $^5D_4 \rightarrow {}^4F_J$ (J = 0-6) transitions, with the peak emission at 545 nm corresponding to the $^5D_4 \rightarrow {}^4F_5$ transition.[93]

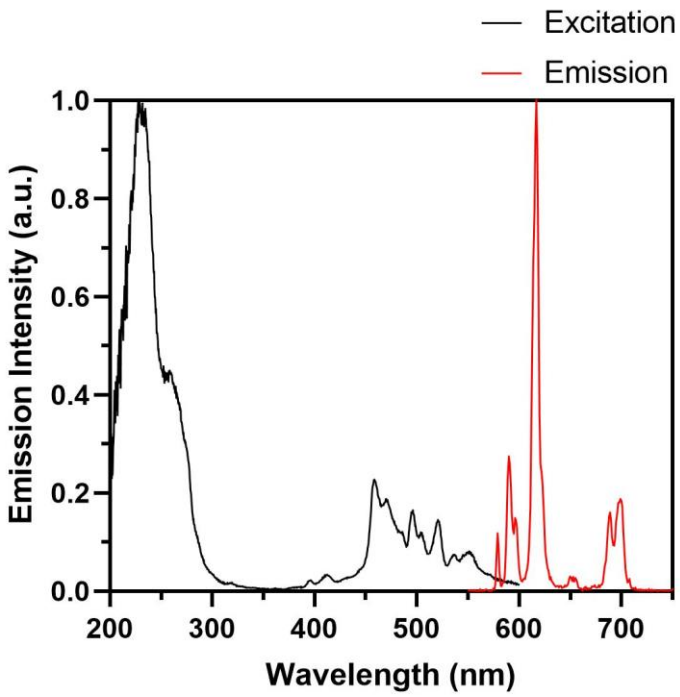

Figure 19: Normalised fluorescence excitation spectrum (λ_{em} = 616, black) and emission spectrum (λ_{ex} = 230, red) for **13**.

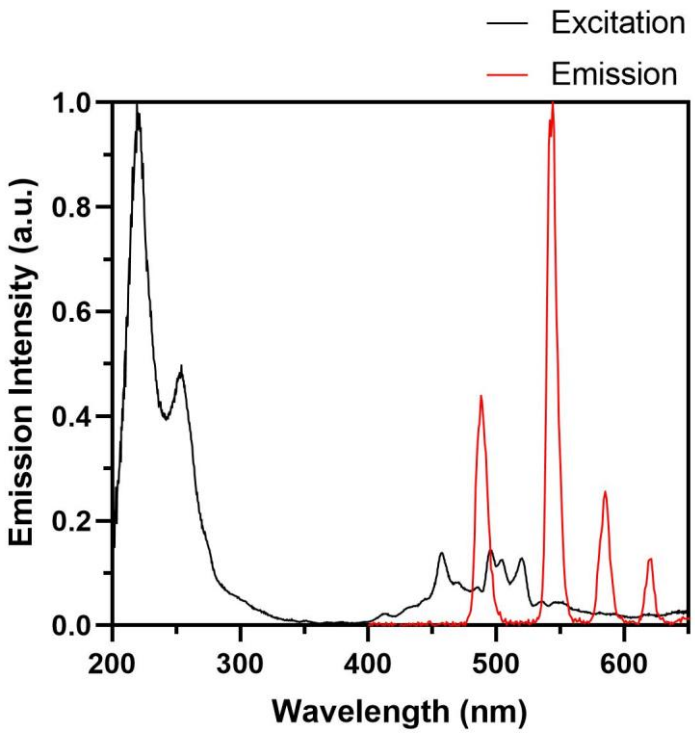

Figure 20: Normalised fluorescence excitation spectrum (λ_{em} = 545, black) and emission spectrum (λ_{ex} = 230, red) for **14**.

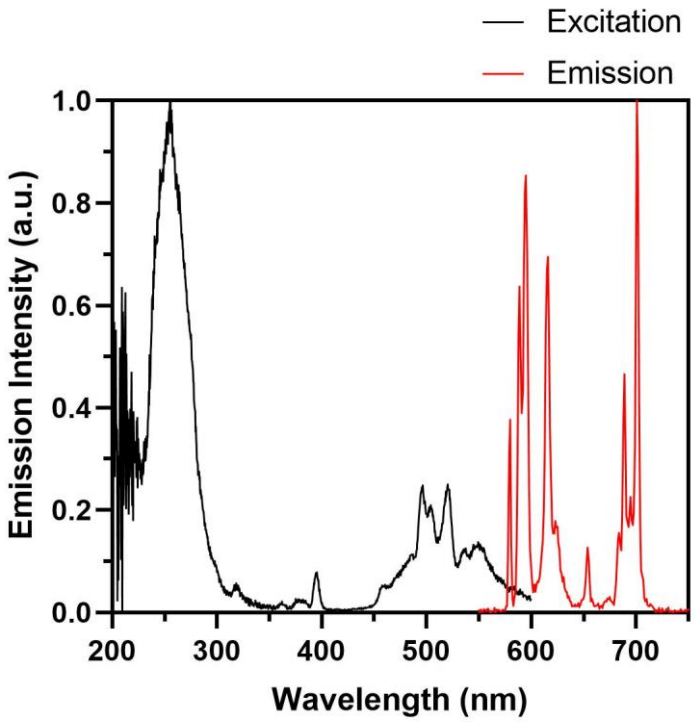

Figure 21: Normalised fluorescence excitation spectrum (λ_{em} = 616, black) and emission spectrum (λ_{ex} = 230, red) for **16**.

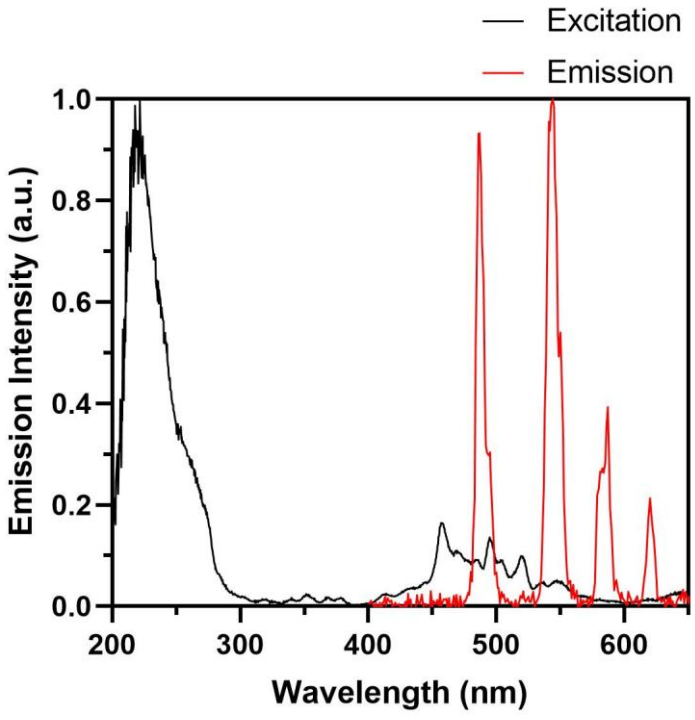

Figure 22: Normalised fluorescence excitation spectrum (λ_{em} = 545, black) and emission spectrum (λ_{ex} = 230, red) for **17**.

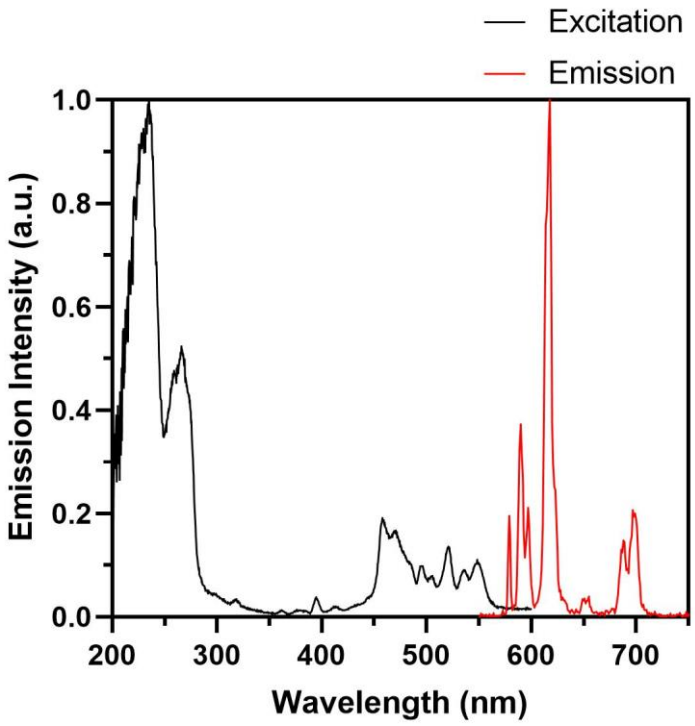

Figure 23: Normalised fluorescence excitation spectrum (λ_{em} = 616, black) and emission spectrum (λ_{ex} = 230, red) for **18**.

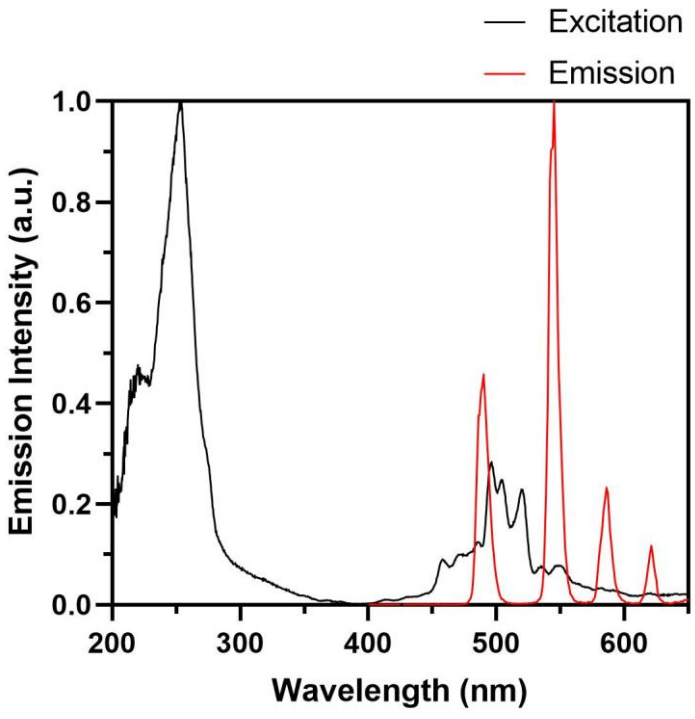

Figure 24: Normalised fluorescence excitation spectrum (λ_{em} = 545, black) and emission spectrum (λ_{ex} = 230, red) for **19**.

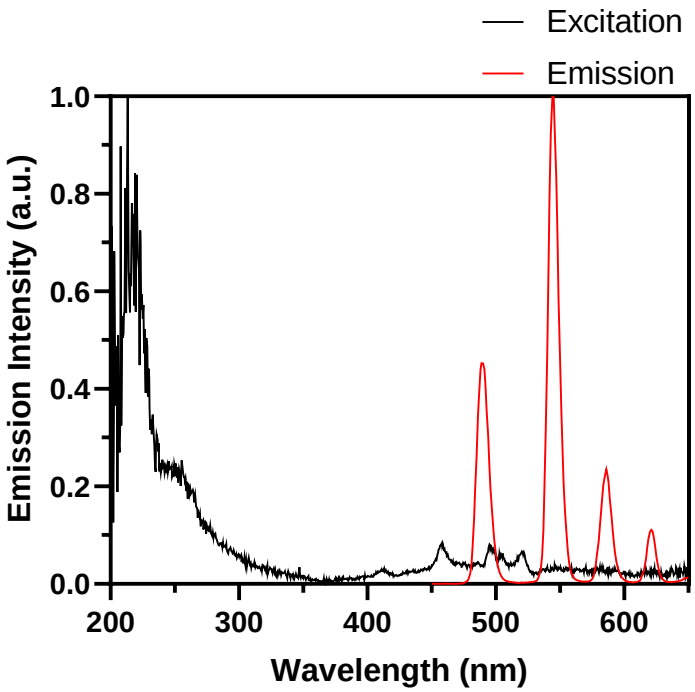

Figure 25: Normalised fluorescence excitation spectrum (λ_{em} = 545, black) and emission spectrum (λ_{ex} = 230, red) for **20**.

3.2 – *q*-values

Given that the complexes are essentially solvated by water in the confocal fluorescence microscopy experiments, it is important to explore the effect of vibrational quenching on the overall fluorescent yields for the lanthanoid(III) metal complexes. Water-induced vibrational quenching is predominantly caused by the O-H stretch oscillation which is a competitive deactivation pathway when the energy gap between the excited and receiving states of the Ln(III) ion is less than 6 quanta of the quenching vibration.[93]

One strategy to minimise vibrational quenching is to use a ligand system that coordinates the Ln(III) centre at as many sites as possible, in order to block the binding of potentially deactivating ligands. It is therefore useful to ascertain the number of binding sites within the first coordination sphere of the lanthanoid metal centre that are occupied by water molecules.

This was done through the calculation of *q* values (Table 3), which essentially represent the number of water molecules within the first coordination sphere of the lanthanoid(III) centre. These *q* values were calculated using the modified Horrocks equation, which calculates *q* as a function of the fluorescence decay constants of the lanthanoid(III) complex in both H_2O and D_2O.[116] The modified Horrocks equation is as follows:

$$q = A\left(\frac{1}{\tau_{H_2O}} - \frac{1}{\tau_{D_2O}} - B\right)$$

where *A* functions as a proportionality constant, reflecting the sensitivity of the Ln(III) ion to vibronic quenching; *τ* represents the luminescence lifetime; and B functions as a correction factor to account for outer sphere quenching. For europium(III), A = 1.2, B = 0.25 and for terbium(III), A = 5.0 and B = 0.06.[116]

Table 3: Luminescence lifetimes for compounds **13**, **14**, **16**-**20** in H_2O and D_2O as well as the standard deviation of the average calculated *q* values.

Compound	τ_{H2O} (ms)	τ_{D2O} (ms)	*q*	SD of *q*
13	0.47	5.1	2.0	0.02
14	1.0	2.3	2.4	0.03
16	0.61	2.4	1.2	0.02
17	1.6	3.5	1.4	0.00
18	0.41	1.6	1.9	0.01
19	1.4	2.7	1.4	0.01
20	0.66	1.4	0.65	0.03

As expected, the *q* values of complexes **13**, **14**, **18** and **19** were closer to 2 (Table 3), indicating that these lanthanoid metal centres had approximately two available coordination sites that water was able to occupy. Note, that these numbers typically are not integers as, in solution, a multitude of probable steric arrangements likely exists, and thus the *q* values reported represent the overall mean coordination number. Complexes **16** and **17** had *q* values closer to 1 (Table 3), most likely as a result of the carbonyl oxygen of the secondary amide group preferentially coordinating the nearby lanthanoid(III) centre and thus occupying one of the binding sites that water would have otherwise occupied. Finally, the lower *q* value observed

for complex **20** was possibly due to steric hinderance from the larger naphthyl group, preventing water from coordinating the lanthanoid centre effectively.

An example of fluorescence decay spectrum of **14** is provided, containing the exponential decay curve fit and best fit values (Figure 26).

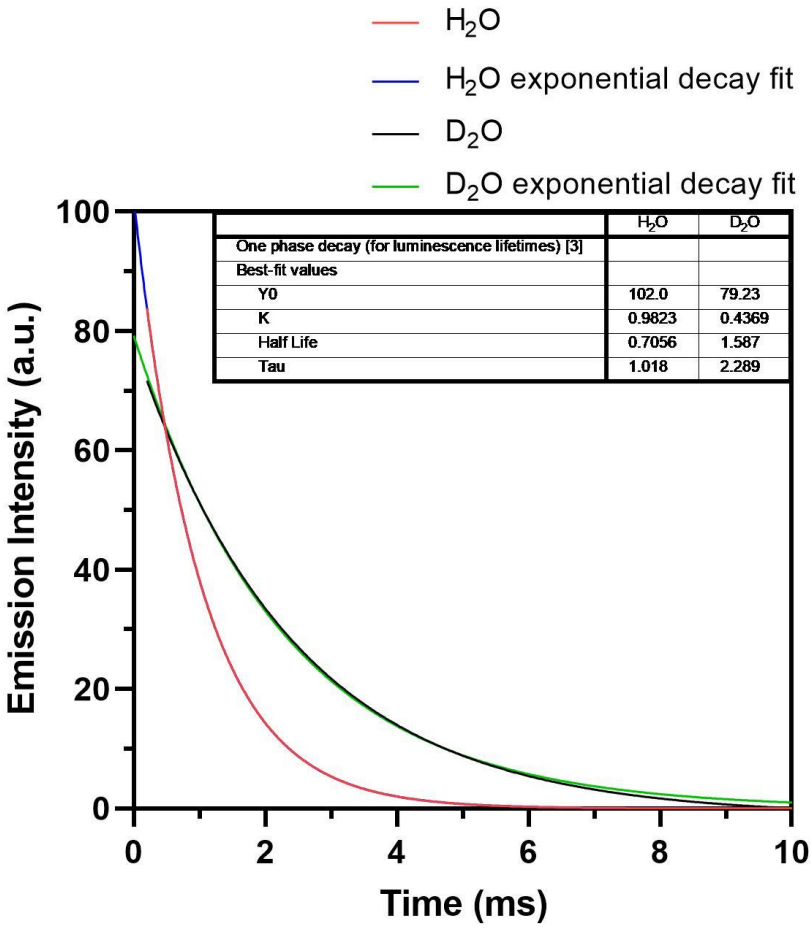

Figure 26: Example fluorescence decay by delay spectrum (λ_{ex} = 230, λ_{em} = 545) and exponential decay curve fitting of **14** in both H_2O (data in red; fit in blue) and D_2O (data in black, fit in green). Best-fit values are displayed.

3.3 – Confocal Fluorescence Microscopy

Compounds **13**, **14**, **16** and **17** were selected for further exploration by confocal fluorescence microscopy, as archetypical analogues with ligand, linker and DLC

moieties that have previously shown promise as potential theranostics and have therefore been extensively characterised.[77,81] Furthermore, these complexes exhibited excellent fluorescence properties (Section 3.2) and the first- and second-generation complexes differ in structure, thereby offering an interesting point of comparison.

The MitoTracker Deep Red® (MTDR) mitochondrial fluorescent imaging probe was used to stain the mitochondria of both the human glioma (T98G) and normal human glial (SVG-p12) cells that were treated with the complexes. This was done in order to perform co-localisation analyses, and also determine the intracellular localisation of the complexes.

A quantitative summary of the microscopy images generated (Figures 27-34) is presented below (Table 4), whereby Pearson's Coefficient measures the overall co-localisation between the lanthanoid complex and MTDR; the M1 Mander's Coefficient quantifies the co-localisation as a proportion of the MTDR fluorescent signal; and the M2 Mander's Coefficient quantifies the co-localisation as a proportion of the complex fluorescent signal.

Table 4: Calculated Pearson's Coefficient's and M1 and M2 Manders Coefficients for co-localisation between complexes **13**, **14**, **16**, **17** and MTDR. All calculations were conducted using the ImageJ Coloc2® plug-in.

	Complex	Pearson's Coefficient	M1 Mander's Coefficient	M2 Manders Coefficient
SVG-p12	**13**	0.29	0.41	0.24
	14	0.26	0.54	0.12
	16	0.072	0.42	0.009
	17	0.02	0.03	0.97
T98G	**13**	0.41	0.69	0.28
	14	0.43	0.61	0.34
	16	0.32	0.19	0.15
	17	0.25	0.35	0.13

As expected from the Nernst equation,[50] there was considerably higher co-localisation of the complexes with MTDR in the T98G cancer cell line, compared to the SVG-p12 glial fibroblast cell line (Table 4, Figures 27-34), owing to the higher mitochondrial membrane potential within cancer cells.[58,66] Interestingly, complexes **13** and **14** appeared to have a higher degree of co-localisation with the MTDR probe, compared to complexes **16** and **17** (Table 4, Figures 27-34), which possessed the secondary amide group within the linker. It is likely that the presence of the polar amide group made it more difficult for complexes **16** and **17** to cross lipophilic phospholipid membranes, resulting in less co-localisation.

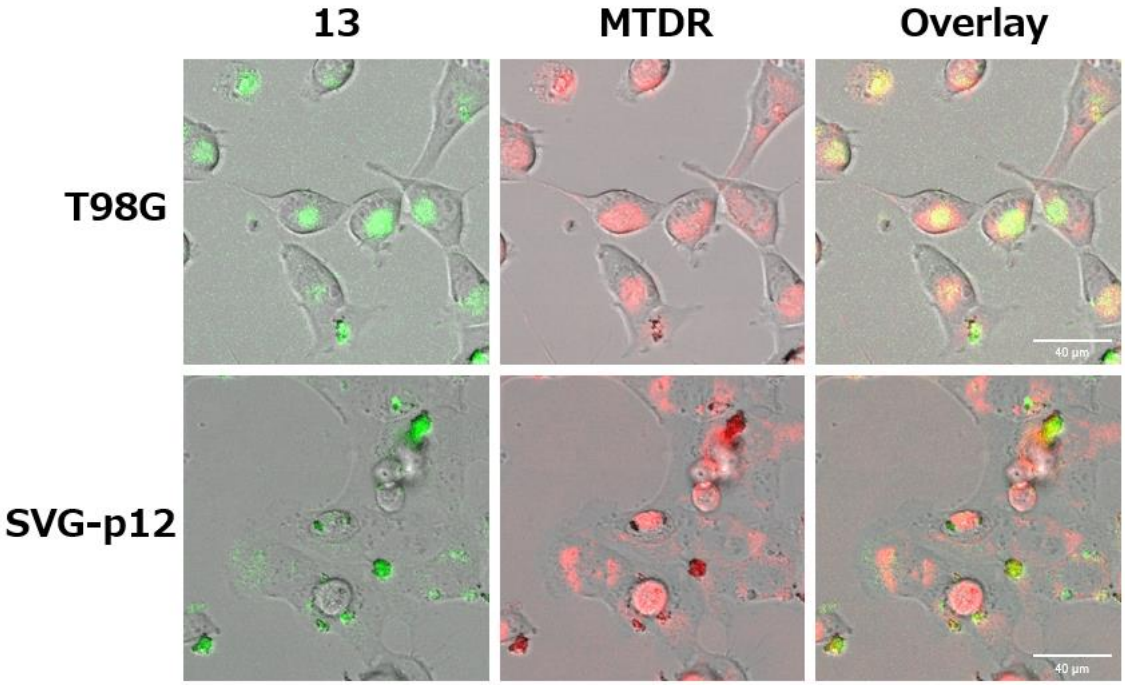

Figure 27: Fluorescence microscopy image of complex **13**, MTDR, and overlay in both T98G and SVG-p12 cell lines (4 x zoom). Images were captured by means of a Leica SP5 II Confocal and Multiphoton microscope, and overlayed using ImageJ.

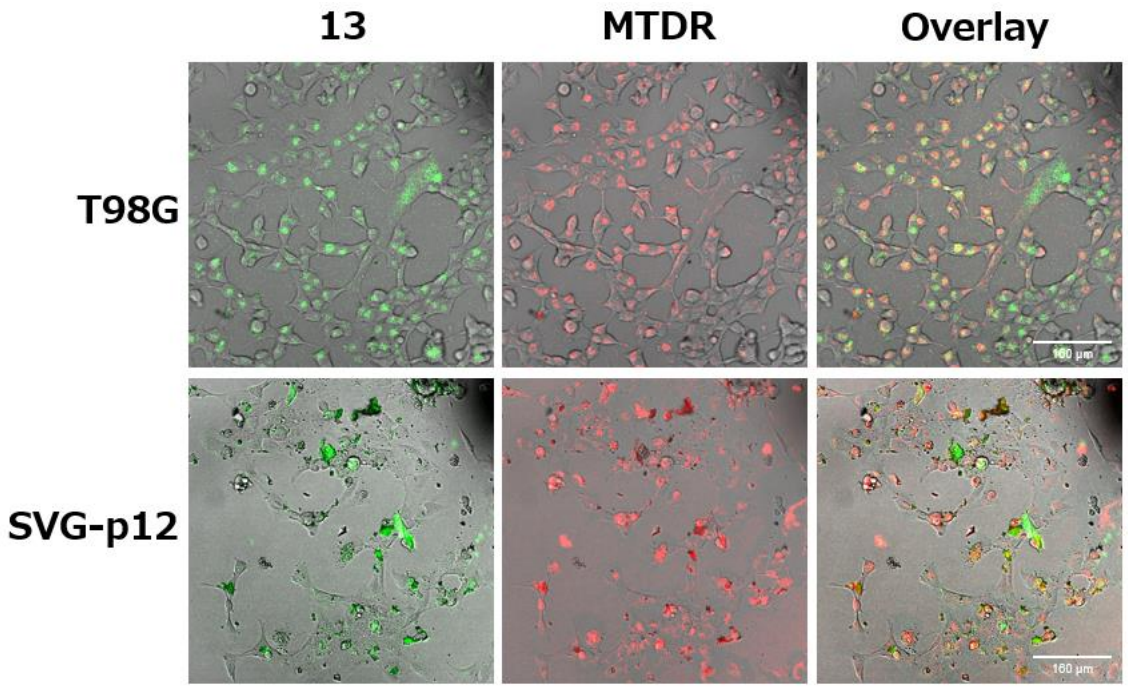

Figure 28: Fluorescence microscopy image of complex **13**, MTDR and overlay in both T98G and SVG-p12 cell lines (1 x zoom). Images were captured on a Leica SP5 II Confocal and Multiphoton microscope, and overlayed using ImageJ.

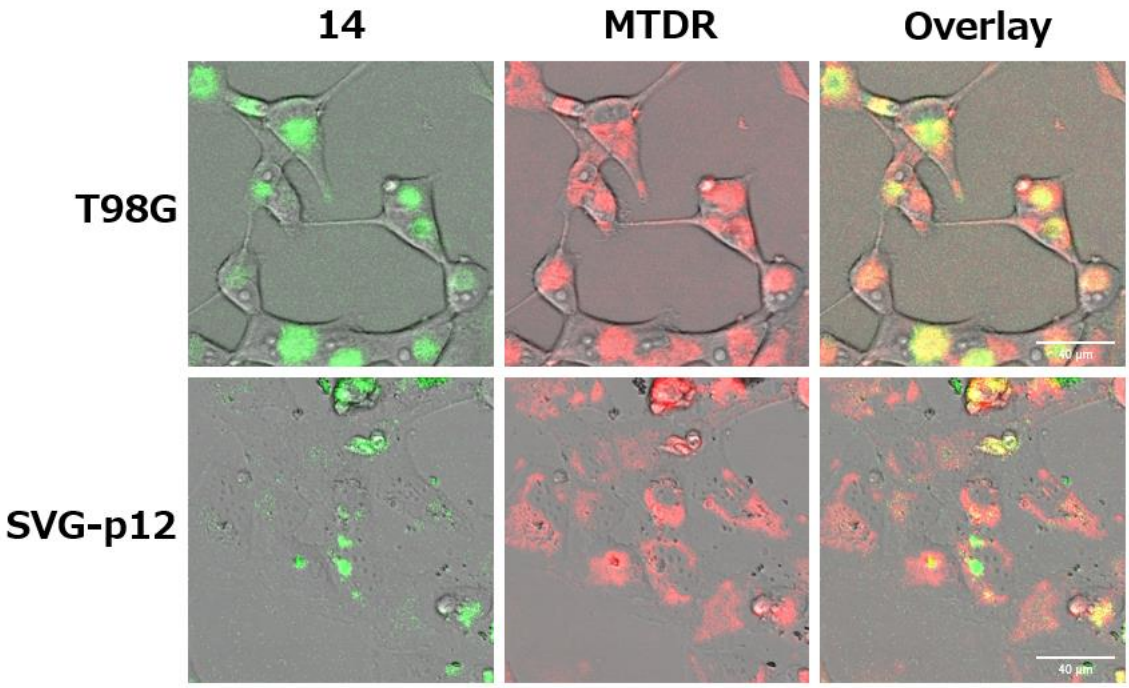

Figure 29: Fluorescence microscopy image of complex **14**, MTDR and overlay in both T98G and SVG-p12 cell lines (4 x zoom). Images were captured on a Leica SP5 II Confocal and Multiphoton microscope, and overlayed using ImageJ.

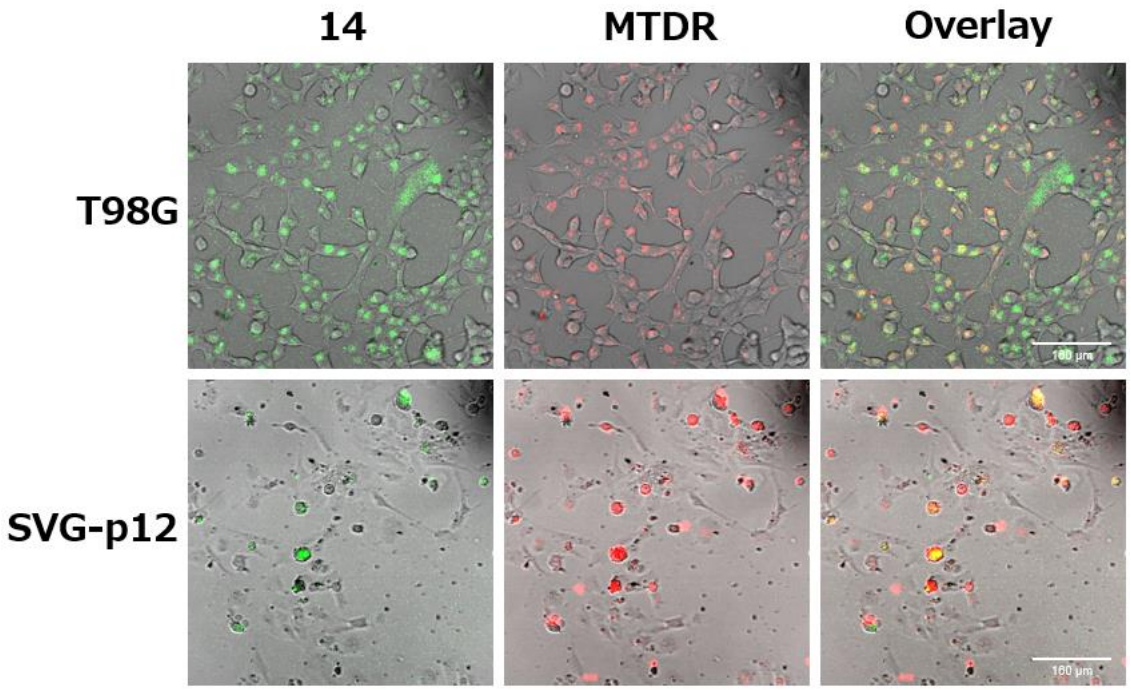

Figure 30: Fluorescence microscopy image of complex **14**, MTDR and overlay in both T98G and SVG-p12 cell lines (1 x zoom). Images were captured on a Leica SP5 II Confocal and Multiphoton microscope, and overlayed using ImageJ.

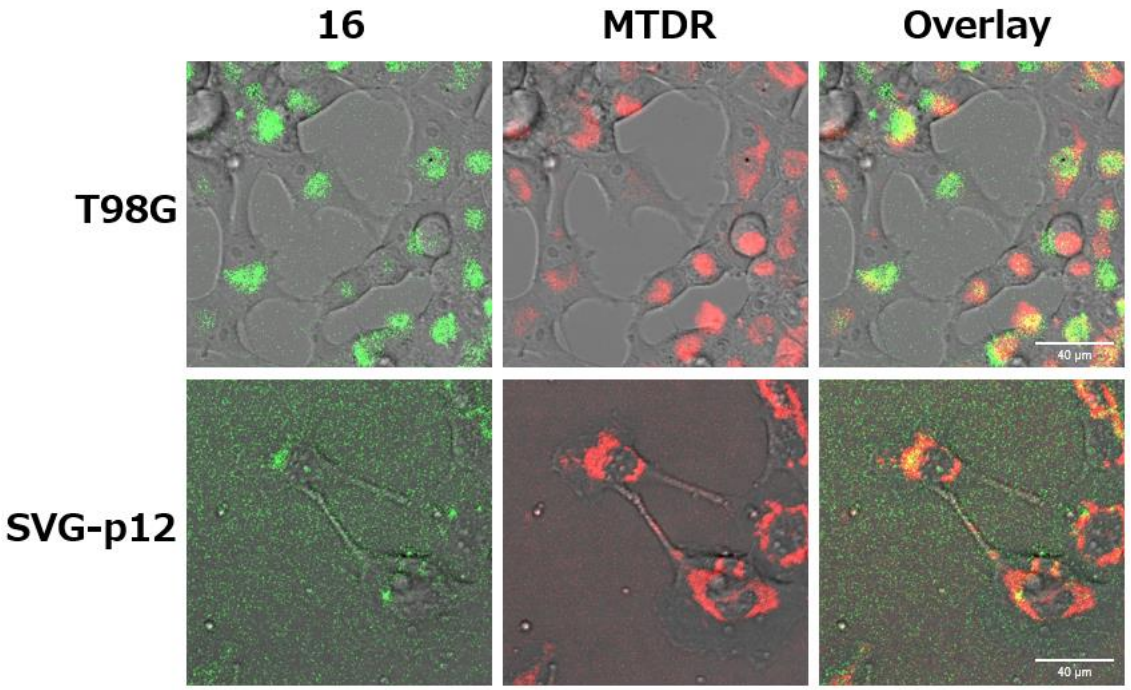

Figure 31: Fluorescence microscopy image of complex **16**, MTDR and overlay in both T98G and SVG-p12 cell lines (4 x zoom). Images were captured on a Leica SP5 II Confocal and Multiphoton microscope, and overlayed using ImageJ.

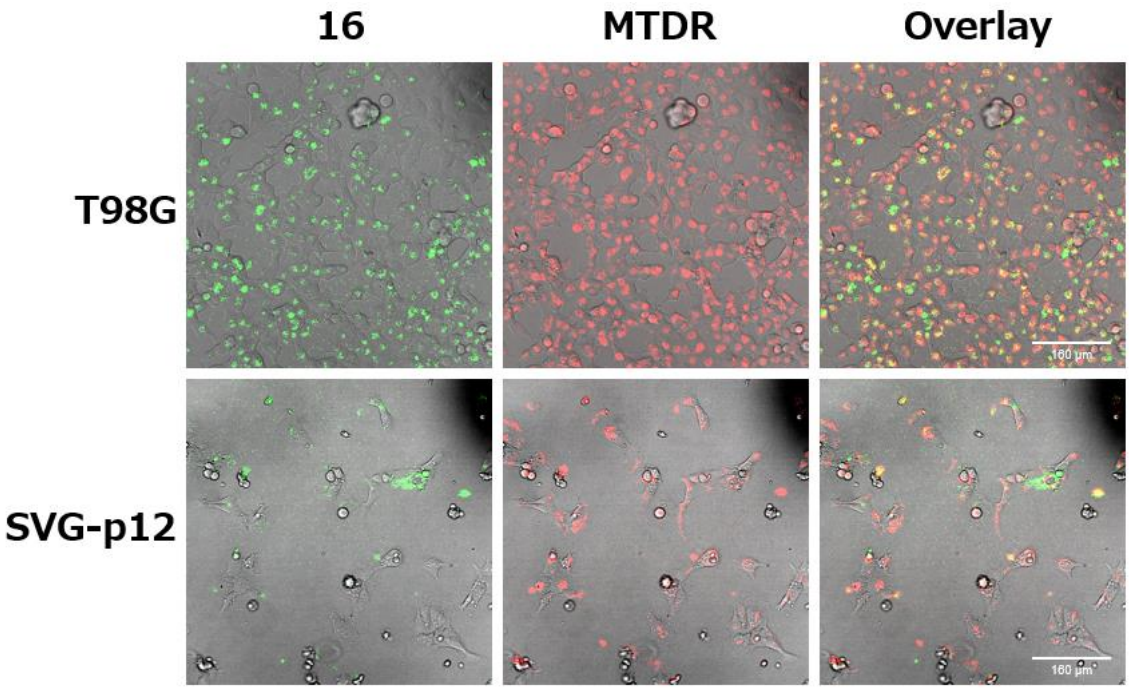

Figure 32: Fluorescence microscopy image of complex **16**, MTDR and overlay in both T98G and SVG-p12 cell lines (1 x zoom). Images were captured on a Leica SP5 II Confocal and Multiphoton microscope, and overlayed using ImageJ.

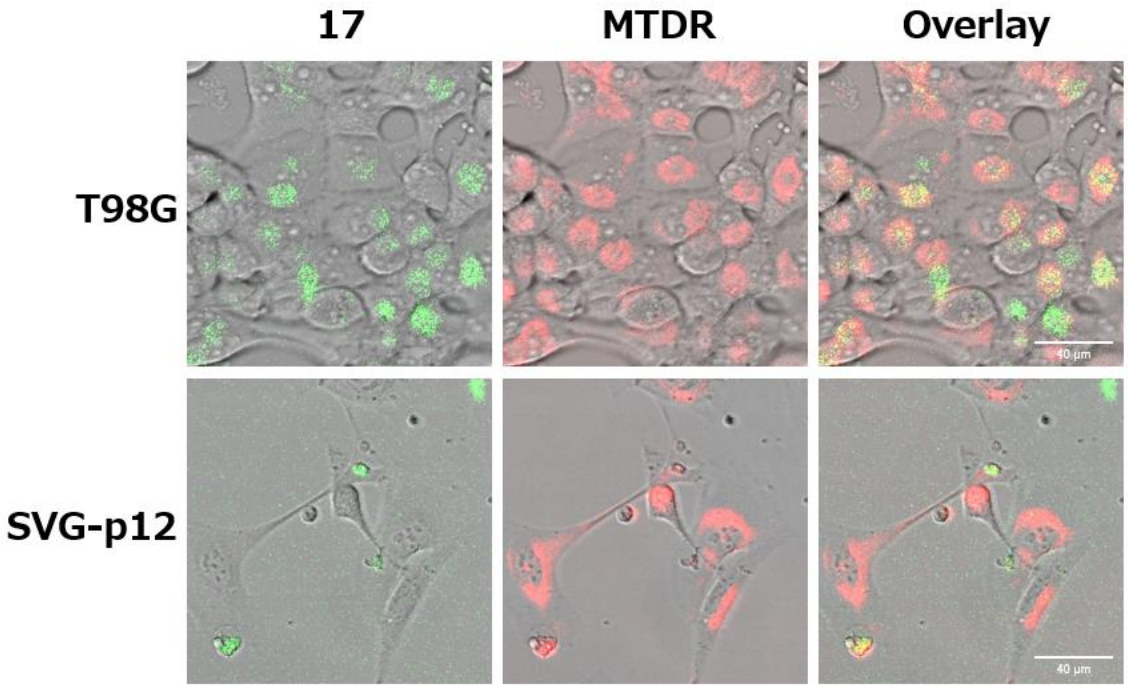

Figure 33: Fluorescent microscopy image of complex **17**, MTDR and overlay in both T98G and SVG-p12 cell lines (4 x zoom)). Images were captured on a Leica SP5 II Confocal and Multiphoton microscope, and overlayed using ImageJ.

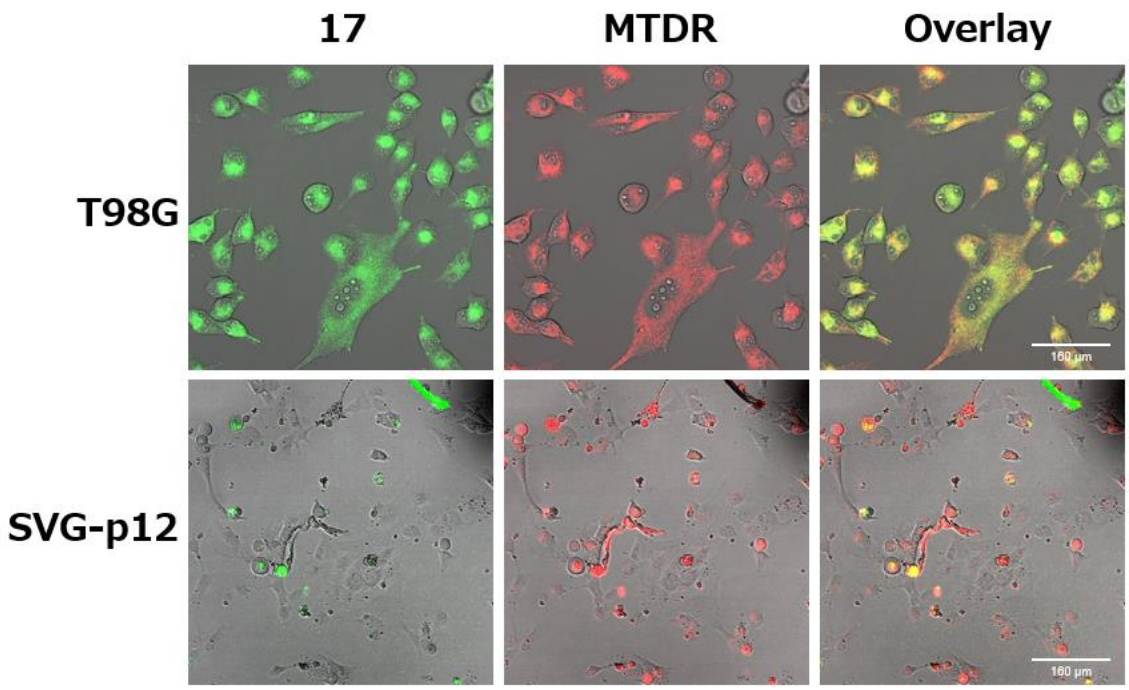

Figure 34: Fluorescent microscopy image of complex **17**, MTDR and overlay in both T98G and SVG-p12 cell lines (1 x zoom). Images were captured on a Leica SP5 II Confocal and Multiphoton microscope, and overlayed using ImageJ.

3.4 – Cell Uptake using ICP-MS

In order to supplement the microscopy data generated, cellular uptake of the lanthanoid(III) metal complexes was also measured and compared between the T98G and SVG p12 cell lines (Figure 35). The lanthanoid (terbium(III) and europium(III)) content of the dosed cells was determined by means of ICP-MS and was normalised to ng Ln / cell. Interestingly, the europium complexes (**13** and **16**) showed higher uptake than their terbium counterparts (**14** and **17**). This is possibly due to differences in membrane solvation interactions, due to electronic differences between the metal centres. Nevertheless, in accordance with the fluorescence microscopy data described in Section 3.3, complexes **13** and **14** displayed much higher cellular uptake, relative to complexes **16** and **17**, with the SVG-p12 cell line displaying less complex uptake compared to their cancer line T98G counterparts (Figure 35).

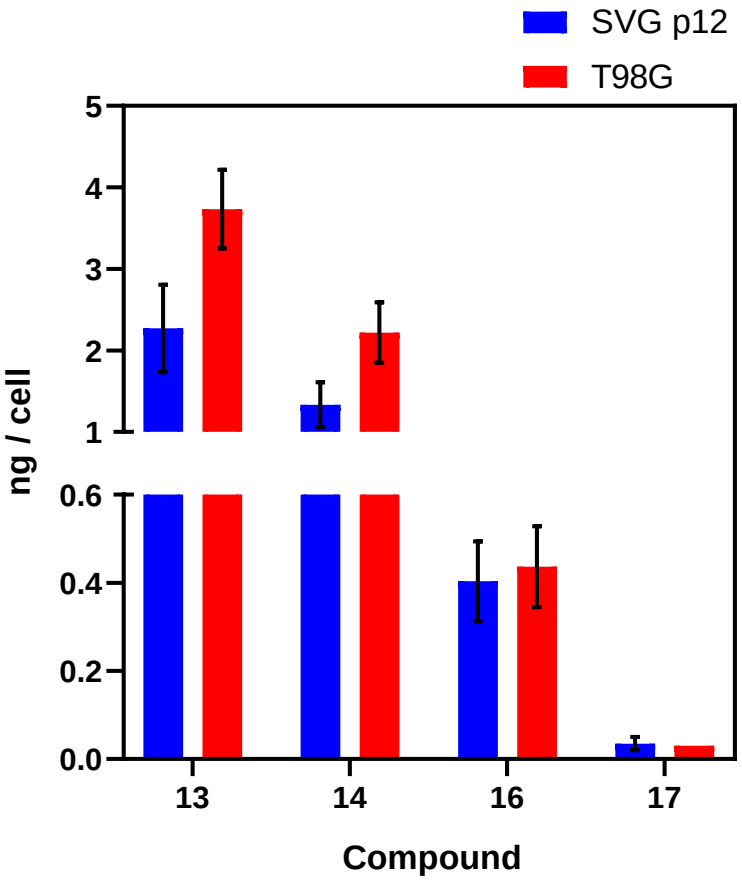

Figure 35: Average (n=3) Ln (Eu for **13**, **16**; Tb for **14**, **17**) uptake by both SVG-p12 and T98G cell lines, in ng of Ln / cell. Error bars show SEM. Values were determined by means of ICP-MS.

Chapter 4:

Conclusions and Future Work

In this project, a number of novel fluorescent lanthanoid complexes were synthesised as analogues of potential cancer theranostics. The fluorescent complexes generated in this work utilised both europium(III) and terbium(III) metal centres, coordinated by a DO3A ligand structure. A linker domain, typically consisting of a fluorescent sensitising antenna group (i.e. a xylyl, 2^{o}-amide-xylyl, butyl or naphthyl group), was used to connect the central ligand structure to a targeting moiety, which consisted of a cationic, delocalised lipophilic TPP group. Such delocalised lipophilic cation groups have previously been shown to serve as effective vectors for selectively delivering cytotoxic payloads to cancer cells.[57,58,66]

Synthetic pathways for these novel complexes were elucidated, including the spectroscopic (^{1}H NMR, ^{13}C NMR, ESI-MS, MALDI-MS) characterisation of key intermediates and target macrocyclic ligands, providing a basis for future research using these complexes. Further characterisation of the complexes was performed by means of MS, fluorescence excitation and emission properties. Additionally, *q* values were determined, being relevant in maximising fluorescent yield of the complexes. These studies identified the lanthanoid(III) complexes generated in this work as suitable candidates for fluorescent microscopy studies.

Finally, a selection of these complexes (**13**, **14**, **16**, **17**) were visualised inside cancer and normal cells using confocal microscopy. As expected, superior co-localisation was observed between these complexes and a known MTDR probe within the glioblastoma T98G cell line relative to the human glial SVG-p12 cell line. Furthermore, the complexes without a secondary amide group in the linker moiety showed superior co-localisation. Such findings were mirrored in the ICP-MS cell uptake studies, which again showed superior lanthanoid(III) complex uptake within the T98G cell line as well as high uptake for the complexes that lacked the secondary amide group in the linker moiety. These fluorescent studies serve as a precedent for a relatively time-efficient, inexpensive and effective means of analysing cellular localisation of this class of metal complexes, which can hopefully be incorporated into future studies involving analogues of these complexes.

Further studies involving microscopy could focus on identifying structure-activity relationships in terms of differences in localisation between different analogues. Such a study could be enhanced through the use of other commercially-available intracellular structural probes, in order to measure localisation of the complexes to other intracellular organelles, even beyond the mitochondria. A comparison between cancer and non-cancer cell lines in terms of differential organelle uptake could potentially reveal other intracellular targets that may be able to be exploited by these complexes in order to preferentially target cancer cells.

It would also be of interest to analyse differences in intracellular localisation due to substituting the TPP targeting moity for other delocalised phosphonium groups – or indeed, different DLC systems entirely. This could be extended to including multiple targeting entities attached to other parts of the macrocyclic ligand structure. Such complexes would need to be evaluated for their stability in solution, as alterations to the macrocyclic ligand could potentially decrease binding affinity for the lanthanoid metal centre. It would be of further interest to measure and compare cellular localisation of these complexes using entirely different targeting vectors, for both the mitochondria as well as a broader range intracellular structures. This could involve the incorporation of mitochondrial targeting peptides or folate conjugates into the molecular structure of the complexes.[117,118] Such a study could potentially lead to the revised development of superior cancer targeting groups, yielding higher selectivity and toxicity to cancer cells.

In terms of adapting fluorescent properties of the complexes developed, linker systems utilising different sensitising antenna groups, such as coumarin, could potentially be employed, with a view to developing lanthanoid complexes that produce higher fluorescent yields. This could be augmented by the use of computational molecular modelling methods, such as density functional theory (DFT) modelling, in order to identify potential linker groups that could be expected to generate high fluorescent yields. Such investigations would ultimately improve the accuracy of microscopy results and could potentially also lead to improved uptake and selectivity toward cancer cells. Further to this, quantum fluorescence yields and molecular brightness characterisation studies could be performed, and the excitation and emission spectra of the complexes further characterised.

Furthermore, it would be valuable to conduct studies in order to elucidate the mechanism of cellular uptake of these complexes. Such mechanisms could potentially be explored by measuring the effects on uptake due to temperature differences, ATP depletion, potassium depletion and blocking certain transporters such as organic cation transporters (OCTs).[119,120] Developing an understanding of uptake mechanisms would potentially be of great value in terms of maximising uptake and selectivity.

Finally, while the T98G and SVG-p12 cell systems employed within this project served as appropriate preliminary models of both normal glial and glioblastoma cells, respectively, an area of improvement would be to conduct similar studies using *in vitro* cell lines that are more representative of *in vivo* conditions. One potential avenue would be to employ QCell models from the QIMR Berghofer Medical Research Institute,[121] which produces high fidelity and well characterised primary brain cancer cell line models for academic research use. Studies using such cancer cell models would likely provide results that more accurately represent those cancers that are found *in vivo*. Furthermore, in terms of establishing the clinical utility of related metal complexes, actual *in vivo* mouse models such as the Th-MYCN transgenic neuroblastoma mouse model could be employed in order to measure a range of metrics, including cytotoxicity, localisation, cell uptake and tumour selectivity of these complexes *in vivo*.

Chapter 5:

Experimental

5.1 – Chemical Materials, Methods and Instrumentation

Precursor chemicals used throughout this project were purchased from a range of commercial manufacturers and distributors including Nowapharm China (cyclen), Sigma-Aldrich (sodium bromide and benzyl bromoacetate), Merck (Pd/C and triphenylphosphine), AJAX Finechem (TFA and sodium azide), Combi-Blocks (*tert*-butyl bromoacetate), ALFA Aesar (*α,α*'-dibromo-p-xylene) and Strem (europium oxide, gadolinium oxide, terbium oxide). Where required experimentally, H_2O was sourced using an ultrapure Milli-Q water purification system. Solvents, including DMF, acetonitrile, toluene, tetrahydrofuran (THF) and DCM, were dried using a PureSolv system. All other solvents did not require further purification and were used as purchased.

All reactions were performed under an inert atmosphere of dry nitrogen gas, using standard Schlenk protocols, unless otherwise indicated.

Analytical high performance liquid chromatography (HPLC) was performed with a Waters 2695 RP-HPLC system, equipped with a Waters Sunfire C18 analytical optimum bed density (OBD) column and a Waters 2996 photodiode array (PDA) detector. Preparative HPLC was performed with a Waters 2535 reversed-phase-HPLC quaternary gradient module, equipped with a Waters Sunfire C18 preparative OBD column and a Waters 2487 tuneable dual-wavelength absorbance detector.

All nuclear magnetic resonance (NMR) spectra were obtained using a Bruker Avance 300 NMR spectrometer with ^{1}H at 300 MHz; ^{13}C at 75 MHz; and ^{31}P at 121 MHz, all at 300 K. Chemical shift values (δ) are reported in ppm and coupling constants (J) are reported in Hz. Splitting pattern multiplicity is reported using standard abbreviations, i.e. s (singlet), d (doublet), t (triplet), q (quartet), m (multiplet).

Electrospray ionisation (ESI) mass spectra were obtained using a Bruker amazon SL mass spectrometer, with samples prepared in ethanol using a series of serial dilutions. Matrix assisted laser desorption ionisation (MALDI-TOF) mass spectra were obtained with a Bruker Autoflex speed LFR MALDI-TOF mass spectrometer

(sample preparation detailed in Chapter 5.2). Inductively-coupled plasma (ICP) mass spectroscopy was performed using a Perkin Elmer ELAN 6100 Inductively Coupled Plasma Emission Mass Spectrometer (ICP-MS).

Fluorescence spectra and fluorescence decay curves were collected using a Shimadzu RF-6000 fluorescence spectrometer. Fluorescence microscopy images were collected using a Leica SP5 II Confocal and Multiphoton microscope (details discussed in chapter 5.8).

5.2 – MALDI Matrix Preparation

In order to prepare the matrix used for MALDI-TOF MS, a stock solution of TA30 (containing 30:70 (*v:v*) MeCN:0.1% aqueous TFA) was prepared and saturated with *α*-cyano-4-hydroxycinnamic acid (4CCA), using sonication. This solution was then used to prepare samples to a concentration of approximately 0.3 mg/mL. From the solution containing the sample, 0.5 µL was spotted onto a polished steel Bruker MALDI 384 target plate and allowed to evaporate to dryness. This yielded a film on the plate, containing the sample within a 4CCA matrix.

5.3 – HPLC Methods

Stock HPLC buffer was prepared by mixing ammonium acetate (7.7 g, 100 mmol) with glacial acetic acid (3.3 mL, 57.7 mmol). The volume was made up to 1 L with water and the pH was adjusted to 4.3 through the addition of glacial acetic acid.

Analytical HPLC was performed at a flow rate of 0.2 mL/min. The mobile phase consisted of both the stock ammonium acetate solution as well as HPLC grade acetonitrile. The mobile phase was ran in a gradient from 100% ammonium acetate buffer to 100% acetonitrile (over 30 minutes for first-generation free ligands and 60 minutes for second-generation free ligands), using multi-channel detection. Samples were injected in 10 µL fractions, at a concentration of 3 mg/mL in water.

Preparative HPLC was performed at a flow rate of 7 mL/min. Again, the mobile phase consisted of both the stock ammonium acetate buffer as well as HPLC grade

acetonitrile. The mobile phase was run in a gradient from 100% ammonium acetate to 100% MeCN (over 30 minutes for first-generation free ligands and 60 minutes for second-generation free ligands), using multi-channel detection. Samples were injected in 500 µL fractions, at a concentration of 80 mg/mL in water.

5.4 – Preparation of Macrocyclic Ligands and Intermediates

5.4.1 – 1,4,7,10-tetraazacyclododecane-1,4,7-tris(tert-butyl acetate) hydrobromide (1)

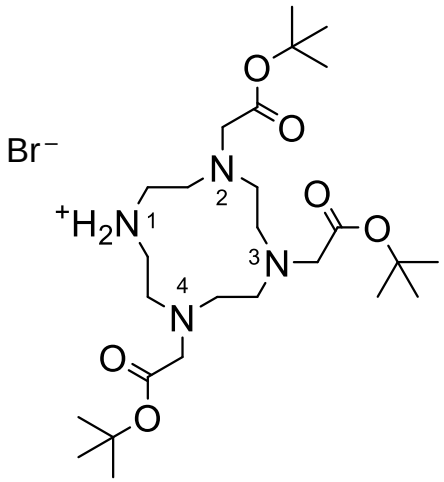

1

A solution of *tert*-butyl bromoacetate (2.8 mL, 1.61 g, 19.2 mmol) was prepared in acetonitrile (15 mL) and added dropwise over 40 minutes to a second solution of cyclen (1.00 g, 5.80 mmol) and sodium hydrogen carbonate (1.61 g, 19.2 mmol) in acetonitrile (40 mL), cooled to 0 ^{o}C in an ice bath. The reaction mixture was allowed to warm to room temperature and was then stirred for a further 48 hours. The mixture was filtered and the filtrate was reduced *in vacuo*. The crude product obtained was then recrystalised from toluene, yielding a colourless crystalline powder (1.16 g, 34%). ESI-MS for $[M + H]^+$: calculated *m/z* 515.38, observed *m/z* 515.41. ^{1}H NMR (300 MHz, $CDCl_3$) δ 10.03 (s, 2H, N$\underline{H}_2$), 3.39 (s, 4H, N2+N4 NC$\underline{H}_2$CO), 3.32 (s, 2H, N3 NC$\underline{H}_2$CO), 3.12 (m, 4H, $NH_2C\underline{H}_2$), 2.93 (m, 8H, N2+N4 $NH_2C\underline{H}_2C\underline{H}_2N$), 2.90 (m, 4H, N1 $NH_2CH_2C\underline{H}_2N$), 1.48 (s, 27H, C$\underline{H}_3$). ^{13}C NMR (75 MHz, $CDCCl_3$) δ 170.54 (s, N2+N4 $\underline{C}O$), 169.65 (s, N3 $\underline{C}O$), 81.87 (s, N2+N4 $\underline{C}(CH_3)_3$), 81.71 (s, N3 $\underline{C}(CH_3)_3$), 58.23 (s, N$\underline{C}H_2CO$), 51.38 (s, N2+N4 N$\underline{C}H_2\underline{C}H_2N$), 49.25 (s, N2+N4 N$\underline{C}H_2CH_2NH_2$), 47.51 (s, $\underline{C}H_2NH_2$), 28.24 (s, $\underline{C}H_3$).

5.4.2 – 1,4,7,10-tetraazacyclododecane-1,4,7-tris(tert-butyl acetate)-10-benzyl acetate (2)

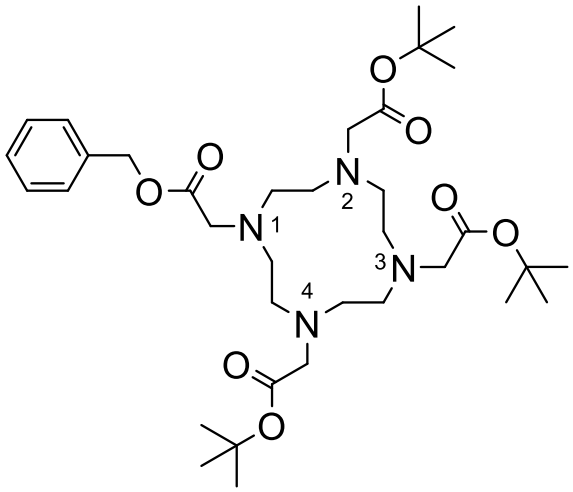

2

A solution of benzyl bromoacetate (174 mg, 0.76 mmol) was prepared in acetonitrile (10 mL). This was then added dropwise to solution of **1** (465 mg, 0.78 mmol) and potassium carbonate (216 mg, 1.56 mmol) in acetonitrile (50 mL). The reaction mixture was heated under reflux for 12 hours and then filtered, washing the residue with acetonitrile. The filtrate was reduced *in vacuo* and re-dissolved in DCM (150 mL), which was washed with water (2 x 50 mL), brine (2 x 50 mL) and water again (50 mL). The organic layer was then collected and dried over magnesium sulphate, which was subsequently filtered off. The filtrate was then reduced *in vacuo*, yielding the product as a pale-orange crystalline powder (0.50 g, 98%). ESI-MS for $[M + Na]^+$: calculated *m/z* 685.42, observed m/z 685.43. ^{1}H NMR (300 MHz, $CDCl_3$) δ 7.35 (m, 5H, Ar), 5.14 (s, 2H, PhC$\underline{H}_2$O), 3.90-1.78 (br m, 24H, NC$\underline{H}_2$), 1.44 (s, 27H, C$\underline{H}_3$). ^{13}C NMR (75 MHz, $CDCCl_3$) δ 173.2 (s, N1 NC$H_2\underline{C}$O), 172.8 (s, N2+N4 NC$H_2\underline{C}$O), 135.4 (s, Ph-i-$\underline{C}$), 128.7 (s, Ph-m-$\underline{C}$H), 128.3 (s, Ph-p-$\underline{C}$H), 128.2 (s, Ph-o-$\underline{C}$H), 81.8 (s, $\underline{C}(CH_3)_3$), 71.9 (s, $\underline{C}H_2$Ph), 55.8 (s, N2+N4 N$\underline{C}H_2$CO), 55.7 (s, N3 N$\underline{C}H_2$CO), 55.5 (s, N1 N$\underline{C}H_2$CO), 50.9 (m, N$\underline{C}H_2\underline{C}H_2$N), 28.1 (s, $\underline{C}H_3$).

5.4.3 – 1,4,7,10-tetraazacyclododecane-1,4,7-tris(tert-butyl acetate)-10-acetic acid (3)

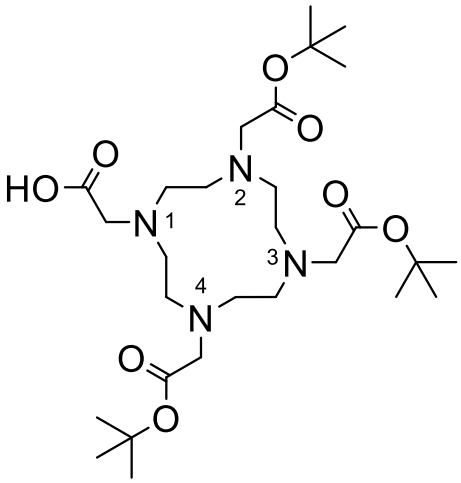

3

A solution of **2** (0.470 g, 0.711 mmol) in methanol (10 mL) was prepared and added to methanol (20 mL) containing one small spatula of Pd/C catalyst. The mixture was placed under a hydrogen atmosphere (1 atm), first purging the flask by bubbling hydrogen gas through the mixture 3 times. The mixture was then stirred for 6 hours at room temperature, after which it was filtered through Celite, washing with methanol (30 mL). The filtrate was reduced *in vacuo*, yielding an amber oil (0.378 g, 93%). ESI-MS for $[M + Na]^+$: calculated *m/z* 595.37, observed *m/z* 595.37. ^{1}H NMR (300 MHz, $CDCl_3$) δ 3.32–2.09 (br m, 24H, C$\underline{H}_2$) 1.42 (m, 27H, C$\underline{H}_3$).^{13}C NMR (75 MHz, $CDCCl_3$) δ 174.6 (s, $\underline{C}$OOH), 173.6 (s, NCH$_2\underline{C}$OO), 89.3 (s, C($\underline{C}$H$_3$)$_3$), 55.8 (m, N$\underline{C}$H$_2$CO), 52.1 (m, N$\underline{C}$H$_2\underline{C}$H$_2$N), 28.1 (s, $\underline{C}$H$_3$).

5.5 – Preparation of Triphenylphosphonium Moieties

5.5.1 – (4-(bromomethyl)benzyl)triphenylphosphonium bromide (4)

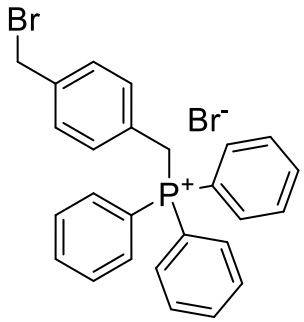

4

Triphenylphosphine (0.66 g, 2.50 mmol) was added to a solution of *α,α'*-dibromo-p-xylene (0.66 g, 2.50 mmol) in toluene (15 mL). The reaction mixture was stirred and heated under reflux at 60 ^{o}C for 24 hours. The precipitate was then collected by filtration, washed with toluene (5 mL) and diethyl ether (2 x 10 mL), and dried under reduced pressure, yielding the product as a colourless powder (1.14 g, 86%). ESI-MS for $[M]^+$: calculated *m/z* 445.07, observed *m/z* 445.07. ^{1}H NMR (300 MHz, $CDCl_3$) δ 7.76-7.64 (m, 9H, o-PhP$^+$, p-PhP$^+$), 7.65-7.55 (m, 6H, m-PhP$^+$), 7.14 (m, 4H, Xy), 5.48 (d, 2H, C$\underline{H}_2$P$^+$, $^{2}J_{HP}$ = 14.6 Hz), 4.40 (s, 2H, C$\underline{H}_2$Br). ^{13}C NMR (75 MHz, $CDCCl_3$) δ 138.3 (d, p-Xy, $^{5}J_{CP}$ = 4.0 Hz), 135.1–134.1 (m, p-Ph), 131.8 (m, o-Xy, $^{3}J_{CP}$ = 5.2 Hz), 130.5–129.6 (m, o-Ph), 129.4 (d, m-Xy, $^{4}J_{CP}$ = 2.5 Hz), 127.7 (d, i-Xy, $^{2}J_{CP}$ = 8.8 Hz), 117.7 (d, i-PhP$^+$, $^{1}J_{CP}$ = 86.1 Hz), 32.8 (s, $\underline{C}H_2$Br), 30.5 (d, CH_2P^+, $^{1}J_{CP}$ = 46.7 Hz). ^{31}P NMR (121 MHz, $CDCl_3$) δ 23.4 (s).

5.5.2 – (4-(azidomethyl)benzyl)triphenylphosphonium bromide (5)

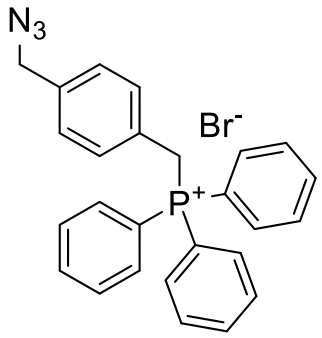

5

A solution of **4** (0.526 g, 1.00 mmol) in DMF (15 mL) was prepared and added to a stirred solution of sodium azide (0.195 g, 3.00 mmol) in DMF (40 mL). The reaction mixture was stirred at room temperature for 72 hours, after which the DMF was removed under a stream of nitrogen. The residue was suspended in chloroform (40 mL) and filtered to remove the excess inorganic salts, washing the precipitate with chloroform (50 mL). The filtrate was reduced *in vacuo*, and the resulting solid washed with ethyl acetate (50 mL) and acetone (50 mL), yielding the product as a fine colourless crystalline powder (0.438 g, 90%). ESI-MS for $[M]^+$: calculated *m/z* 408.16, observed *m/z* 408.15. ^{1}H NMR (300 MHz, $CDCl_3$) δ 7.79– 7.68 (m, 9H, o-PhP^+, p-PhP^+), 7.65-7.52 (m, 6H, m-PhP^+), 7.16 (dd, 2H, o-xy, $^3J_{HH}$ = 6.1 Hz, $^4J_{HP}$ = 2.2 Hz), 7.07 (d, 2H, m-xy H, $^3J_{HH}$ = 7.7 Hz), 5.49 (d, 2H, CH_2P^+, $^2J_{HP}$ = 14.4 Hz), 4.24 (s, 2H, CH_2N_3). ^{13}C NMR (75 MHz, $CDCCl_3$) δ 135.2 (d, p-Xy, $^5J_{CP}$ = 3.9 Hz), 134.9 (s, p-PhP^+), 134.5 (s, m-PhP^+), 132.1 (d, o-Xy C, $^3J_{CP}$ = 5.8 Hz), 130.3 (m, o-PhP^+), 128.7 (s, m-Xy), 127.6 (d, i-Xy, $^2J_{CP}$ = 9.7 Hz), 117.2 (d, i-PhP^+, $^1J_{CP}$ = 85.2 Hz), 54.2 (s, $\underline{C}H_2N_3$), 30.4 (d, $\underline{C}H_2P^+$, $^1J_{CP}$ = 46.6 Hz). ^{31}P NMR (121 MHz, $CDCl_3$) δ 23.5 (s).

5.5.3 – (4-(Aminomethyl)benzyl)triphenylphosphonium bromide (6)

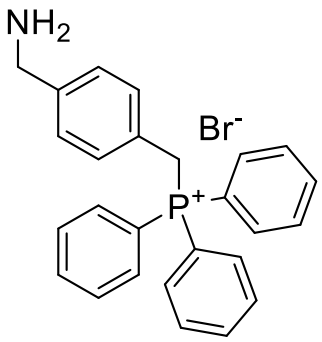

6

A solution of **5** (0.3872 g, 0.7928 mmol) in methanol (10 mL) was prepared and added methanol (10 mL) containing one small spatula of Pd/C catalyst. The mixture was placed under a hydrogen atmosphere (1 atm), first purging the flask by bubbling hydrogen gas through the mixture 3 times. The mixture was then stirred for 6 hours at room temperature, after which it was filtered through Celite, washing with methanol (30 mL). The filtrate was reduced *in vacuo*, and the crude product redissolved in water (50 mL). The aqueous phase was washed with DCM (3 x 20 mL), after which the aqueous phase was collected and reduced under a stream of nitrogen. This yielded the product as a colourless crystalline powder (0.297 g, 81%). ESI-MS for $[M]^+$: calculated *m/z* 382.17, observed *m/z* 382.19. ^{1}H NMR (300 MHz, D_2O) δ 7.75–7.54 (m, 15H, PhP^+), 7.29–6.95 (m, 4H, Xy), 5.10 (d, 2H, $C\underline{H}_2P^+$, $^2J_{HP}$ = 14.2 Hz), 4.07 (s, 2H, $C\underline{H}_2NH_2$), 2.64 (s, 2H, $N\underline{H}_2$). ^{13}C NMR (75 MHz, D_2O) δ 135.2 (s, p-Xy), 134.2 (m, p-PhP^+), 131.6 (d, o-Xy, $^3J_{CP}$ = 5.1 Hz), 129.9 (m, o-PhP^+), 127.3 (s, i-Xy), 124.3 (s, m-Xy), 117.1 (d, i-PhP^+, $^1J_{CP}$ = 85.5 Hz), 42.8 (s, $\underline{C}H_2NH_2$), 31.1 (d, $\underline{C}H_2P^+$, $^1J_{CP}$ = 52.6 Hz). ^{31}P NMR (121 MHz, D_2O) 22.4 (s, $\underline{P}^+$).

5.5.4 – 2,6-bis(bromomethyl)naphthalene (7)

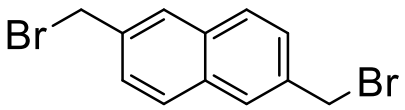

7

To a solution of 2,6-dimethylnaphthalene (0.401 g, 2.57 mmol) in DCM was added *N*-bromosuccinimide (0.915 mg, 5.14 mmol) and azobisisobutyronitrile (34.48 mg, 0.21 mmol). The mixture was heated under reflux at 38 ^{o}C for 48 hours, after which it was cooled to room temperature, dried over anhydrous sodium sulphate and filtered off. The filtrate was mixed with cyclohexane (100 mL) and filtered again. The solvent was then reduced, yielding the product as a colourless crystalline powder (0.572 g, 71%). mp 187 ^{o}C (from cyclohexane). ^{1}H NMR (300 MHz, $CDCl_3$) δ 7.74–7.38 (m, 6H, Nap), 4.68 (s, 2H, C$\underline{H}_2$Br). ^{13}C NMR (75 MHz, $CDCl_3$) δ 134.5-126.6 (m, Nap), 34.5 (s, 4H, $\underline{C}H_2$Br).

5.5.5 – ((6-(bromomethyl)naphthalen-2-yl)methyl)triphenylphosphonium bromide (8)

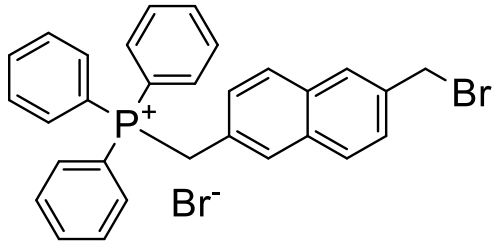

8

Triphenylphosphine (0.477 g, 1.82 mmol) was added to a solution of **7** (0.572 g, 1.82 mmol) in toluene (20 mL). The reaction mixture was stirred and heated under reflux at 60 ^{o}C for 72 hours. The precipitate was then collected, washing with toluene (5 mL) and diethyl ether (2 x 10 mL) and dried under reduced pressure, yielding the product as a colourless powder (0.259 g, 25%). ESI-MS for $[M]^+$: calculated *m/z* 497.09, observed *m/z* 497.14. ^{1}H NMR (300 MHz, $CDCl_3$) δ 7.76–7.67 (m, 6H, Nap), 7.62–7.54 (m, 15H, PhP^+), 5.65 (d, 2H, $C\underline{H}_2P^+$, $^{2}J_{HP}$ = 14.0 Hz). 4.61 (s, 2H, $C\underline{H}_2Br$). ^{13}C NMR (75 MHz, $CDCl_3$) δ 135.5-134.7 (m, o-PhP^+, p-PhP^+), 134.3 (m, m-PhP^+), 130.6-129.8 (m, Nap), 117.8 (d, i-PhP^+, $^{1}J_{CP}$ = 86.4 Hz), 33.8 (s, 2H, $\underline{C}H_2Br$), 30.6 (d, CH_2P^+, $^{1}J_{CP}$ = 46.7 Hz). ^{31}P NMR (121 MHz, $CDCl_3$) δ 23.2 (s).

5.6 – Coupling Reactions

5.6.1 – Triphenyl(4-((4,7,10-tris(carboxymethyl)-1,4,7,10-tetraazacyclododecan-1-yl)methyl)benzyl)phosphonium trifluoroacetate (9)

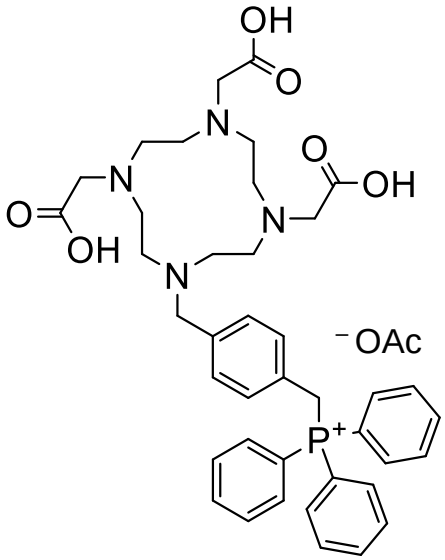

9

Sodium carbonate (0.0731 g, 0.680 mmol) was added to a solution of **1** (0.10 g, 0.19 mmol) and **4** (0.099 g, 0.17 mmol) in acetonitrile (10 mL). The reaction mixture was heated under reflux at 80 ^{o}C for 36 hours. The mixture was then filtered and reduced *in vacuo*, yielding the *tert*-butyl protected ligand as a colourless powder. This product was subsequently dissolved in trifluoroacetic acid (TFA):DCM 1:1 (6 mL) and stirred at room temperature for 18 hours. The volatiles were then reduced under a stream of nitrogen and the crude residue dissolved in water (50 mL) washing with chloroform (3 x 25 mL). The aqueous layer was collected and reduced under a stream of nitrogen, yielding a colourless oil, which was purified using RP-HPLC freeze dried. This yielded the product as a colourless powder (0.103 g, 79%). MALDI-TOF MS for $[M]^+$: calculated *m/z* 711.33, observed *m/z* 711.33. ^{1}H NMR (D_2O, 300 MHz) δ 7.85 (m, 3H, p-PhP$^+$), 7.65 (m, 12H, o-PhP$^+$, m-PhP$^+$), 7.33 (d, 2H, o-Xy, $^{3}J_{HH}$ = 7.6 Hz), 7.00 (d, 2H, m-Xy, $^{3}J_{HH}$ = 8.2 Hz), 4.73 (s, 2H, C$\underline{H}_2$P$^+$), 3.82 (s, 2H, Xy-C$\underline{H}_2$N), 3.60–2.71 (br m, 22H, NC$\underline{H}_2$). ^{13}C NMR (75 MHz, D_2O) δ 171.0 (s, CO), 135.1 (s, p-Xy), 134.2 (s, p-PhP$^+$), 134.1 (s, m-PhP$^+$), 131.8 (m, o-Xy), 131.6 (s, o-PhP$^+$), 130.0 (s,

m-Xy), 129.9 (m, i-Xy), 117.1 (d, i-PhP$^+$, $^1J_{CP}$ = 86.7 Hz), 56.4 (s, $\underline{C}H_2CO$), 56.1 (m, Xy-N$\underline{C}H_2$), 50.2 (s, N$\underline{C}H_2\underline{C}H_2$N), 29.7 (d, CH_2P^+, $^1J_{CP}$ = 49.1 Hz). ^{31}P NMR (121 MHz, D_2O) δ 22.1 (s).

5.6.2 – Triphenyl(4-((2-(4,7,10-tris(carboxymethyl)-1,4,7,10-tetraazacyclododecan-1-yl)acetamido)methyl)benzyl)phosphonium trifluoroacetate (10)

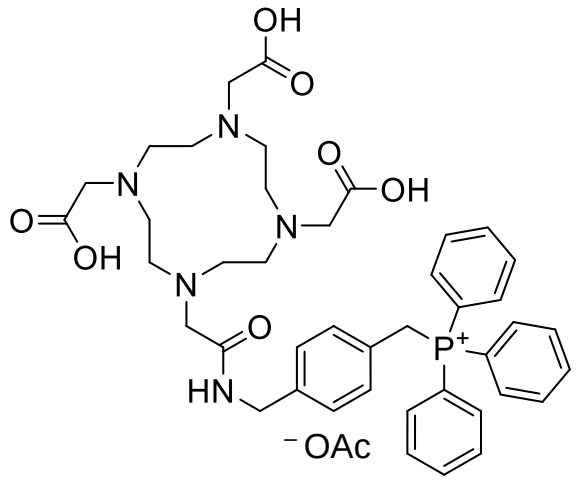

10

A solution of **1** (0.337 g, 0.66 mmol), HATU (300 g, 0.79 mmol) and NMM (0.281 g, 1.39 mmol) in dimethylformamide (20 mL) was prepared. A second solution of **6** (0.301 g, 0.65 mmol) in DMF (15 mL) was prepared and added dropwise. The reaction mixture was then stirred at room temperature for 24 hours before being reduced *in vacuo* to yield an amber oil. This product was subsequently dissolved in TFA:DCM 1:1 (10 mL) and stirred at room temperature for 16 hours. The volatiles were then reduced under a stream of nitrogen and the crude residue dissolved in water (50 mL) washing with chloroform (3 x 25 mL). The aqueous layer was collected and reduced under a stream of nitrogen, yielding a colourless oil, which was purified using RP-HPLC freeze dried. This yielded the product as a colourless powder (0.182 g, 33%). MALDI-TOF MS for $[M]^+$: calculated *m/z* 761.35, observed *m/z* 761.56. ^{1}H NMR (300 MHz, $CDCl_3$) δ 7.94−7.75 (m, 3H, p-PhP$^+$), 7.74−7.47 (m, 12H, o-PhP$^+$, m-PhP$^+$), 7.08 (s, 2H, o-Xy), 6.95 (s, 2H, m-Xy), 4.26 (s, 2H, C$\underline{H}_2$P$^+$), 4.00-1.71 (m, 26H, NC$\underline{H}_2$). ^{13}C NMR (75 MHz, $CDCl_3$) δ 172.0 (s, $\underline{C}$O), 135.9 (s, p-Xy), 135.7 (s, p-PhP$^+$), 134.6 (m, m-PhP$^+$), 132.9 (m, o-Xy), 131.0 (s, Ar C), 128.8 (m, o-PhP$^+$), 127.8 (s, m-Xy), 127.5 (s, i-Xy), 123.1 (m, i-PhP$^+$), 56.8 (m, N$\underline{C}$H$_2$O), 51.3 (m, N$\underline{C}$H$_2\underline{C}$H$_2$N), 46.8 (s, $\underline{C}$H$_2$NH), 33.7 (s, $\underline{C}$H$_2$P$^+$). ^{31}P NMR (121 MHz, $CDCl_3$) δ 22.4 (s).

5.6.3 – Triphenyl((6-((4,7,10-tris(carboxymethyl)-1,4,7,10-tetraazacyclododecan-1-yl)methyl)naphthalen-2-yl)methyl)phosphonium trifluoroacetate (11)

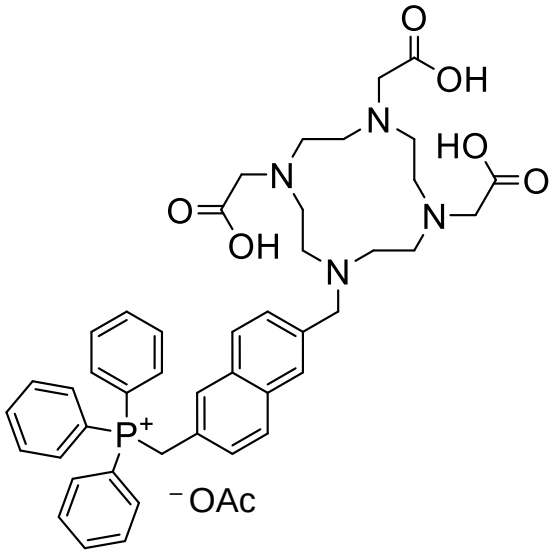

11

Sodium carbonate (0.191 g, 1.80 mmol) was added to a solution of **1** (0.268 g, 0.45 mmol) and **8** (0.259 g, 0.45 mmol) in acetonitrile (20 mL). The reaction mixture was heated under reflux at 80 ^{o}C for 36 hours. The mixture was then filtered and reduced *in vacuo*, yielding the *tert*-butyl protected ligand as a white powder. This product was subsequently dissolved in TFA:DCM 1:1 (6 mL) and stirred at room temperature for 18 hours. The volatiles were then reduced under a stream of nitrogen and the crude residue dissolved in water (50 mL) washing with chloroform (3 x 25 mL). The aqueous layer was collected and reduced under a stream of nitrogen, yielding a colourless oil, which was purified using RP-HPLC and freeze dried. This yielded the product as a colourless powder (0.101 g, 29%). ESI-MS for $[M+^{t}Bu_3]^+$: calculated *m/z* 929.53, observed *m/z* 929.53. MALDI-TOF MS for $[M]^+$: calculated *m/z* 761.35, observed *m/z* 761.56. ^{1}H NMR (300 MHz, $CDCl_3$) δ 7.94−7.72 (m, 6H, Nap), 7.68−6.82 (m, 15H, PhP^+), 4.30 (s, 2H, $C\underline{H}_2P^+$), 3.70-1.71 (m, 24H, $C\underline{H}_2N$). ^{31}P NMR (121 MHz, $CDCl_3$) δ 23.6 (s).

5.7 – Complex Formation

5.7.1 – 2,2',2''-(10-(4-((triphenylphosphonio)methyl)benzyl)-1,4,7,10-tetraazacyclododecane-1,4,7-triyl)triacetatogadolinium(III) trifluoroacetate (12)

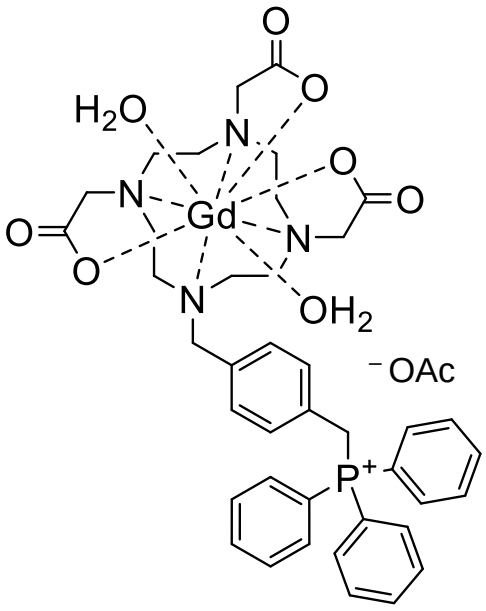

12

Gadolinium oxide (52 mg, 0.002685 mmol) and **9** (8.1 mg, 0.0105 mmol) were dissolved in water (10 mL) and stirred at room temperature for 36 hours. The mixture was then centrifuged, and the supernatant passed through a 0.2 µm PTFE syringe filter. The filtrate was freeze-dried, yielding the product as a colourless powder (5.3 mg, 85%). MALDI-TOF MS for $[M]^+$: calculated *m/z* 866.23, observed *m/z* 866.21.

5.7.2 – 2,2',2''-(10-(4-((triphenylphosphonio)methyl)benzyl)-1,4,7,10-tetra azacyclododecane-1,4,7-triyl)triacetatoeuropium(III) trifluoroacetate (13)

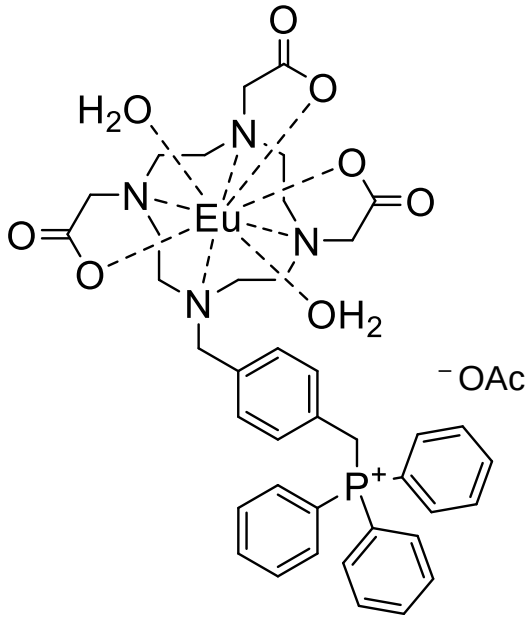

13

Europium oxide (36 mg, 0.10 mmol) and **9** (9.5 mg, 0.012 mmol) were dissolved in water (10 mL) and stirred at 80 ^{o}C for 36 hours. The mixture was then centrifuged, and the supernatant passed through a 0.2 µm PTFE syringe filter. The filtrate was freeze-dried, yielding the product as a colourless powder (4.3 mg, 39%). MALDI-TOF MS for $[M]^{+}$: calculated *m/z* 861.23, observed *m/z* 861.15.

5.7.3 – 2,2',2''-(10-(4-((triphenylphosphonio)methyl)benzyl)-1,4,7,10-tetra azacyclododecane-1,4,7-triyl)triacetatoterbium(III) trifluoroacetate (14)

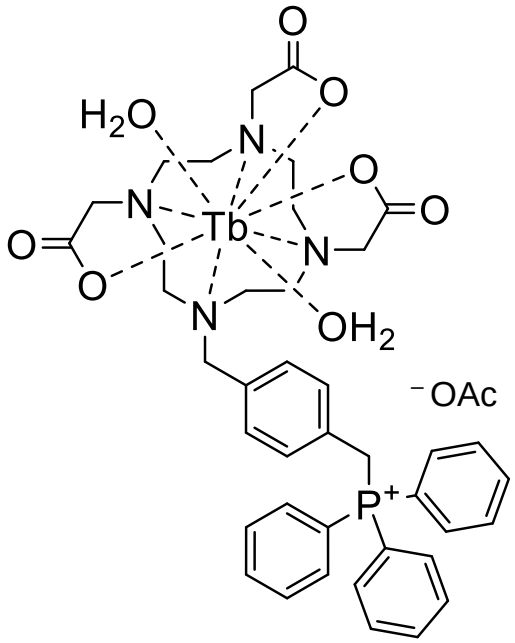

14

Terbium oxide (3 mg, 0.00402 mmol) and **9** (6 mg, 0.0078 mmol) were dissolved in water (10 mL) and stirred at room temperature for 36 hours. The mixture was then centrifuged, and the supernatant passed through a 0.2 µm PTFE syringe filter. The filtrate was freeze-dried, yielding the product as a colourless powder (3.9 mg, 54%). MALDI-TOF MS for $[M]^+$: calculated *m/z* 867.23, observed *m/z* 867.22.

5.7.4 – 2,2',2''-(10-(2-oxo-2-((4-((triphenylphosphonio)methyl)benzyl) amino)ethyl)- 1,4,7,10-tetraazacyclododecane-1,4,7-triyl) triacetatogadolinium(III) trifluoroacetate (15)

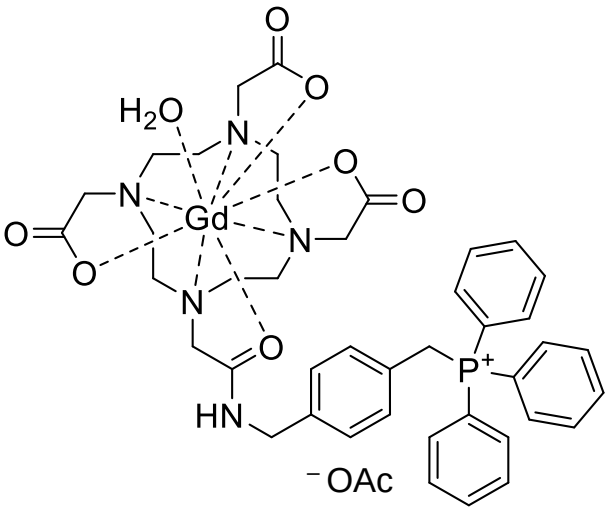

15

Gadolinium oxide (3.63 mg, 0.01 mmol) and **10** (10 mg, 0.012 mmol) were dissolved in water (10 mL) and stirred at room temperature for 24 hours. The mixture was then centrifuged, and the supernatant passed through a 0.2 µm PTFE syringe filter. The filtrate was freeze-dried, yielding the product as a colourless powder (8.4 mg, 75%). MALDI-TOF MS for $[M]^+$: calculated *m/z* 922.25, observed *m/z* 923.01.

5.7.5 – 2,2',2''-(10-(2-oxo-2-((4-((triphenylphosphonio)methyl)benzyl) amino)ethyl)- 1,4,7,10-tetraazacyclododecane-1,4,7-triyl) triacetatoeuropium(III) trifluoroacetate (16)

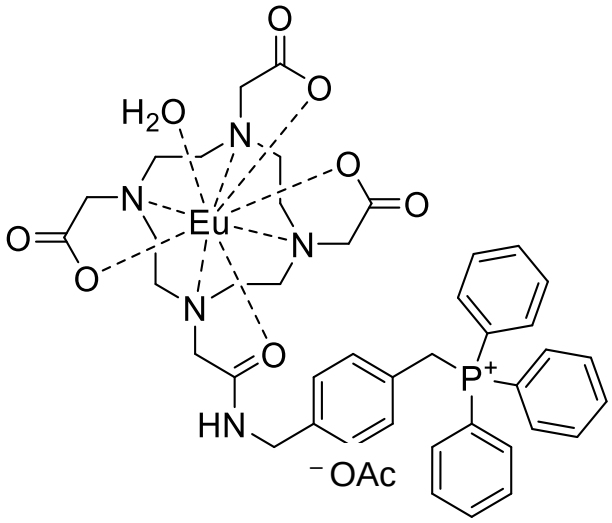

16

Europium oxide (10.56 mg, 0.03 mmol) and **10** (35 mg, 0.0423 mmol) were dissolved in water (10 mL) and stirred at room temperature for 36 hours. The mixture was then centrifuged, and the supernatant passed through a 0.2 µm PTFE syringe filter. The filtrate was freeze-dried, yielding the product as a colourless powder (37.5 mg, 94%). MALDI-TOF MS for $[M]^+$: calculated *m/z* 918.25, observed *m/z* 918.25.

5.7.6 – 2,2',2''-(10-(2-oxo-2-((4-((triphenylphosphonio)methyl)benzyl) amino)ethyl)- 1,4,7,10-tetraazacyclododecane-1,4,7-triyl) triacetatoterbium(III) trifluoroacetate (17)

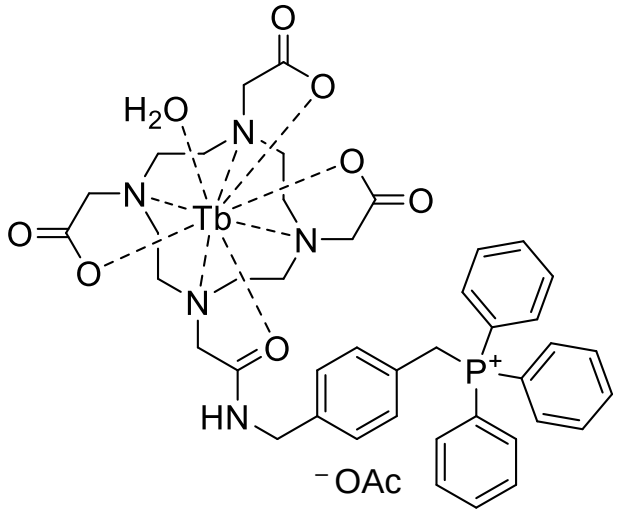

17

Terbium oxide (22.43 mg, 0.03 mmol) and **10** (35 mg, 0.0423 mmol) were dissolved in water (10 mL) and stirred at room temperature for 36 hours. The mixture was then centrifuged, and the supernatant passed through a 0.2 µm PTFE syringe filter. The filtrate was freeze-dried, yielding the product as a colourless powder (32.9 mg, 83%). MALDI-TOF MS for $[M]^+$: calculated *m/z* 924.25, observed *m/z* 924.26.

5.7.7 – 2,2',2''-(10-(4-(triphenylphosphonio)butyl)-1,4,7,10-tetraazacyclododecane-1,4,7-triyl)triacetatoeuropium(III) trifluoroacetate (18)

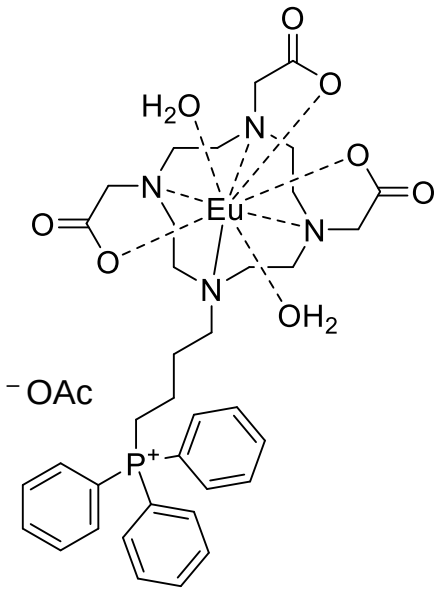

18

Europium oxide (2.2 mg, 0.0063 mmol) and triphenyl(4-(4,7,10-tris(carboxymethyl)-1,4,7,10-tetraazacyclododecan-1-yl)butyl)phosphonium acetate (3 mg, 0.0042 mmol) were dissolved in water (10 mL) and stirred at 80 ^{o}C for 72 hours. The mixture was then centrifuged, and the supernatant passed through a 0.2 µm PTFE syringe filter. The filtrate was freeze-dried, yielding the product as a colourless powder (2.1 mg, 61%). MALDI-TOF MS for $[M]^{+}$: calculated *m/z* 813.23, observed *m/z* 813.13.

5.7.8 – 2,2',2''-(10-(4-(triphenylphosphonio)butyl)-1,4,7,10-tetraazacyclododecane-1,4,7-triyl)triacetatoterbium(III) trifluoroacetate (19)

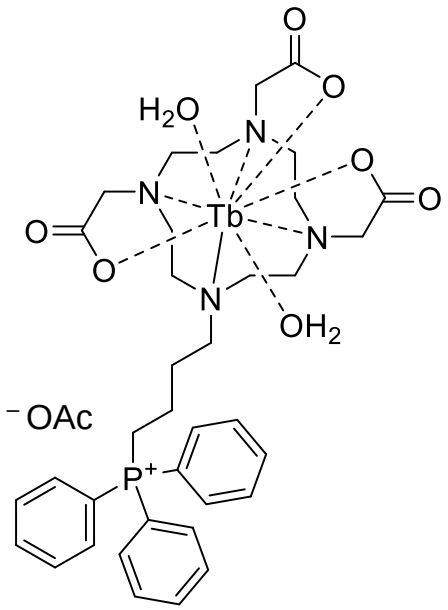

19

Terbium oxide (7.48 mg, 0.0100 mmol) and triphenyl(4-(4,7,10-tris(carboxymethyl)-1,4,7,10-tetraazacyclododecan-1-yl)butyl)phosphonium acetate (6.5 mg, 0.0091 mmol) were dissolved in water (10 mL) and stirred at 80 ^{o}C for 72 hours. The mixture was then centrifuged, and the supernatant passed through a 0.2 µm PTFE syringe filter. The filtrate was freeze-dried, yielding the product as a colourless powder (6.5 mg, 85%). MALDI-TOF MS for $[M]^{+}$: calculated *m/z* 819.23, observed *m/z* 819.21.

5.7.9 – 2,2',2''-(10-((6-((triphenylphosphonio)methyl)naphthalen-2-yl)methyl)-1,4,7,10-tetraazacyclododecane-1,4,7-triyl)triacetatoterbium(III) trifluoroacetate (20)

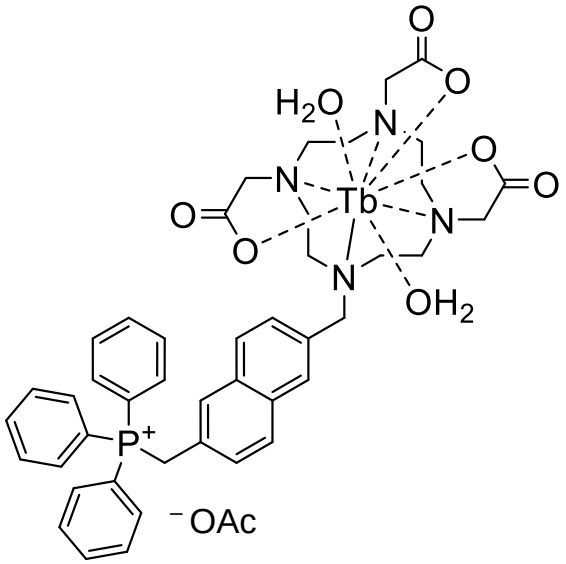

20

Terbium oxide (16 mg, 0.022 mmol) and **11** (50 mg, 0.0649 mmol) were dissolved in water (10 mL) and stirred at 80 ^{o}C for 36 hours. The mixture was then centrifuged, and the supernatant passed through a 0.2 µm PTFE syringe filter. The filtrate was freeze-dried, yielding the product as a colourless powder (41 mg, 68%). MALDI-MS for $[M]^{+}$: calculated *m/z* 917.25, observed *m/z* 917.18.

5.8 – Biological and Confocal Fluorescence Microscopy Methods

Both human glioblastoma (T98G) and human foetal glial (SVG-p12) cell lines were purchased from ATCC. Advanced DMEM (1X) Reduced Serum Medium was purchased from Gibco. Plastic and glassware was purchased from Costar and glass bottom cell culture dishes for microscopy from Mattek. FBS, PBS, TrypLE, L-glutamine and antibiotic solutions were all purchased from ThermoFisher scientific.

The T98G and SVG-p12 were both cultured in a Category 3 Cell Culture lab in accordance with standard cell culturing techniques. The two cell lines were cultured as monolayers, using Advanced DMEM (1X) Reduced Serum Medium, supplemented with penicillin (100 u/mL), L-glutamine (2.5 mM), streptomycin (100 µg/mL) and foetal bovine serum (10% v/v). Cells were passaged at approximately 90% confluence, using PBS to wash and TrypLE solution to detach the cells. Cell pellets were obtained through centrifugation at 2000 RPM for 5 minutes. The cells were cultured in 25 cm^2 collagen coated cell culture flasks and incubated at 37 ^oC in a 5% CO_2 humidified atmosphere.

In order to perform cell uptake studies, T98G and SVG-p12 cells were seeded onto 12-well plates, and grown to approximately 80% confluence. The cells were counted using a ThermoFisher® Countess automated cell counter. The culture medium in each plate was then removed and replaced with culture medium dosed with either **13**, **14**, **16** or **17** at a concentration of 100 µM, as well as a non-dosed control. Each concentration, as well as the non-dosed control, was repeated in triplicate for both cell lines. The cells were incubated for a further 24 hours with the dosing medium. They were then harvested by first washing with PBS, followed by trypsinisation with TrypLE. The cells were pelleted by centrifugation and then washed twice with PBS, re-centrifuging after each wash. The PBS supernatant was discarded and the cells digested in concentrated HNO_3 (100 µL, 69%) for 24 hours at room temperature. This digest solution was then made up to 5 mL with water, and the lanthanoid metal content was measured using ICP-MS.

In order to perform cell microscopy studies, T98G and SVG-p12 cells were seeded onto 35 mm glass bottom microscopy dishes, and grown to approximately 80%

confluence. The culture medium in each dish was then removed and replaced with culture medium dosed with either **13**, **14**, **16** or **17** at a concentration of 100 µM, as well as a non-dosed control. The cells were incubated for a further 24 hours with the dosing medium, followed by a 15 minute incubation with MTDR probe at a concentration of 100 nM. The medium was replaced with PBS and the cells were visualised under a Leica SP5 II Confocal and Multiphoton microscope. A 25W objective was used with an open pinhole and images were captured at both 1X and 4X zoom. Brightfield images were first captured, using 200 V of gain and a laser power of 2%, with the PMT NDD3 detector. Fluorescence images of the lanthanoid complexes were then obtained, using excitation wavelengths of 488 nm for complexes **13** and **14**, and 458 nm for complexes **16** and **17**, both with approximately 20% laser power and approximately 800 V gain. Fluorescence images of the complexes were captured between 450-630 nm, with the PMT1 detector. Fluorescence images of the MTDR probe were then obtained, using an excitation wavelength of 644 nm with 2% laser power and approximately 800 V gain. Fluorescence images of MTDR were collected between 660-670 nm using the PMT3 detector. The three images captured for each level of magnification were overlayed and the emission overlap was quantified using ImageJ® software.

Chapter 6:

References

1. Knowles MA, Selby PJ. *Introduction to the Cellular and Molecular Biology of Cancer*. Vol 4.(11):1-33; 2005. http://jcp.bmj.com/cgi/doi/10.1136/jcp.45.1.91-d
2. Murray CJL, Salomon JA, Mathers CD, Lopez AD. Summary measures of population health: concepts, ethics, measurement and applications. Published online 2002:814(1-13). http://books.google.co.uk/books?id=1kEv5qL22pQC
3. Australian Government. *Australian Burden of Disease Study: Impact and Causes of Illness and Death in Australia*.; 2016(16-28). https://www.aihw.gov.au/reports/burden-of-disease/burden-disease-study-illness-death-2015/contents/table-of-contents
4. Bates N, Callander E, Lindsay D, Watt K. Labour force participation and the cost of lost productivity due to cancer in Australia. *BMC Public Health*. 2018;18(1):1-7. doi:10.1186/s12889-018-5297-9
5. Urbanska K, Sokolowska J, Szmidt M, Sysa P. Glioblastoma multiforme - An overview. *Contemp Oncol*. 2014;18(5):307-312. doi:10.5114/wo.2014.40559
6. Simpson JR, Horton J, Scott C, et al. Influence of location and extent of surgical resection on survival of patients with glioblastoma multiforme: Results of three consecutive radiation therapy oncology group (RTOG) clinical trials. *Int J Radiat Oncol Biol Phys*. 1993;26(2):239-244. doi:10.1016/0360-3016(93)90203-8
7. Mahvash M, Hugo HH, Maslehaty H, Mehdorn HM, Stark AM. Glioblastoma multiforme in children: Report of 13 cases and review of the literature. *Pediatr Neurol*. 2011;45(3):178-180. doi:10.1016/j.pediatrneurol.2011.05.004
8. Karcher S, Steiner HH, Ahmadi R, et al. Different angiogenic phenotypes in primary and secondary glioblastomas. *Int J Cancer*. 2006;118(9):2182-2189. doi:10.1002/ijc.21648
9. Allen C, Her S, Jaffray DA. Radiotherapy for Cancer: Present and Future. *Adv Drug Deliv Rev*. 2017;109:1-2. doi:10.1016/j.addr.2017.01.004
10. Kim W, Lee S, Seo D, et al. Cellular Stress Responses in Radiotherapy. *Cells*. 2019;8(9):1-18. doi:10.3390/cells8091105
11. De Ruysscher D, Niedermann G, Burnet NG, Siva S, Lee AWM, Hegi-Johnson F. Radiotherapy toxicity. *Nat Rev Dis Prim*. 2019;5(1). doi:10.1038/s41572-019-0064-5
12. Chang JE, Khuntia D, Robins HI, Mehta MP. Radiotherapy and

radiosensitizers in the treatment of glioblastoma multiforme. *Clin Adv Hematol Oncol*. 2007;5(11):894-915.

13. Chabner BA, Roberts TG. Chemotherapy and the war on cancer. *Nat Rev Cancer*. 2005;5(1):65-72. doi:10.1038/nrc1529
14. Kislin KL, McDonough WS, Eschbacher JM, Armstrong BA, Berens ME. NHERF-1: Modulator of glioblastoma cell migration and invasion. *Neoplasia*. 2009;11(4):377-387. doi:10.1593/neo.81572
15. Rocha Pinheiro SL, Lemos FFB, Marques HS, et al. Immunotherapy in glioblastoma treatment: Current state and future prospects. *World J Clin Oncol*. 2023;14(4):138-159. doi:10.5306/wjco.v14.i4.138
16. Jaracz S, Chen J, Kuznetsova L V., Ojima I. Recent advances in tumor-targeting anticancer drug conjugates. *Bioorganic Med Chem*. 2005;13(17):5043-5054. doi:10.1016/j.bmc.2005.04.084
17. Cui Q, Wen S, Huang P. Targeting cancer cell mitochondria as a therapeutic approach: recent update. *Chimia (Aarau)*. 2017;71(10):643. doi:10.2307/j.ctvnwc0d0.18
18. Warburg O. On the origin of cancer cells. *Science (80-)*. 1956;123(3191):309-314. doi:10.1126/science.123.3191.309
19. Bonora M, Patergnani S, Rimessi A, et al. ATP synthesis and storage. *Purinergic Signal*. 2012;8(3):343-357. doi:10.1007/s11302-012-9305-8
20. Maldonado EN, Lemasters JJ. Warburg revisited: Regulation of mitochondrial metabolism by voltage-dependent anion channels in cancer cells. *J Pharmacol Exp Ther*. 2012;342(3):637-641. doi:10.1124/jpet.112.192153
21. Harvey AJ, Kind KL, Thompson JG. REDOX regulation of early embryo development. *Reproduction*. 2002;123(4):479-486. doi:10.1530/rep.0.1230479
22. Bustamante E, Pedersen PL. High aerobic glycolysis of rat hepatoma cells in culture: Role of mitochondrial hexokinase. *Proc Natl Acad Sci U S A*. 1977;74(9):3735-3739. doi:10.1073/pnas.74.9.3735
23. Heiden MGV, Cantley LC, Thompson CB. Understanding the warburg effect: The metabolic requirements of cell proliferation. *Science (80-)*. 2009;324(5930):1029-1033. doi:10.1126/science.1160809
24. Bustamante E, Morris HP, Pedersen PL. Energy metabolism of tumor cells. Requirement for a form of hexokinase with a propensity for mitochondrial binding. *J Biol Chem*. 1981;256(16):8699-8704. doi:10.1016/s0021-

9258(19)68900-3

25. Christofk HR, Vander Heiden MG, Harris MH, et al. The M2 splice isoform of pyruvate kinase is important for cancer metabolism and tumour growth. *Nature*. 2008;452(7184):230-233. doi:10.1038/nature06734
26. Pedersen PL. Warburg, me and Hexokinase 2: Multiple discoveries of key molecular events underlying one of cancers' most common phenotypes, the "Warburg Effect", i.e., elevated glycolysis in the presence of oxygen. *J Bioenerg Biomembr*. 2007;39(3):211-222. doi:10.1007/s10863-007-9094-x
27. Geschwind JF, Georgiades CS, Ko YH, Pedersen PL. Recently elucidated energy catabolism pathways provide opportunities for novel treatments in hepatocellular carcinoma. *Expert Rev Anticancer Ther*. 2004;4(3):449-457. doi:10.1586/14737140.4.3.449
28. Ward PS, Thompson CB. Metabolic Reprogramming: A Cancer Hallmark Even Warburg Did Not Anticipate. *Cancer Cell*. 2012;21(3):297-308. doi:10.1016/j.ccr.2012.02.014
29. Chandra D, Singh KK. Genetic insights into OXPHOS defect and its role in cancer. *Biochim Biophys Acta - Bioenerg*. 2011;1807(6):620-625. doi:10.1016/j.bbabio.2010.10.023
30. Modica-Napolitano JS, Aprille JR. Basis for the Selective Cytotoxicity of Rhodamine 123. *Cancer Res*. 1987;47(16):4361-4365.
31. Dairkee SH, Hackett AJ. Differential retention of rhodamine 123 by breast carcinoma and normal human mammary tissue. *Breast Cancer Res Treat*. 1991;18(1):57-61. doi:10.1007/BF01975444
32. Davis S, Weiss MJ, Wong JR, Lampidis TJ, Chen LB. Mitochondrial and plasma membrane potentials cause unusual accumulation and retention of rhodamine 123 by human breast adenocarcinoma-derived MCF-7 cells. *J Biol Chem*. 1985;260(25):13844-13850. doi:10.1016/s0021-9258(17)38802-6
33. Summerhayes IC, Lampidis TJ, Bernal SD, et al. Unusual retention of rhodamine 123 by mitochondria in muscle and carcinoma cells. *Proc Natl Acad Sci U S A*. 1982;79(17 I):5292-5296. doi:10.1073/pnas.79.17.5292
34. Johnson L V., Walsh ML, Chen LB. Localisation of mitochondria in living cells with rhodamine 123. *Proc Natl Acad Sci U S A*. 1980;77(2 II):990-994. doi:10.1073/pnas.77.2.990
35. Zhang B bei, Wang D gang, Guo F fen, Xuan C. Mitochondrial membrane

potential and reactive oxygen species in cancer stem cells. *Fam Cancer*. 2015;14(1):19-23. doi:10.1007/s10689-014-9757-9

36. Lonergan T, Brenner C, Bavister B. Differentiation-Related Changes in Mitochondrial Properties as Indicators of Stem Cell Competence. *J Cell Physiol*. 2006;208(May):149-153. doi:10.1002/JCP
37. Johnson L V., Walsh ML, Bockus BJ, Chen LB. Monitoring of relative mitochondrial membrane potential in living cells by fluorescence microscopy. *J Cell Biol*. 1981;88(3):526-535. doi:10.1083/jcb.88.3.526
38. Bernal, S. D.; Lampidis, T. J.; Summerhayes IC. Rhodamine-123 Selectively Reduces Clonal Growth of Carcinoma Cells in vitro Published by : American Association for the Advancement of Science Stable URL : https://www.jstor.org/stable/1688958. *Science (80-)*. 1982;218(4577):1117-1119.
39. Bernal SD, Lampidis TJ, Mcisaac RM, Chen LB. Anticarcinoma activity in vivo of rhodamine 123, a mitochondrial-specific dye. *Science (80-)*. 1983;222(4620):169-172. doi:10.1126/science.6623064
40. Lampidis T, Bernal S, Summerhayes I, Chen L. Selective Toxicity of Rhodamine 123 in Carcinoma Cells. *Cancer Res*. 1983;43(February):716-720.
41. Modica-Napolitano JS, Singh KK. Mitochondria as targets for detection and treatment of cancer. *Expert Rev Mol Med*. 2002;4(9):1-19. doi:10.1017/s1462399402004453
42. Modica-Napolitano JS, Weiss MJ, Chen LB, Aprille JR. Rhodamine 123 inhibits bioenergetic function in isolated rat liver mitochondria. *Biochem Biophys Res Commun*. 1984;118(3):717-723. doi:10.1016/0006-291X(84)91453-0
43. Emaus RK, Grunwald R, Lemasters JJ. Rhodamine 123 as a probe of transmembrane potential in isolated rat-liver mitochondria: spectral and metabolic properties Ronald K. Emaus, Ron Grunwald and John J. Lemasters *. *Biochim Biophys Acta*. 1986;850:436-448.
44. Sun X, Song K, Hu J, Garlid KD. AAl, A Newly Synthesized Monovalent Lipophilic Cation, Expresses Potent in Vivo Antitumor Activity. *Cancer Res*. 1994;54(6):1465-1471.
45. Rideout D, Bustamante A, Patel J. Mechanism of inhibition of fadu hypopharyngeal carcinoma cell growth by tetraphenylphosphonium chloride.

Int J Cancer. 1994;57(2):247-253. doi:10.1002/ijc.2910570220

46. Anderson WM, Delinck DL, Benninger L, Wood JM, Smiley ST, Chen LB. Cytotoxic effect of thiacarbocyanine dyes on human colon carcinoma cells and inhibition of bovine heart mitochondrial NADH-ubiquinone reductase activity via a rotenone-type mechanism by two of the dyes. *Biochem Pharmacol*. 1993;45(3):691-696. doi:10.1016/0006-2952(93)90144-L
47. Pilch YH. Mediation of Immunity to Tumor-specific Transplantation Antigens by RNA Inhibition of Isograft Growth in Rats. *Cancer Res*. 1972;32(4):839-846.
48. Weiss MJ, Wong JR, Ha CS, et al. Dequalinium, a topical antimicrobial agent, displays anticarcinoma activity based on selective mitochondrial accumulation. *Proc Natl Acad Sci U S A*. 1987;84(15):5444-5448. doi:10.1073/pnas.84.15.5444
49. Koya K, Li Y, Wang H, et al. MKT-077, a novel rhodacyanine dye in clinical trials, exhibits anticarcinoma activity in preclinical studies based on selective mitochondrial accumulation. *Cancer Res*. 1996;56(3):538-543.
50. Wright SH. Generation of resting membrane potential. *Am J Physiol - Adv Physiol Educ*. 2004;28(4):139-142. doi:10.1152/advan.00029.2004
51. Ross MF, Kelso GF, Blaikie FH, et al. Lipophilic triphenylphosphonium cations as tools in mitochondrial bioenergetics and free radical biology. *Biokhimiya*. 2005;70(2):273-283.
52. Modica-Napolitano JS, Aprille JR. Delocalised lipophilic cations selectively target the mitochondria of carcinoma cells. *Adv Drug Deliv Rev*. 2001;49(1-2):63-70. doi:10.1016/S0169-409X(01)00125-9
53. Lampidis TJ, Salet C, Moreno G, Chen LB. Effects of the mitochondrial probe rhodamine 123 and related analogs on the function and viability of pulsating myocardial cells in culture. *Agents Actions*. 1984;14(5-6):751-757. doi:10.1007/BF01978920
54. Ketterer B, Neumcke B, Läuger P. Transport mechanism of hydrophobic ions through lipid bilayer membranes. *J Membr Biol*. 1971;5(3):225-245. doi:10.1007/BF01870551
55. Flewelling RF, Hubbell WL. Hydrophobic ion interactions with membranes. Thermodynamic analysis of tetraphenylphosphonium binding to vesicles. *Biophys J*. 1986;49(2):531-540. doi:10.1016/S0006-3495(86)83663-3
56. Honig BH. Electrostatic Interactions in Membranes and Proteins. *Electrost*

Interact. 1986;(15):163-193.

57. Flewelling RF, Hubbell WL. The membrane dipole potential in a total membrane potential model. Applications to hydrophobic ion interactions with membranes. *Biophys J*. 1986;49(2):541-552. doi:10.1016/S0006-3495(86)83664-5
58. James AM, Blaikie FH, Smith RAJ, Lightowlers RN, Smith PM, Murphy MP. Specific targeting of a DNA-alkylating reagent to mitochondria: Synthesis and characterisation of [4-((11aS)-7-methoxy-1,2,3,11a-tetrahydro-5H-pyrrolo[2,1-c][1,4] benzodiazepin-5-on-8-oxy)butyl]-triphenylphosphonium iodide. *Eur J Biochem*. 2003;270(13):2827-2836. doi:10.1046/j.1432-1033.2003.03660.x
59. Murphy MP, Echtay KS, Blaikie FH, et al. Superoxide activates uncoupling proteins by generating carbon-centered radicals and initiating lipid peroxidation: Studies using a mitochondria- targeted spin trap derived from α-phenyl-N-tert-butylnitrone. *J Biol Chem*. 2003;278(49):48534-48545. doi:10.1074/jbc.M308529200
60. Chen LB. Mitochondrial membrane potential in living cells. *Neuroscience*. 1988;10(4):155-181. http://dx.doi.org/10.1038/nrn2665
61. Rideout DC, Calogeropoulou T, Jaworski JS, Dagnino R, McCarthy M. Phosphonium salts exhibiting selective anti- carcinoma activity in vitro. *Anticancer Drug Des*. 1989;4(4):265-280.
62. Madar I, Weiss L, Izbicki G. Preferential accumulation of 3H-tetraphenylphosphonium in non-small cell lung carcinoma in mice: Comparison with 99mTc-MIBI. *J Nucl Med*. 2002;43(2):234-238.
63. Zhou Y, Liu S. 64Cu-labeled phosphonium cations as PET radiotracers for tumor imaging. *Bioconjug Chem*. 2011;22(8):1459-1472. doi:10.1021/bc200106p
64. Liu S, Kim YS, Zhai S, Shi J, Hou G. Evaluation of 64Cu(DO3A-xy-TPEP) as a potential PET radiotracer for monitoring tumor multidrug resistance. *Bioconjug Chem*. 2009;20(4):790-798. doi:10.1021/bc800545e
65. Robinson KM, Janes MS, Beckman JS. The selective detection of mitochondrial superoxide by live cell imaging. *Nat Protoc*. 2008;3(6):941-947. doi:10.1038/nprot.2008.56
66. Smith RAJ, Porteous CM, Coulter C V., Murphy MP. Selective targeting of an antioxidant to mitochondria. *Eur J Biochem*. 1999;263(3):709-716.

doi:10.1046/j.1432-1327.1999.00543.x

67. Manetta A, Gamboa G, Nasseri A, et al. Novel phosphonium salts display in vitro and in vivo cytotoxic activity against human ovarian cancer cell lines. *Gynecol Oncol*. 1996;60(2):203-212. doi:10.1006/gyno.1996.0026
68. Abu-Gosh SE, Kolvazon N, Tirosh B, Ringel I, Yavin E. Multiple triphenylphosphonium cations shuttle a hydrophilic peptide into mitochondria. *Mol Pharm*. 2009;6(4):1138-1144. doi:10.1021/mp900032r
69. Hawthorne MF. The Role of Chemistry in the Development of Boron Neutron Capture Therapy of Cancer. *Angew Chemie Int Ed English*. 1993;32(7):950-984. doi:10.1002/anie.199309501
70. Morrison DE, Aitken JB, De Jonge MD, Issa F, Harris HH, Rendina LM. Synthesis and biological evaluation of a class of mitochondrially-targeted gadolinium(III) agents. *Chem - A Eur J*. 2014;20(50):16602-16612. doi:10.1002/chem.201404107
71. Meneely GR. *Neutron Capture Therapy*. Vol 194.; 1965. doi:10.1001/jama.1965.03090230119044
72. Dymova MA, Taskaev SY, Richter VA, Kuligina EV. Boron neutron capture therapy: Current status and future perspectives. *Cancer Commun*. 2020;40(9):406-421. doi:10.1002/cac2.12089
73. Barth RF, Coderre JA, Vicente MGH, Blue TE. Boron neutron capture therapy of cancer: Current status and future prospects. *Clin Cancer Res*. 2005;11(11):3987-4002. doi:10.1158/1078-0432.CCR-05-0035
74. Yang Z, Lin H, Huang J, et al. A gadolinium-complex-based theranostic prodrug for: In vivo tumour-targeted magnetic resonance imaging and therapy. *Chem Commun*. 2019;55(31):4546-4549. doi:10.1039/c9cc01816f
75. MARTIN RF, D'CUNHA G, PARDEE M, ALLEN BJ. Induction of DNA Double-Strand Breaks by 157Gd Neutron Capture. *Pigment Cell Res*. 1989;2(4):330-332. doi:10.1111/j.1600-0749.1989.tb00213.x
76. Gierga DP, Yanch JC, Shefer RE. An investigation of the feasibility of gadolinium for neutron capture synovectomy. *Med Phys*. 2000;27(7):1685-1692. doi:10.1118/1.599037
77. Hall AJ, Robertson AG, Hill LR, Rendina LM. Synthesis and tumour cell uptake studies of gadolinium(III)–phosphonium complexes. *Sci Rep*. 2021;11(1):1-14. doi:10.1038/s41598-020-79893-9

78. Adam JF, Elleaume H, Joubert A, et al. Synchrotron radiation therapy of malignant brain glioma loaded with an iodinated contrast agent: First trial on rats bearing F98 gliomas. *Int J Radiat Oncol Biol Phys*. 2003;57(5):1413-1426. doi:10.1016/j.ijrobp.2003.07.007
79. Radiation dose enhancement in tumors with iodine. *Med Phys*. 1983;10(1):75-78.
80. Hofer KG. Biophysical aspects of Auger processes. *Acta Oncol (Madr)*. 2000;39(6):651-657. doi:10.1080/028418600750063686
81. Robertson AG, Rendina LM. Gadolinium theranostics for the diagnosis and treatment of cancer. *Chem Soc Rev*. Published online 2021. doi:10.1039/x0xx00000x
82. Laster BH, Dixon DW, Novick S, et al. Photon activation therapy and brachytherapy. *Brachytherapy*. 2009;8(3):324-330. doi:10.1016/j.brachy.2008.12.008
83. Laster ABH, Thomlinson WC, Fairchild RG. Photon Activation of Iododeoxyuridine : Biological Efficacy of Auger Electrons. *Radiat Res*. 1993;133(2):219-224.
84. Goorley T, Nikjoo H, Goorley T, Nikjoob H. Electron and Photon Spectra for Three Gadolinium-Based Cancer Therapy Approaches. *Radiat Res*. 2000;154(5):556-563.
85. Fok JS, Smith WB. Hypersensitivity reactions to gadolinium-based contrast agents. *Curr Opin Allergy Clin Immunol*. 2017;17(4):241-246. doi:10.1097/ACI.0000000000000371
86. Runge VM, Clanton JA, Lukehart CM, Partain CL J a. . Paramagnetic Agents for NMR Imaging : A Review. *Ajr*. 1983;141(6):1209-1215.
87. Heckman JJ, Pinto R, Savelyev PA. Proton Relaxation Enhancement. *Angew Chemie Int Ed 6(11), 951–952*. 1967;(8):149-156.
88. Aime S, Caravan P. Biodistribution of gadolinium-based contrast agents, including gadolinium deposition. *J Magn Reson Imaging*. 2009;30(6):1259-1267. doi:10.1002/jmri.21969
89. Ramalho J, Ramalho M, Jay M, Burke LM, Semelka RC. Gadolinium toxicity and treatment. *Magn Reson Imaging*. 2016;34(10):1394-1398. doi:10.1016/j.mri.2016.09.005
90. Kanal E, Maravilla K, Rowley HA. Gadolinium Contrast Agents for CNS

Imaging : Current Concepts and Clinical Evidence. *AJNR*. 2014;35:2215-2226.

91. Laurent S, Elst L Vander, Muller RN. Comparative study of the physicochemical properties of six clinical low molecular weight gadolinium contrast agents. 2006;137:128-137. doi:10.1002/cmmi.100
92. Layne KA, Wood DM, Dargan PI, Layne KA, Wood DM, Gadolinium-based PID. Gadolinium-based contrast agents – what is the evidence for ‘ gadolinium deposition disease ’ and the use of chelation therapy ? *Clin Toxicol*. 2020;58(3):151-160. doi:10.1080/15563650.2019.1681442
93. Wolfbeis OS, Hanninen P, Harama H. *Lanthanide Luminescence*. Vol 7.; 2011.
94. Baranyai Z, Tircsó G, Rösch F. The Use of the Macrocyclic Chelator DOTA in Radiochemical Separations. *Eur J Inorg Chem*. 2020;2020(1):36-56. doi:10.1002/ejic.201900706
95. Kostelnik TI, Orvig C. Radioactive Main Group and Rare Earth Metals for Imaging and Therapy. *Chem Rev*. 2019;119(2):902-956. doi:10.1021/acs.chemrev.8b00294
96. Giese E. Rare Earth Elements: therapeutic and diagnostic applications in modern medicine. *Clin Med Reports*. 2018;2(1):1-2. doi:10.15761/cmr.1000139
97. Karlin KP, Zubieta J, Linder MC, et al. Production and Applications of Copper-64 Radiopharmaceuticals. *Methods Enzymol*. 2004;386(1973):237-261.
98. Petersdorf S, Baker M, Eat JF, et al. Samarium-153-EDTMP Biodistribution and Estimation. *J Nucl Med*. 1993;34:1031-1036.
99. Dadabhoy A, Faulkner S, Sammes PG. Long wavelength sensitizers for europium(iii) luminescence based on acridone derivatives. *J Chem Soc Perkin Trans 2*. 2002;2(2):348-357. doi:10.1039/b104541p
100. Dillip GR, Madhukar Reddy C, Rajesh M, Chaurasia S, Deva Prasad Raju B, Joo SW. Green fluorescence of terbium ions in lithium fluoroborate glasses for fibre lasers and display devices. *Bull Mater Sci*. 2016;39(3):711-717. doi:10.1007/s12034-016-1192-0
101. Montgomery CP, Murray BS, New EJ, Pal R, Parker D. Cell-penetrating metal complex optical probes: Targeted and responsive systems based on lanthanide luminescence. *Acc Chem Res*. 2009;42(7):925-937. doi:10.1021/ar800174z
102. Bünzli JCG, Piguet C. Taking advantage of luminescent lanthanide ions. *Chem*

Soc Rev. 2005;34(12):1048-1077. doi:10.1039/b406082m

103. Brunet E, Juanes O, Rodriguez-Ubis J. Supramolecularly Organized Lanthanide Complexes for Efficient Metal Excitation and Luminescence as Sensors in Organic and Biological Applications. *Curr Chem Biol*. 2012;1(1):11-39. doi:10.2174/2212796810701010011
104. Hasegawa Y, Kitagawa Y, Nakanishi T. Effective photosensitized, electrosensitized, and mechanosensitized luminescence of lanthanide complexes /639/638/439/943 /639/638/911 review-article. *NPG Asia Mater*. 2018;10(4):52-70. doi:10.1038/s41427-018-0012-y
105. de Sa GF, Malta OL, Donega C, et al. *Spectroscopic Properties and Design of Highly Luminescent Lanthanide Coordination Complexes*. Vol 196.; 2000. doi:10.1007/978-1-4939-0808-0_2
106. Dexter DL. A theory of sensitized luminescence in solids. *J Chem Phys*. 1953;21(5):836-850. doi:10.1063/1.1699044
107. Förster T. Transfer mechanisms of electronic excitation. *Discuss Faraday Soc*. 1959;27(10):7-17. doi:10.1039/DF9592700007
108. Mara D, Artizzu F, Smet PF, Kaczmarek AM, Van Hecke K, Van Deun R. Vibrational Quenching in Near-Infrared Emitting Lanthanide Complexes: A Quantitative Experimental Study and Novel Insights. *Chem - A Eur J*. 2019;25(69):15944-15956. doi:10.1002/chem.201904320
109. Garda Z, Kócs T, Bányai I, et al. Complexes of bifunctional do3a-n-(α-amino)propinate ligands with mg(ii), ca(ii), cu(ii), zn(ii), and lanthanide(iii) ions: Thermodynamic stability, formation and dissociation kinetics, and solution dynamic nmr studies. *Molecules*. 2021;26(16). doi:10.3390/molecules26164956
110. Busse M, Windsor MSA, Tefay AJ, et al. Tumor cell uptake and selectivity of gadolinium(III)-phosphonium complexes: The role of delocalisation at the phosphonium centre. *J Inorg Biochem*. 2017;177(April):313-321. doi:10.1016/j.jinorgbio.2017.07.004
111. Faulkner S, Pope SJA, Burton-Pye BP. Lanthanide complexes for luminescence imaging applications. *Appl Spectrosc Rev*. 2005;40(1):1-31. doi:10.1081/ASR-200038308
112. Hanaoka K, Kikuchi K, Kobayashi S, Nagano T. Time-resolved long-lived luminescence imaging method employing luminescent lanthanide probes with

a new microscopy system. *J Am Chem Soc*. 2007;129(44):13502-13509. doi:10.1021/ja073392j

113. Morrison DE, Aitken JB, De Jonge MD, Ioppolo JA, Harris HH, Rendina LM. High mitochondrial accumulation of new gadolinium(III) agents within tumour cells. *Chem Commun*. 2014;50(18):2252-2254. doi:10.1039/c3cc46903d
114. Otog N, Gantogos B, Fujisawa I, Iwasa S. Highly enantioselective synthesis of norcaradiene derivatives from naphthyl diazoacetamides using a Ru(ii)-Pheox complex. *Chem Commun*. 2022;58(88):12325-12328. doi:10.1039/d2cc04355f
115. Djerassi C. BROMINATIONS WITH N-BROMOSUCCINIMIDE AND RELATED COMPOUNDS. Published online 1948.
116. Beeby A, Clarkson IM, Dickins RS, et al. Non-radiative deactivation of the excited states of europium, terbium and ytterbium complexes by proximate energy-matched OH, NH and CH oscillators: An improved luminescence method for establishing solution hydration states. *J Chem Soc Perkin Trans 2*. 1999;2(3):493-503. doi:10.1039/a808692c
117. Farsinejad S, Gheisary Z, Ebrahimi Samani S, Alizadeh AM. Mitochondrial targeted peptides for cancer therapy. *Tumor Biol*. 2015;36(8):5715-5725. doi:10.1007/s13277-015-3719-1
118. Fernández M, Javaid F, Chudasama V. Advances in targeting the folate receptor in the treatment/imaging of cancers. *Chem Sci*. 2018;9(4):790-810. doi:10.1039/c7sc04004k
119. Chithrani BD, Chan WCW. Elucidating the mechanism of cellular uptake and removal of protein-coated gold nanoparticles of different sizes and shapes. *Nano Lett*. 2007;7(6):1542-1550. doi:10.1021/nl070363y
120. Egger AE, Rappel C, Jakupec MA, Hartinger CG, Heffeter P, Keppler BK. Development of an experimental protocol for uptake studies of metal compounds in adherent tumor cells. *J Anal At Spectrom*. 2009;24(1):51-61. doi:10.1039/b810481f
121. D'Souza RCJ, Offenhäuser C, Straube J, et al. Q-Cell Glioblastoma Resource: Proteomics Analysis Reveals Unique Cell-States are Maintained in 3D Culture. *Cells*. 2020;9(2). doi:10.3390/cells9020267